**IEA Wind Task 46**

**Erosion of wind turbine blades**

# A V&V framework for numerical simulations of LEE drivers: Preliminary results

## Technical Report

**iea wind**

# Technical Report

# A V&V framework for numerical simulations of LEE drivers: Preliminary results

**Prepared for the**

**International Energy Agency Wind Implementing Agreement**

**Authors:**

**Sara C. Pryor, Cornell University (sp2279@cornell.edu)**

**Rebecca J. Barthelmie, Cornell University**

**Xin Zhou, Cornell University**

**14 March 2025**

IEA Wind TCP functions within a framework created by the International Energy Agency (IEA). Views, findings, and publications of IEA Wind do not necessarily represent the views or policies of the IEA Secretariat or of all its individual member countries. IEA Wind is part of IEA's Technology Collaboration Programme (TCP).

# Purpose

Leading edge erosion (LEE) of wind turbine blades has been identified as a major factor in decreased wind turbine blade lifetimes and energy output over time. Accordingly, the International Energy Agency Wind Technology Collaboration Programme (IEA Wind TCP) has created the Task 46 to undertake cooperative research in the key topic of blade erosion. Participants in the task are given in Table 1.

The Task 46 under IEA Wind TCP is designed to improve understanding of the drivers of LEE, the geospatial and temporal variability in erosive events; the impact of LEE on the performance of wind plants and the cost/benefit of proposed mitigation strategies. Furthermore Task 46 seeks to increase the knowledge about erosion mechanics and the material properties at different scales, which drive the observable erosion resistance. Finally, the Task aims to identify the laboratory test setups which reproduce faithfully the failure modes observed in the field in the different protective solutions.

This report is a product of Work Package 2 **Climatic conditions driving blade erosion.**

The objectives of this report are to:

- Summarized recent research using Numerical Weather Prediction (NWP) models to make predictions of the meteorological drivers of wind turbine blade LEE in the context of:

    a. Assessing the erosion climate over a region i.e. enabling development of erosion atlases

    b. Making day-ahead forecasts of highly erosive periods to inform possible use of erosion safe mode operation

- Describe data and metrics that have been used to quantify simulation fidelity in the context of wind turbine blade LEE applications

- Make recommendations regarding the process of building a robust model verification and validation (V&V) framework for assessing simulation fidelity in the context of wind turbine blade LEE

**Table 1 IEA Wind Task 46 Participants.**

| Country | Contracting Party | Active Organizations |
|---|---|---|
| Belgium | The Federal Public Service of Economy, SMEs, Self-Employed and Energy | Engie |
| Canada | Natural Resources Canada | WEICan |
| Denmark | Danish Energy Agency | DTU (OA), Hempel, Ørsted A/S, PowerCurve, Siemens Gamesa Renewable Energy |
| Finland | Business Finland | VTT |
| Germany | Federal Ministry for Economic Affairs and Energy | Fraunhofer IWES, Covestro, Emil Frei (Freilacke), Nordex Energy SE, RWE, DNV, Mankiewicz, Henkel |
| Ireland | Sustainable Energy Authority of Ireland | South East Technology University, University of Galway, University of Limerick |
| Japan | New Energy and Industrial Technology Development Organization | AIST, Asahi Rubber Inc., Osaka University, Tokyo Gas Co. |
| Netherlands | Netherlands Enterprise Agency | TU Delft, TNO |
| Norway | Norwegian Water Resources and Energy Directorate | Equinor, University of Bergen, Statkraft |
| Spain | CIEMAT | CENER, Aerox, CEU Cardenal Herrera University, Nordex Energy Spain |
| United Kingdom | Offshore Renewable Energy Catapult | ORE Catapult, University of Bristol, Lancaster University, Imperial College London, Ilosta, Vestas |
| United States | U. S. Department of Energy | Cornell University, Sandia National Laboratories, 3M |

# Table of Contents

# List of Figures

# List of Tables

# Executive Summary

Wind turbine blade leading edge erosion (LEE) reduces electricity production and increases wind energy operation and maintenance costs. Numerical Weather Prediction (NWP) models such as the Weather Research and Forecasting (WRF) model have long been employed for wind resource assessments and short-term power production forecasts. These models also have potential utility in assessment of both the long-term erosion climate and short-term forecasting for erosion safe mode operation. However, these applications require simulation fidelity that has not yet been demonstrated. This report summarizes recent work to develop a preliminary V&V framework for quantifying model fidelity of LEE relevant properties and that has demonstrated critical model configuration components that dictate model skill.

# 1. Introduction

Erosion of wind turbine blade coatings with subsequent exposure and erosion of the substrate causes decreased aerodynamic performance and increases operation and maintenance costs. At most locations, the primary cause of wind turbine blade leading edge erosion (LEE) is materials stresses caused by falling hydrometeors impacting on rapidly rotating wind turbine blades (Bartolomé and Teuwen 2019; Bech; Hasager; Bak 2018; Letson; Barthelmie; Pryor 2020; Pryor; Coburn; Barthelmie 2025; Pryor et al. 2022; Zhang et al. 2015). The amount of kinetic energy transferred from an ensemble of falling hydrometeors is dictated by:

(a) The closing velocity between the hydrometeors and the blade. Variations in wind turbine blade rotational speed are a function of incident wind speed at the hub-height. The rotational speed of the wind turbine blades during typical operation exceeds the terminal fall velocity of hydrometeors and hence generally dominates the closing velocity between falling hydrometeors and wind turbine blades.

(b) The number, size and phase of hydrometeors that impact the blade leading edge. The number of larger droplets is greatly enhanced under conditions with heavier precipitation (i.e. higher rainfall rates that describe the accumulation of water at the surface in a time interval) and/or when hail is present (Pryor et al. 2022). With respect to phase, collisions with hail (ice) versus rain (liquid) droplets may be more damaging than impacts from liquid hydrometeors (Heymsfield et al. 2018; Keegan; Nash; Stack 2013; Kim and Kedward 2000; Macdonald and Stack 2021; Savana 2022; Zhu et al. 2022). Note, although there is evidence that larger droplets that are more numerous during intense precipitation cause higher materials stresses (Pryor et al. 2024), hydrometeor size distributions (HSD) at the ground are typically not available from models or measurements. Thus development of erosion atlases based on availability of size-resolved droplet concentrations require post-processing of simulated/observed precipitation intensity using empirical relationships to derive HSD (Pryor; Coburn; Barthelmie 2025).

Numerical Weather Prediction (NWP) models such as the Weather Research and Forecasting (WRF) model (Skamarock et al. 2019) can simulate the space and time variability and magnitude of precipitation intensity/phase and wind speeds with relatively high fidelity. They thus have the potential to be used in two contexts within LEE prediction:

(a) Erosion climate assessment (i.e. development of 'erosion atlases'). Geospatially explicit estimates of LEE potential can enable wind farm developers to assess the costs/benefits of applying blade leading edge protection (LEP) at a given location(s) (Ansari et al. 2024; Herring et al. 2019; Katsivalis et al. 2022; Major et al. 2021; Sareen; Sapre; Selig 2014) and could help in scheduling blade inspections and maintenance scheduling/contracts at specific locations (Nielsen; Tcherniak; Ulriksen 2020; Papaelias and Márquez 2020). If erosion atlases also include high time-resolution in terms of damage accumulation (Pryor; Coburn; Barthelmie 2025), they could also provide critical information regarding Levelized Cost of Energy (LCoE) benefits from dynamic operation to reduce erosion (i.e. implementation of safe mode operation wherein the rotor speed is reduced during periods associated with high damage (Bech; Hasager; Bak 2018; Letson and Pryor 2023)).

(b) Short-term (day-ahead) forecasting for erosion safe mode operation (Bech; Hasager; Bak 2018; Letson and Pryor 2023). Forecasts of the potential need for dynamical operation to reduce coating damage could aid in accurate bidding on the day-ahead electricity market in a manner analogous to short-term power production forecasts (Tuncar; Sağlam; Oral 2024).

However, these applications represent stringent requirements for simulation fidelity in terms of the time and space joint (or copula) probabilities of wind speed and precipitation intensity plus the occurrence and size of hail. Intense precipitation (high rainfall rates) and hail are challenging for numerical models to accurately simulate (Adams-Selin et al. 2019; Davenport 2021; Gagne et al. 2017; Kumjian and Lombardo 2020; Prein et al. 2021; Scaff et al. 2020; Shepherd et al. 2024; Snook et al. 2016) due in part to complex cloud microphysics processes (Morrison et al. 2020; Tao et al. 2016) and strong, non-linear atmosphere-surface coupling (Dai; Williams; Qiu 2021; Feng et al. 2018). Model fidelity with respect to wind speeds is also a strong function of grid spacing, land use, topography and planetary boundary layer scheme employed (Carvalho et al. 2012; Hahmann et al. 2020; Jiménez and Dudhia 2013; Pryor and Hahmann 2019). Hence, there is a need for research to:

- Assess the fidelity of NWP models with respect to parameters of critical importance to LEE as a function of the model configuration. Such fidelity assessment must be predicated on application of appropriate statistical metrics of skill.

- Establish a robust Verification and Validation (V&V) framework (Thacker et al. 2004) that encapsulates the aspects of NWP simulation(s) critical to both the long-term erosion climate and short-term prediction of erosive events. Note, herein "Verification" means determining if a model is implemented in a manner that represents the physical understanding of the process(es) and "Validation" is the process of determining the degree to which the model represents the real world (i.e. agreement with observations). The expected outcome of a model V&V process is a quantitative statement of the agreement between experimental data and model prediction, as well as the predictive accuracy of the model.

## 2. Recent NWP simulations and validation in the context of LEE

This report focusses on three recent studies employing WRF simulations within the U.S. southern Great Plains (SGP). This geographic focus is partly due to the concentration of wind turbine assets in this region and the frequency of high wind speeds, intense precipitation, and hail (Figure 1). Annual total precipitation within the SGP exhibits large scale gradients (Figure 1a). Precipitation intensity and occurrence also exhibit very high spatiotemporal variability (see examples in Figure 2). Even under strong large scale (synoptic) forcing (e.g. Figure 2b, 9 March 2024) although precipitation is wide-spread, regions with highest intensity are often associated with embedded cells with deep convection and hence are rather localized. For this and other reasons, use of high resolution NWP simulations (i.e. use of small grid spacing) is necessary to capture the hydroclimate (Prein et al. 2021).
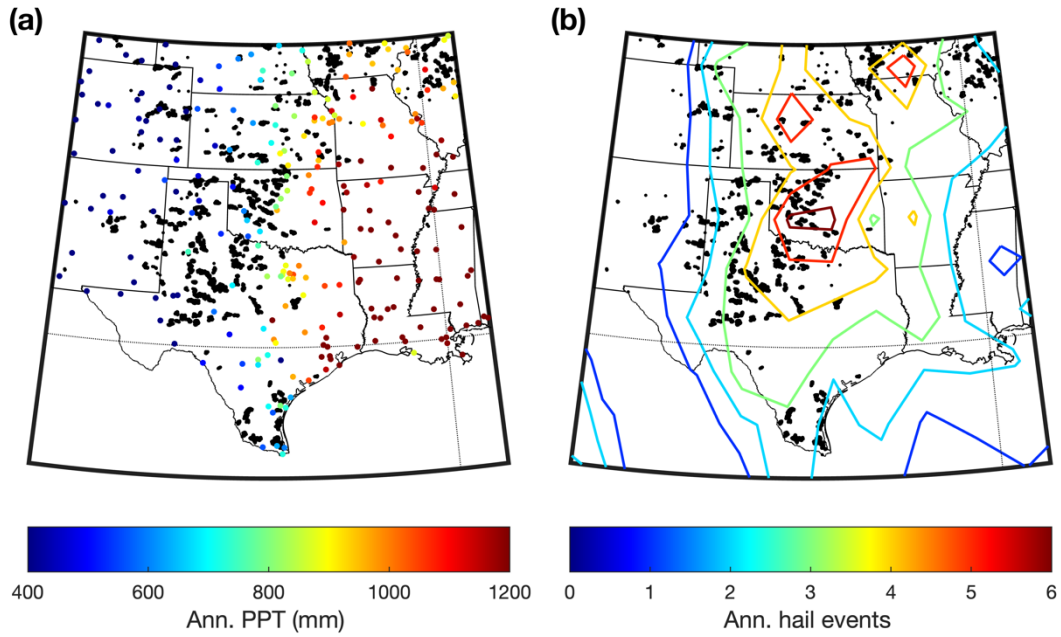
**Figure 1 Wind turbine locations and (a) annual total precipitation (mm) and (b) hail frequency in the U.S. Southern Great Plains.**

**(a) Colored dots show mean annual total precipitation at Automated Surface Observing Station (ASOS) sites computed using 1-min observations from 2005 to 2022 (Pryor; Coburn; Barthelmie 2025). (b) Colored contours show the mean number of hail days per year based on the NASA Passive Microwave Hail Climatology Data Products V1 dataset (Bang and Cecil 2019). Black dots indicate locations of wind turbines at the end of 2023.**
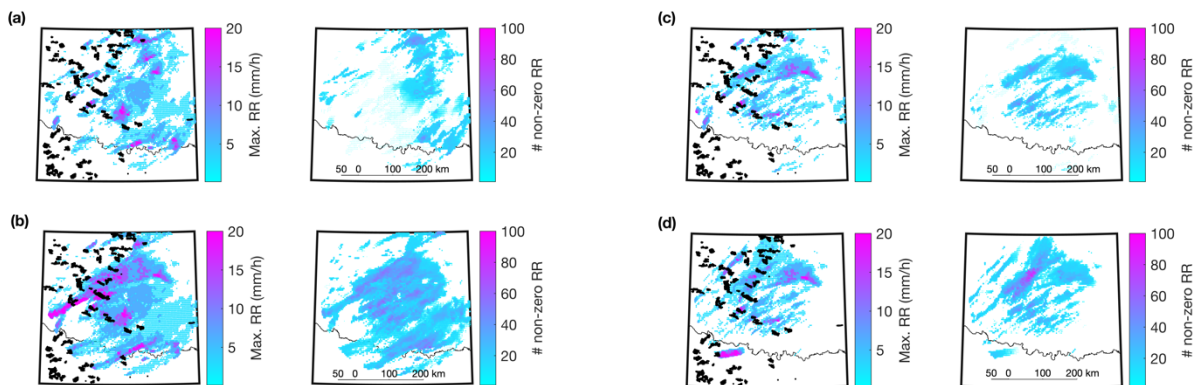


**Figure 2 Illustrative examples of spatiotemporal variability of precipitation in the U.S. Southern Great Plains.**

**5-minute observations with a dual polarization scanning Doppler RADAR located in Oklahoma City (Oklahoma/Texas state boundary shown by the thin black line) during (a) 7 March 2024, (b) 8 March 2024, (c) 9 March 2024 and (d) 24 March 2024. Left panels: Maximum precipitation intensity (mmhr$^{-1}$). Right panels: Number of all ~5-minute measurement periods within each day with non-zero precipitation. Data are measured at high spatial resolution but are presented here on ~ 4×4 km grid to aid legibility. Black dots indicate the locations of wind turbines.**

Two of the studies (study 1 and 2) summarized herein were undertaken in the context of building an erosion atlas (i.e. quantifying the long-term spatial variability in wind turbine blade coating lifetimes). Accordingly, these simulations used lateral boundary conditions from reanalysis products and are conducted in a manner similar to those used to develop regional climate projections (Pryor et al. 2023a) and/or mesoscale wind resources assessments (such as the New European Wind Atlas

(Dörenkämper et al. 2020; Hahmann et al. 2020)). The third study (study 3) applies and evaluates WRF in the context of day-ahead forecasting (i.e. short-term simulations performed within very high-fidelity lateral boundary conditions) and specifically focusses on forecast fidelity as a function of WRF model formulation. Based on considerations described above, all simulations were performed at so-called convection permitting model resolution (dx < 4 km). These studies are presented below to illustrate the types of data, methods and metrics that can be employed within a model V&V framework and to draw out inferences regarding use of NWP simulations for LEE erosion atlases and short-term forecasting for erosion safe mode operation in the SGP.

## 2.1   Study 1: Letson et al. (2020).

The initial study (Letson et al. 2020a; Letson et al. 2020b) provided the first assessment of the fidelity of the Weather Research and Forecasting (WRF) model with respect to the atmospheric drivers of wind turbine blade LEE. It comprised a 25-day simulation with an inner-most domain grid spacing (dx) of 1.33 km by 1.33 km. The simulation output at 10-minute intervals was evaluated relative to:

- Multiple products from nine dual polarization Doppler RADARs:

  - Composite RADAR reflectivity (cREF, decibels (dBZ)). High values of cREF and the coverage of high cREF were used to identify the presence and spatial extent of deep convection and heavy precipitation. This property is the maximum reflectivity in each vertical column and can be directly derived from measurements with RADAR. However, it must be computed using approximations based on cloud droplet properties in WRF simulations. The occurrence and spatial extent of cREF > 40 and 50 dBZ were employed as metrics of deep convection and, for the second threshold, a high likelihood of hail occurrence (Witt et al. 1998). The spatial patterns of the total frequency of occurrence of cREF above these thresholds over the 25-day period from RADAR and WRF were compared to assess whether preferred locations of deep convection were well-reproduced. Further comparisons included time series of the domain-wide total spatial extent of exceedance of the cREF thresholds in each 10-minute period to assess whether the time variation of the scale of deep convection was properly reproduced. Finally, cumulative probability distributions of cREF from areas surrounding individual RADAR and the corresponding WRF grid cells to quantify whether the dynamic range of cREF was accurately simulated.

  - Simulated spatial variability of total accumulated precipitation (mm in each WRF grid cell) and time variability in precipitation rate (mmhr$^{-1}$) across the simulation domain as derived from the WRF output were evaluated relative to RADAR estimates derived using observed reflectivity and Z-R relationships (NOAA 2016a). As with the cREF analyses, time series of domain-wide accumulated precipitation from WRF and RADAR were also compared to determine if the time variation (e.g. duration) of precipitation events was captured. Since the time series of cREF and precipitation are not drawn from Gaussian distributions, Spearman (rank) correlation coefficients were used in the skill assessment.

  - Hail occurrence/amount/size. The presence and geographical location (in latitude and longitude) of hail producing clouds is diagnosed from RADAR measurements based on reflectivity, aspect ratio of hydrometeors, vertically-

integrated liquid, and altitude of the melting layer (NOAA 2016b; Wallace et al. 2019; Witt et al. 1998). Where hail is diagnosed as present, RADAR-based estimated 75th percentile hailstone diameter (maximum estimated size of hail (MESH)) is also generated. Accumulated depth of hail at the ground and MESH can be output from WRF but are not directly comparable to the RADAR reports. Thus, total hail accumulation at the ground in each WRF grid column was compared to the number of RADAR hail reports within 100 km of each RADAR station and time series of hail occurrence within the domain from RADAR and WRF. Contingency tables, which is a matrix format table that displays multi-variate frequency distributions most usually for classed (or categorical) variables, and skill metrics for rare events were used to evaluate the simulations. Based on the generic example of a simple contingency table (Table 2), the following statistical metrics were computed and presented:

Proportion correct: $\quad C = \dfrac{a+d}{a+b+c+d}$ $\qquad$ (1)

Hit rate: $\quad H = \dfrac{a}{a+c}$ $\qquad$ (2)

False alarm rate: $\quad F = \dfrac{b}{b+d}$ $\qquad$ (3)

Odds ratio: $\theta = \dfrac{H}{1-H} \Big/ \dfrac{F}{1-F}$ $\qquad$ (4)

where *a* = number of hits (correct predictions of events), *b* = false alarms (predictions of events when none occurred), *c* = misses (event occurred without a prediction) and *d* = correct negatives (correct forecasts of no event).

**Table 2 Example contingency table.**

| Modeled↓ \ Observed→ | Event (e.g. hail) | No event (e.g. no hail) |
|---|---|---|
| Event (e.g. hail) | a | b |
| No event (e.g. no hail) | c | d |

- Wind speeds at 10-m height a.g.l. were evaluated relative to observations from nine two-dimensional sonic anemometers of the NWS Automated Surface Observation System (ASOS) (Schmitt and Chester 2009) using Spearman (rank) correlation coefficients for the time series at given locations. Cumulative density functions (CDF) of observed wind speeds at the ASOS stations were also compared with those from the WRF grid cells containing each ASOS station.

- Wind turbine electrical power production estimates from the Fitch wind farm parameterization in the WRF simulations (Fitch et al. 2012) were evaluated relative to observed wind energy power production in each 15 minute period as aggregated across the Electric Reliability Council of Texas (ERCOT) power system (Fertig 2019) again using Spearman correlation coefficients.

Key results of these analyses included:

- o The frequency of occurrence of high cREF is positively biased in the WRF simulations relative to the RADAR. This likely caused by errors in the representation of the size and number of cloud droplets produced by the Milbrandt-Yau (Milbrandt and Yau 2005a; Milbrandt and Yau 2005b)

microphysics scheme. This can cause biases in precipitation rates and hail occurrence (Tao et al. 2016) and was a primary motivator of study 3 which involved systematic assessments of different microphysics schemes across a range of convective environments.

○ In general, the spatial gradients in accumulated precipitation were reproduced in the simulations, but the precise timing (and location) of heavy precipitation was not well-captured.

○ Hours with WRF-simulated hail occurrence in 100-km radii around each of the nine RADAR stations exhibit a mean proportion correct of 0.77 (range of 0.69 to 0.84 across the nine RADARs) and the false alarm ratio ranges from 0.06 to 0.16. The mean odds ratio is 4.55 (range of 0.89 to 10.46). The odds ratio (Stephenson 2000) is even higher for the most intense hail events indicating good skill. However, there was evidence of excessive production of hail in the simulations.

○ Wind speeds at 10-m height from WRF exhibit relatively good, but spatially varying agreement, with ASOS observations both in terms of the CDF at point locations and the temporal variability. Spearman rank correlation coefficients between modeled and observed wind speeds at individual ASOS sites range from 0.21 to 0.58 (significantly different from zero at 99% confidence level). Wind climates exhibited equal fidelity during precipitation and no precipitation periods.

○ The overall Spearman rank correlation coefficient for wind power output time series derived from the Fitch wind farm parameterization in WRF and reported by the ERCOT grid is 0.52 which is significantly different from zero at the 99% confidence level according to a permutation test (Wilks 2020). When a period of wind speeds close to wind turbine cut-out is removed the Spearman correlation coefficient increases to 0.63. Fidelity in terms of power production is not only symptomatic of fidelity for hub-height wind speeds but is essential to understanding the power loss associated with use of erosion safe mode.

The relatively short duration of the simulation precluded detailed investigation of the size of hail (MESH) and the joint occurrence of precipitation and power producing wind speeds. These issues were subsequently addressed in study 2.

## 2.2 Study 2: Pryor et al. (2023).

The second study (Pryor et al. 2023b) involved WRF simulations using a similar configuration to study 1 but covering a wider range of climates by sampling multiple months. It also employed many of the same evaluation datasets, methods and metrics. To avoid model drift, cold restarts with new initial conditions were implemented every 14 days with a 6-hour spin-up period. The entire paper is available in Appendix A. Thus, only a brief precis of key findings is given here:

○ The frequency of occurrence of hail as a function of wind speed is well represented in the WRF simulation. This is an important finding, and important to accuracy of erosion atlases, because the closing velocity between hydrometeors and the blade is highly non-linear with wind speed as is the material stress associated with hail impacts.

○ The WRF simulation overestimates the probability of occurrence of large MESH during the winter months (January and February) but underestimates

the probability of occurrence of large MESH in the transition and summer months. If found to be a generalizable, this finding has high relevance to assessment of the seasonality of coating damage due to hail impacts. A further inference is that testing of other microphysics schemes would have high value.

- o The simulated frequency of liquid precipitation (of any intensity) during 10-m wind speeds above 7 ms$^{-1}$ exhibits a positive bias relative to RADAR-based observations close to each of the ASOS stations where wind speeds are measured. However, comparisons at the highly instrumented Department of Energy site at Lamont in Oklahoma indicated a negative bias in the occurrence of heavy precipitation at high wind speeds from WRF. The implication is that simulation fidelity with respect to these joint probabilities is highly spatially varying. Thus, any resulting erosion atlas would not be equally robust across space. Longer simulations would be useful in assessing whether this spatial variability across the precipitation gradient is persistent.

## 2.3  Study 3: Pryor et al. (2024) and Zhou et al. (2024).

The third study (Pryor et al. 2024; Zhou et al. 2024) (see Appendix B) involved conducting WRF simulations using a set-up similar to what would be employed in short-term (i.e. day-ahead) forecasting for wind power production (Jacondino et al. 2021; Tuncar; Sağlam; Oral 2024). These simulations were performed for case studies of meteorological events that are likely to have been associated with large increments in accumulated distance to failure of blade coatings (i.e. deep convection, heavy precipitation, hail and wind speeds at close where wind turbine blades reach maximum rotational speed (Letson and Pryor 2023)) and were designed to determine how fidelity varied across simulations conducted with five different microphysical schemes. Key findings included:

- o Model fidelity, particularly with respect to cREF and precipitation rates, is higher for deep convection events with strong large-scale (synoptic) forcing. Additionally, differences between 24-hour accumulated precipitation and cREF from simulations with different microphysics schemes were more marked during meteorological conditions that have weaker synoptic forcing and hence local land conditions play a larger role in determining the location and intensity of deep convection. This has key importance to the relative ability to make reliable forecasts of erosive events as a function of season.

- o For the springtime event with strong synoptic forcing, the time evolution spatially averaged precipitation rates from the WRF ensemble members exhibit relatively good agreement with data from nine RADARs. However, all ensemble members overestimate the peak precipitation rates. The rate of hail fall is best reproduced in simulations with Milbrandt-Yau (Milbrandt and Yau 2005a; Milbrandt and Yau 2005b) and Morrison (Morrison; Thompson; Tatarskii 2009) microphysics schemes. This might indicate that erosion atlases might be more robust when predicated on use of one of these two microphysics schemes.

- o Simulations of meteorological conditions with more locally-forced convection exhibit a positive bias in terms of total accumulated precipitation and the spatial occurrence of hail and graupel except for simulations with the Morrison microphysics scheme. This has key importance to the relative ability to make

reliable forecasts of erosive events as a function of season, since strong synoptic forcing is more frequent outside of the summer months (Zhou et al. 2024).

## 3. Key Conclusions/Recommendations

Heavy rainfall and hail during convective events are challenging for numerical models to simulate in both space and time. For the wind turbine blade LEE application, fidelity is also required with respect to hail size and joint probabilities of wind speed and hydrometeor type and precipitation rates. This demands fidelity that is seldom evaluated and thus there is a need to develop robust V&V frameworks that focus on LEE applications. Research summarized herein presents the initial steps towards developing such frameworks. These studies also illustrate that WRF simulations performed at high spatial resolution (dx $\approx$ 1-2 km) and with appropriate configuration settings exhibit fidelity for the marginal probabilities of wind speed, precipitation rate and hail occurrence. However, the fidelity with which the joint probabilities of these properties and the simulation of maximum size of hail is, as yet, not sufficient to characterize potential damage to wind turbine blade coatings.

Our recommendations are:

- Future research should develop and employ V&V frameworks that:

  - Focus on copula (joint) probability distributions of wind speed-precipitation rate.

  - Include explicit consideration of hail frequency/occurrence and size (where relevant).

  - Employ robust and appropriate statistical methods to assess skill. Use of Reliability Diagrams (Coburn and Pryor 2022; Coburn; Arnheim; Pryor 2022) would yield important insights and extend beyond techniques described above for relative rare events.

  - Address the different needs of communities seeking to develop erosion atlases and those seeking to inform implementation of erosion safe mode operation.

- Future research should also encapsulate a comprehensive assessment of fidelity as a function of model configuration across multiple climates and event 'types'. The design of such experiments could usefully leverage and adapt that used within the New European Wind Atlas (NEWA) (Dörenkämper et al. 2020; Hahmann et al. 2020).

These measures will advance our ability to make robust erosion atlases using NWP models and advance the case for short-term forecasting to be expanded to include information pertinent for erosion safe mode implementation.

## 4. References

Adams-Selin, R. D., A. J. Clark, C. J. Melick, S. R. Dembek, I. L. Jirak, and C. L. Ziegler, 2019: Evolution of WRF-HAILCAST during the 2014–16 NOAA/hazardous weather testbed spring forecasting experiments. *Weather and Forecasting*, **34,** 61-79.

Ansari, Q. M., F. Sánchez, L. Mishnaevsky Jr, and T. M. Young, 2024: Evaluation of offshore wind turbine blades coating thickness effect on leading edge

protection system subject to rain erosion. *Renewable Energy*, **226,** 120378, doi: 10.1016/j.renene.2024.120378.

Bang, S. D., and D. J. Cecil, 2019: Constructing a multifrequency passive microwave hail retrieval and climatology in the GPM domain. *Journal of Applied Meteorology and Climatology*, **58,** 1889-1904.

Bartolomé, L., and J. Teuwen, 2019: Prospective challenges in the experimentation of the rain erosion on the leading edge of wind turbine blades. *Wind Energy*, **22,** 140-151.

Bech, J. I., C. B. Hasager, and C. Bak, 2018: Extending the life of wind turbine blade leading edges by reducing the tip speed during extreme precipitation events. *Wind Energy Science*, **3,** 729-748.

Carvalho, D., A. Rocha, M. Gomez-Gerteira, and C. Santos, 2012: A sensitivity study of the WRF model in wind simulation for an area of high wind energy. *Environmental Modelling and Software*, **33,** 21-34.

Coburn, J., and S. C. Pryor, 2022: Do Machine Learning Approaches Offer Skill Improvement for Short-Term Forecasting of Wind Gust Occurrence and Magnitude? *Weather and Forecasting*, **37,** 525-543.

Coburn, J., J. Arnheim, and S. C. Pryor, 2022: Short-term forecasting of wind gusts at airports across CONUS using machine learning. *Earth and Space Science*, **9,** e2022EA002486, 10.1029/2022EA002486.

Dai, Y., I. N. Williams, and S. Qiu, 2021: Simulating the effects of surface energy partitioning on convective organization: Case study and observations in the US Southern Great Plains. *Journal of Geophysical Research: Atmospheres*, **126,** e2020JD033821.

Davenport, C. E., 2021: Environmental Evolution of Long-Lived Supercell Thunderstorms in the Great Plains. *Weather and Forecasting*, **36,** 2187-2209, 10.1175/waf-d-21-0042.1.

Dörenkämper, M., and Coauthors, 2020: The Making of the New European Wind Atlas - Part 2: Production and Evaluation. *Geoscientific Model Development*, **13,** 5079-5102, 10.5194/gmd-13-5079-2020.

Feng, Z., L. R. Leung, R. A. Houze Jr, S. Hagos, J. Hardin, Q. Yang, B. Han, and J. Fan, 2018: Structure and evolution of mesoscale convective systems: Sensitivity to cloud microphysics in convection-permitting simulations over the United States. *Journal of Advances in Modeling Earth Systems*, **10,** 1470-1494.

Fertig, E., 2019: Simulating subhourly variability of wind power output. *Wind Energy*, **22,** 1275-1287, 10.1002/we.2354.

Fitch, A. C., J. B. Olson, J. K. Lundquist, J. Dudhia, A. K. Gupta, J. Michalakes, and I. Barstad, 2012: Local and Mesoscale Impacts of Wind Farms as Parameterized in a Mesoscale NWP Model. *Monthly Weather Review*, **140,** 3017-3038, 10.1175/mwr-d-11-00352.1.

Gagne, D. J., A. McGovern, S. E. Haupt, R. A. Sobash, J. K. Williams, and M. Xue, 2017: Storm-based probabilistic hail forecasting with machine learning applied to convection-allowing ensembles. *Weather and Forecasting*, **32,** 1819-1840.

Hahmann, A. N., and Coauthors, 2020: The making of the New European Wind Atlas – Part 1: Model sensitivity. *Geoscientific Model Development*, **13,** 5053-5078, 10.5194/gmd-13-5053-2020.

Herring, R., K. Dyer, F. Martin, and C. Ward, 2019: The increasing importance of leading edge erosion and a review of existing protection solutions. *Renewable*

*and Sustainable Energy Reviews*, **115,** 109382 doi: 10.1016/j.rser.2019.109382.

Heymsfield, A., M. Szakáll, A. Jost, I. Giammanco, and R. Wright, 2018: A comprehensive observational study of graupel and hail terminal velocity, mass flux, and kinetic energy. *Journal of the Atmospheric Sciences*, **75,** 3861-3885.

Jacondino, W. D., A. L. da Silva Nascimento, L. Calvetti, G. Fisch, C. A. A. Beneti, and S. R. da Paz, 2021: Hourly day-ahead wind power forecasting at two wind farms in northeast Brazil using WRF model. *Energy*, **230,** 120841, https://doi.org/120810.121016/j.energy.122021.120841.

Jiménez, P. A., and J. Dudhia, 2013: On the ability of the WRF model to reproduce the surface wind direction over complex terrain. *Journal of Applied Meteorology and Climatology*, **52,** 1610-1617.

Katsivalis, I., A. Chanteli, W. Finnegan, and T. M. Young, 2022: Mechanical and interfacial characterisation of leading-edge protection materials for wind turbine blade applications. *Wind Energy*, **25,** 1758-1774.

Keegan, M. H., D. Nash, and M. Stack, 2013: On erosion issues associated with the leading edge of wind turbine blades. *Journal of Physics D: Applied Physics*, **46,** 383001, doi: 10.1088/0022-3727/46/38/383001.

Kim, H., and K. T. Kedward, 2000: Modeling hail ice impacts and predicting impact damage initiation in composite structures. *AIAA journal*, **38,** 1278-1288.

Kumjian, M. R., and K. Lombardo, 2020: A hail growth trajectory model for exploring the environmental controls on hail size: Model physics and idealized tests. *Journal of the Atmospheric Sciences*, **77,** 2765-2791.

Letson, F., and S. C. Pryor, 2023: From Hydrometeor Size Distribution Measurements to Projections of Wind Turbine Blade Leading Edge Erosion. *Energies*, **5,** 3906, https://doi.org/10.3390/en16093906.

Letson, F., R. J. Barthelmie, and S. C. Pryor, 2020: RADAR-derived precipitation climatology for wind turbine blade leading edge erosion. *Wind Energy Science*, **5,** 331-347.

Letson, F., T. J. Shepherd, R. J. Barthelmie, and S. C. Pryor, 2020a: WRF modelling of deep convection and hail for wind power applications. *Journal of Applied Meteorology and Climatology*, **59,** 1717-1733.

Letson, F., T. J. Shepherd, R. J. Barthelmie, and S. C. Pryor, 2020b: Modelling hail and convective storms with WRF for wind energy applications. *Journal of Physics: Conference Series*, **1452,** 012051 doi: 012010.011088/011742-016596/011452/012051/012051.

Macdonald, J., and M. Stack, 2021: Some thoughts on modelling hail impact on surfaces. *Journal of Bio-and Tribo-Corrosion*, **7,** 1-7, doi: 10.1007/s40735-020-00458-4.

Major, D., J. Palacios, M. Maughmer, and S. Schmitz, 2021: Aerodynamics of leading-edge protection tapes for wind turbine blades. *Wind Engineering*, **45,** 1296-1316.

Milbrandt, J., and M. Yau, 2005a: A multimoment bulk microphysics parameterization. Part II: A proposed three-moment closure and scheme description. . *Journal of the Atmospheric Sciences*, **62,** 3065-3081.

Milbrandt, J. A., and M. K. Yau, 2005b: A Multimoment Bulk Microphysics Parameterization. Part I: Analysis of the Role of the Spectral Shape Parameter. *Journal of the Atmospheric Sciences*, **62,** 3051-3064, 10.1175/JAS3534.1.

Morrison, H., G. Thompson, and V. Tatarskii, 2009: Impact of cloud microphysics on the development of trailing stratiform precipitation in a simulated squall line: Comparison of one-and two-moment schemes. *Monthly Weather Review*, **137,** 991-1007.

Morrison, H., and Coauthors, 2020: Confronting the challenge of modeling cloud and precipitation microphysics. *Journal of Advances in Modeling Earth Systems*, **12,** e2019MS001689.

Nielsen, J. S., D. Tcherniak, and M. D. Ulriksen, 2020: A case study on risk-based maintenance of wind turbine blades with structural health monitoring. *Structure and Infrastructure Engineering*.

NOAA, 2016a: Federal Meteorological Handbook, No. 11  WSR-88D Meteorologic Observations Part A, System concepts, responsibilities, and procedures. FCM-H11A-2016, Washington, DC, 25 pp.

——, 2016b: Federal Meteorological Handbook, No. 11  WSR-88D Meteorologic Observations Part C, Products and Algorithms. FCM-H11A-2016, Washington, DC, 25 pp.

Papaelias, M., and F. P. G. Márquez, 2020: Wind turbine inspection and condition monitoring. *Non-Destructive Testing and Condition Monitoring Techniques for Renewable Energy Industrial Assets*, Elsevier, 19-29.

Prein, A., R. Rasmussen, D. Wang, and S. Giangrande, 2021: Sensitivity of organized convective storms to model grid spacing in current and future climates. *Philosophical Transactions of the Royal Society A*, **379,** 20190546.

Pryor, S. C., and A. N. Hahmann, 2019: Downscaling wind. *Oxford Research Encyclopedia, Climate Science*, H. von Storch, Ed., Oxford University Press.

Pryor, S. C., J. J. Coburn, and R. J. Barthelmie, 2025: Spatiotemporal Variability in Wind Turbine Blade Leading Edge Erosion. *Energies*, **18,** 425, https://doi.org/10.3390/en18020425.

Pryor, S. C., J. J. Coburn, R. J. Barthelmie, and T. J. Shepherd, 2023a: Projecting Future Energy Production from Operating Wind Farms in North America: Part 1: Dynamical Downscaling. *Journal of Applied Meteorology and Climatology*, **62,** 63-80, 10.1175/jamc-d-22-0044.1.

Pryor, S. C., F. Letson, T. Shepherd, and R. J. Barthelmie, 2023b: Evaluation of WRF simulation of deep convection in the US Southern Great Plains. *Journal of Applied Meteorology and Climatology*, **62,** 41-62.

Pryor, S. C., and Coauthors, 2022: Atmospheric Drivers of Wind Turbine Blade Leading Edge Erosion: Review and Recommendations for Future Research. *Energies*, **15,** 8553, https://doi.org/10.3390/en15228553.

Pryor, S. C., and Coauthors, 2024: Prioritizing Research for Enhancing the Technology Readiness Level of Wind Turbine Blade Leading-Edge Erosion Solutions. *Energies*, **17,** 6285, https://doi.org/10.3390/en17246285.

Sareen, A., C. A. Sapre, and M. S. Selig, 2014: Effects of leading edge erosion on wind turbine blade performance. *Wind Energy*, **17,** 1531-1542.

Savana, R., 2022: Effect of Hail Impact on Leading Edge Polyurethane Composites, TUDelft, Available from http://repository.tudelft.nl/. 126 pp.

Scaff, L., A. F. Prein, Y. Li, C. Liu, R. Rasmussen, and K. Ikeda, 2020: Simulating the convective precipitation diurnal cycle in North America's current and future climate. *Climate Dynamics*, **55,** 369-382.

Schmitt, I. V., and V. Chester, 2009: A quality control algorithm for the ASOS ice free wind sensor. *13th Conference on Integrated Observing and Assimilation Systems for Atmosphere, Oceans, and Land Surface*, Phoenix, AZ, USA,

American Meteorological Society. Available from https://ams.confex.com/ams/89annual/techprogram/paper_145755.htm.

Shepherd, T., F. Letson, R. J. Barthelmie, and S. C. Pryor, 2024: How well are hazards associated with derechos reproduced in regional climate simulations? *Natural Hazards and Earth System Sciences*, **24,** 4473-4505.

Skamarock, W. C., and Coauthors, 2019: A Description of the Advanced Research WRF Version 4, 162 pp.

Snook, N., Y. Jung, J. Brotzge, B. Putnam, and M. Xue, 2016: Prediction and ensemble forecast verification of hail in the supercell storms of 20 May 2013. *Weather and Forecasting*, **31,** 811-825.

Stephenson, D. B., 2000: Use of the "odds ratio" for diagnosing forecast skill. *Weather and Forecasting*, **15,** 221-232.

Tao, W. K., D. Wu, S. Lang, J. D. Chern, C. Peters-Lidard, A. Fridlind, and T. Matsui, 2016: High-resolution NU-WRF simulations of a deep convective-precipitation system during MC3E: Further improvements and comparisons between Goddard microphysics schemes and observations. *Journal of Geophysical Research: Atmospheres*, **121,** 1278-1305.

Thacker, B. H., S. W. Doebling, F. M. Hemez, M. C. Anderson, J. E. Pepin, and E. A. Rodriguez, 2004: Concepts of model verification and validation, California, 41 pp.

Tuncar, E. A., Ş. Sağlam, and B. Oral, 2024: A review of short-term wind power generation forecasting methods in recent technological trends. *Energy Reports*, **12,** 197-209.

Wallace, R., K. Friedrich, E. A. Kalina, and P. Schlatter, 2019: Using operational radar to identify deep hail accumulations from thunderstorms. *Weather and Forecasting*, **34,** 133-150.

Wilks, D. S., 2020: *Statistical methods in the atmospheric sciences.* 4th ed. Elsevier, 840 pp.

Witt, A., M. D. Eilts, G. J. Stumpf, J. Johnson, E. D. W. Mitchell, and K. W. Thomas, 1998: An enhanced hail detection algorithm for the WSR-88D. *Weather and Forecasting*, **13,** 286-303.

Zhang, S., K. Dam-Johansen, S. Nørkjær, P. L. Bernad Jr, and S. Kiil, 2015: Erosion of wind turbine blade coatings–design and analysis of jet-based laboratory equipment for performance evaluation. *Progress in Organic Coatings*, **78,** 103-115.

Zhou, X., F. Letson, P. Crippa, and S. C. Pryor, 2024: Urban effect on precipitation and deep convective systems over Dallas-Fort Worth. *Journal of Geophysical Research: Atmospheres*, **129,** e2023JD039972, https://doi.org/039910.031029/032023JD039972.

Zhu, X., X. Fu, L. Liu, K. Xu, G. Luo, Z. Zhao, and W. Chen, 2022: Damage mechanism of composite laminates under multiple ice impacts at high velocity. *International Journal of Impact Engineering*, **168,** 104296, https://doi.org/10.1016/j.ijimpeng.2022.104296.

## Appendix A:

Reference: Pryor S.C., Letson F.W., Shepherd T. and Barthelmie R.J. (2023): Evaluation of WRF simulation of deep convection in the US Southern Great Plains. *Journal of Applied Meteorology and Climatology* **62** 41-62 doi: 10.1175/JAMC-D-22-0090.1 **© American Meteorological Society. Used with permission.**

# Evaluation of WRF Simulation of Deep Convection in the U.S. Southern Great Plains

S. C. PRYOR,[a] F. LETSON,[a] T. SHEPHERD,[a] AND R. J. BARTHELMIE[b]

[a] *Department of Earth and Atmospheric Sciences, Cornell University, Ithaca, New York*
[b] *Sibley School of Mechanical and Aerospace Engineering, Cornell University, Ithaca, New York*

ABSTRACT: The Southern Great Plains (SGP) region exhibits a relatively high frequency of periods with extremely high rainfall rates (RR) and hail. Seven months of 2017 are simulated using the Weather Research and Forecasting (WRF) Model applied at convection-permitting resolution with the Milbrandt–Yau microphysics scheme. Simulation fidelity is evaluated, particularly during intense convective events, using data from ASOS stations, dual-polarization radar, and gridded datasets and observations at the DOE Atmospheric Radiation Measurement site. The spatial gradients and temporal variability of precipitation and the cumulative density functions for both RR and wind speeds exhibit fidelity. Odds ratios > 1 indicate that WRF is also skillful in simulating high composite reflectivity (cREF, used as a measure of widespread convection) and RR > 5 mm h$^{-1}$ over the domain. Detailed analyses of the 10 days with highest spatial coverage of cREF > 30 dBZ show spatially similar reflectivity fields and high RR in both radar data and WRF simulations. However, during periods of high reflectivity, WRF exhibits a positive bias in terms of very high RR (>25 mm h$^{-1}$) and hail occurrence, and during the summer and transition months, maximum hail size is underestimated. For some renewable energy applications, fidelity is required with respect to the joint probabilities of wind speed and RR and/or hail. While partial fidelity is achieved for the marginal probabilities, performance during events of critical importance to these energy applications is currently not sufficient. Further research into optimal WRF configurations in support of potential damage quantification for these applications is warranted.

SIGNIFICANCE STATEMENT: Heavy rainfall and hail during convective events are challenging for numerical models to simulate in both space and time. For some applications, such as to estimate damage to wind turbine blades and solar panels, fidelity is also required with respect to hail size and joint probabilities of wind speed and hydrometeor type and rainfall rates (RR). This demands fidelity that is seldom evaluated. We show that, although this simulation exhibits fidelity for the marginal probabilities of wind speed, RR, and hail occurrence, the joint probabilities of these properties and the simulation of maximum size of hail are, as yet, not sufficient to characterize potential damage to these renewable energy industries.

KEYWORDS: Convective storms/systems; Radars/radar observations; Numerical analysis/modeling; Numerical weather prediction/forecasting; Renewable energy

## 1. Introduction

Organized convection is a major contributor to annual total precipitation and a source of very high rainfall rates (RR), hail, and high wind gusts over the Southern Great Plains (SGP) of the United States (Fig. 1). Indeed, mesoscale convective systems (MCSs) contribute 30%–70% of precipitation received during the warm season (defined as April to September) over a region extending from the Rocky Mountains east to the Mississippi River (Feng et al. 2019; Fritsch et al. 1986). The total accumulated precipitation from mesoscale organized convection during the 1982 warm season exceeded 30 cm over a vast swath of northeastern Texas and eastern Oklahoma and thus contributed nearly 50% of total annual precipitation (Fritsch et al. 1986). A more recent analysis has shown MCSs generate 30%–70% of warm-season precipitation and up to one-half of annual total precipitation over most of Texas and Oklahoma (Feng et al. 2021). Within the SGP, MCSs are most frequent in spring and are closely connected to the large-scale circulation

(Yang et al. 2017). MCSs during the spring and autumn "commonly initiate under strong baroclinic forcing and favorable thermodynamic environments" and "feature both large and deep convection, with a large stratiform rain area and high volume of rainfall" (Feng et al. 2019). Conversely, summer (June–August) "MCSs often initiate under weak baroclinic forcing, featuring a high-pressure ridge with weak low-level convergence acting on the warm, humid air associated with the low-level jet" (Feng et al. 2019).

Over the continental United States, hail damage produces approximately 60% of total annual property loss caused by severe weather (Murillo and Homeyer 2019). Both observations (e.g., estimates from the Global Precipitation Mission; Bang and Cecil 2019; Fig. 1a) and simulations indicate that severe hail occurs in the SGP on approximately 5% of all days (Prein and Holland 2018; Trapp et al. 2019). According to one prior study, parts of Oklahoma and Texas experience an average of one severe hail day per year, which is defined as a day with maximum estimated size of hail (MESH) above 29 mm (Cintineo et al. 2012). The U.S. National Oceanic and Atmospheric Administration (NOAA) documents "the occurrence of storms and other significant weather phenomena having

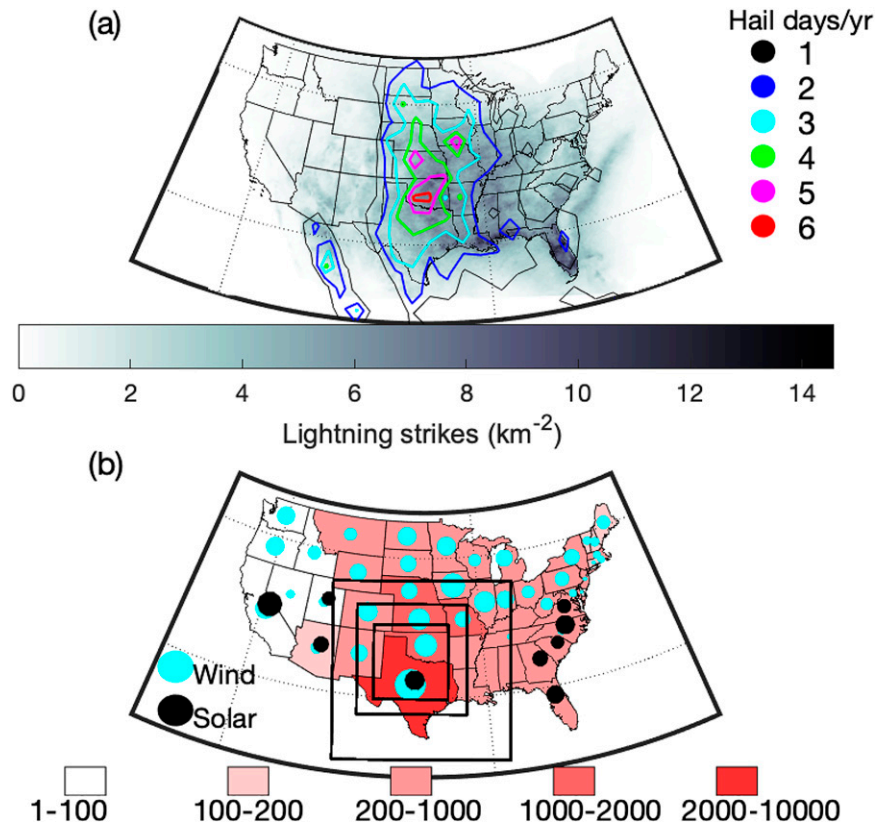*Corresponding author*: S. C. Pryor, sp2279@cornell.edu

FIG. 1. (a) Mean annual frequency of lightning strikes (2002–14) from the NLDN (Rudlosky and Fuelberg 2010) mapped to 12-km resolution. Also shown is the annual frequency of hail days derived from GPM data from 2014 to 2022 (contours). Note that these data have a spatial resolution of 2°. (b) Mean annual frequency (2005–21) of hailstorms and thunderstorms by state from the NOAA Storm Reports (red shading). Also shown are the state-by-state IC of wind energy (cyan) and solar (black; top 10 states only) as of the end of 2020 (American Clean Power 2021). The area of each dot is proportional to IC. Wind and solar installed capacities in Texas at the end of 2020 were 5.3 (solar) and 33 (wind) GW. The light-gray boxes indicate the Southern Great Plains and three domains used in the simulations with the WRF Model presented herein (see details in Fig. 2).

sufficient intensity to cause loss of life, injuries, significant property damage, and/or disruption to commerce" at the county level in the NOAA Storm Events Database (https://www.ncdc.noaa.gov/stormevents/). According to data from the associated NOAA Storm Reports for 2005–21, an average of over 2000 events described as "thunderstorms" or "hailstorms" occur in Texas per year (Fig. 1b).

The fidelity with which numerical models reproduce organized convection and associated hydrometeors remains comparatively poor even when regional models are applied at convection-permitting spatial scales (Scaff et al. 2020). Model fidelity is challenged by factors such as the complexity of cloud microphysics processes (Morrison et al. 2020; Tao et al. 2016) and strong, nonlinear atmosphere–surface coupling (Dai et al. 2021; Feng et al. 2018). Hail occurrence, number concentration, and diameter are particularly challenging to simulate (Adams-Selin et al. 2019; Gagne et al. 2017; Snook et al. 2016). This is in part because hail production and

indeed the environmental conditions responsible for hail generation and hail fall are still incompletely understood (Davenport 2021; Kumjian and Lombardo 2020). For example, even the 1D WRF-HAILCAST model, in which hail diameter is projected from modeled cloud liquid- and solid-phase water and vertical velocities, only achieved forecasts of hail sizes within 12 mm of measurements two-thirds of the time (Adams-Selin and Ziegler 2016).

Observational evidence suggests that the generation of cold pools caused in part by downdrafts' transport of cold, dry air from the middle troposphere toward the surface tends to be associated with precipitation rates $> 2$ mm h$^{-1}$ and is key to the organization of multicell convection (Schlemmer and Hohenegger 2014). Numerical simulations indicate a strong positive association between the updraft and downdraft area and cold-pool vertical extent and intensity (Marion and Trapp 2019), and that the ability of cold pools to initiate development of further convective cells and organize convection is critically
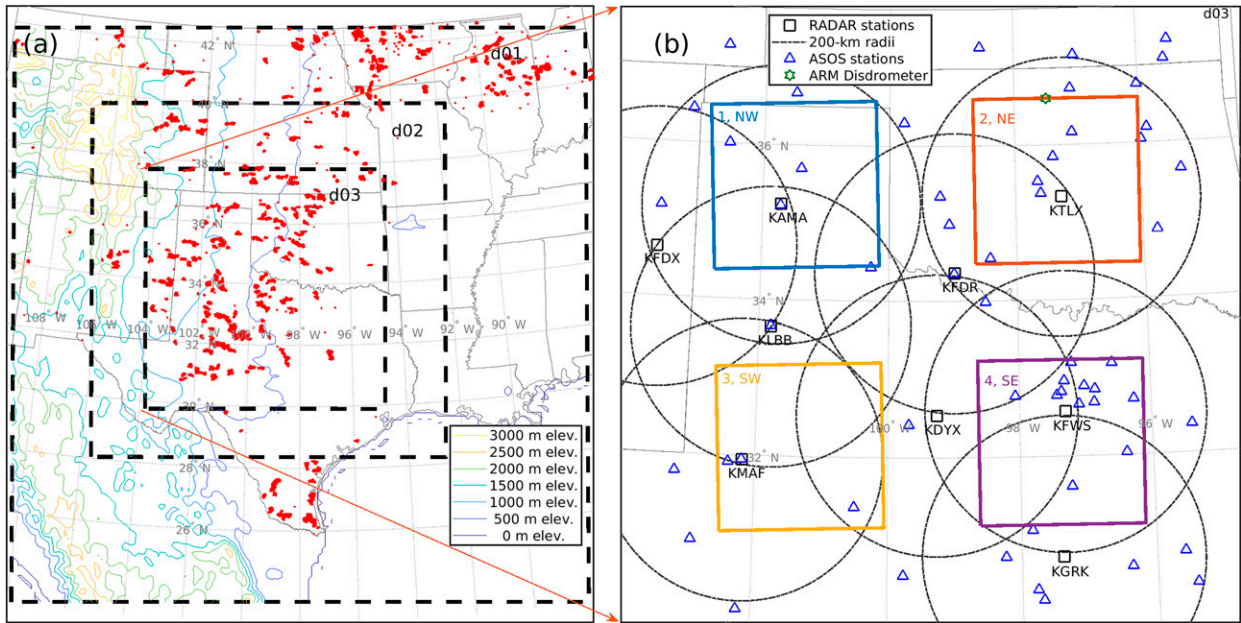
FIG. 2. (a) Topography in the simulation domains and location of wind turbines based on the USGS wind turbine database (Hoen et al. 2018), updated as of April 2022. (b) Locations of NWS ASOS and dual-polarization Doppler radar in domain d03 and the DOE ARM site at Lamont. Also shown are the four subregions—NW, NE, SW, and SE—that are used to examine the spatial variability in atmospheric conditions.

dependent on the cold-pool depth and advection speed (Haerter et al. 2019). Previous research focused on the SGP has found that the areal extent of stratiform precipitation associated with midlatitude deep convection tends to be underestimated in convection-permitting model simulations (i.e., with a grid spacing $\Delta x = 1$ km) performed with a wide array of microphysics schemes (Han et al. 2019). Conversely, simulations tend to produce excessively intense updraft velocities and too wide an area of high composite reflectivity (cREF > 45 dB$Z$; Fan et al. 2017). Numerical simulation of precipitation, advection speeds, cold-pool characteristics, and cloud properties associated with convective systems are substantially improved by use of so-called convection-permitting grid spacing and thus a decrease of $\Delta x$ from 12 to 4 km (Prein et al. 2021). MCS updraft and downdraft widths were smaller, the updraft depth was shallower, and the median updraft and downdraft velocities were slightly lower in simulations with $\Delta x = 1$ km, relative to those with $\Delta x = 4$ km (Prein et al. 2021). Decreasing $\Delta x$ from 4 km in simulations of MCSs led to improved representation of the updraft and downdraft properties relative to radar wind profiler observations in the SGP (Wang et al. 2020). Idealized simulations of individual thunderstorms also indicate that grid spacing of 1 km led to improved representation of deep convective structures relative to simulations at 2 km (Verrelle et al. 2015). Additional previous research found MCS simulation fidelity is enhanced by use of $\Delta x = 1$ km rather than 3 km due largely to better representation of the cold pool (Squitieri and Gallus 2020). Based on this research, a grid spacing of 1.3 km is used here in the innermost simulation domain.

There are clear societal needs with regard to high-fidelity short-term forecasts and climate-scale simulations of deep convection and the associated hazards. Specific to the SGP, Dallas–Fort Worth, Texas, suffered $800 million in hail damage in a single event in 2011 (Brown et al. 2015), and another event in May 1995 caused $2 billion of damage and 109 injuries (Edwards and Thompson 1998). The SGP is also characterized by large wind and solar resources and deployments (Figs. 1 and 2). Both exhibit vulnerability to damage from extremely heavy rainfall and hailstones associated with deep convection (Letson et al. 2020a,b; Makarskas et al. 2021). With respect to solar panels and both residential and commercial properties, the primary source of damage derives from kinetic energy transfer during hailstone impacts. Hence, the hydroclimatic parameters of interest are the hailstone diameter, mass, terminal fall velocity $v_t$, and number (Brown et al. 2015; Makarskas et al. 2021). For wind turbines, the damage is manifest as roughening of the wind turbine blade leading edge. This leading-edge erosion (LEE) is also, to the first order, the result of material stresses caused by kinetic energy transfer from falling hydrometeors. In this case, however, the closing velocity is dictated by both the hydrometeor $v_t$ and the blade rotational speed. The linear speed of the blade tip is zero at wind speeds below cut-in (when the wind turbine begins to generate electrical power), rises rapidly as wind speed increases, and then is constant at wind speeds above those where power output is equal to the rated capacity of the wind turbine (Fig. 3). Hydrometeor $v_t$ is lower than the wind turbine tip speed and thus plays a secondary, but important, role and is dictated by the diameter, phase, and density (Fig. 3).
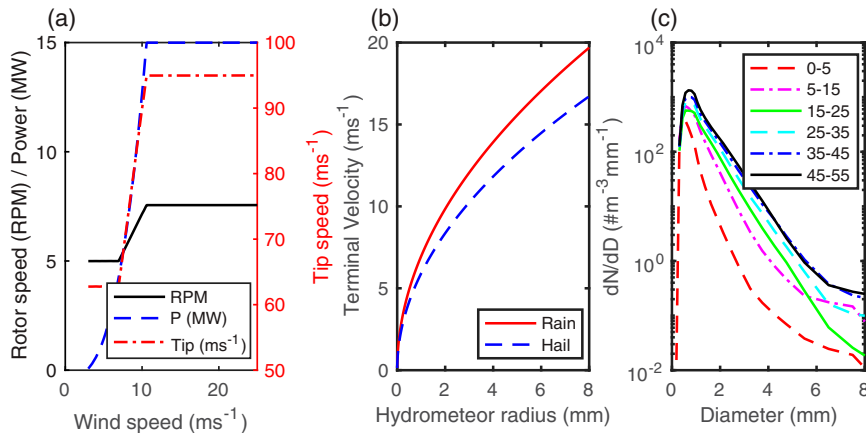
Fig. 3. (a) Wind turbine rotational speed [revolutions per minute (label RPM)], tip speed (label Tip; m s$^{-1}$), and electrical power production (label P; MW) as a function of wind speed for the International Energy Agency (IEA) 15-MW reference wind turbine (Gaertner et al. 2020). This reference turbine represents typical characteristics of a wind turbine that would generate 15 MW of electrical power under optimal wind conditions. Power production begins at ~4 m s$^{-1}$ and ceases at hub-height wind speeds > 25 m s$^{-1}$. Thus, no RPM or tip-speed data are plotted outside this range. (b) Illustrative terminal fall velocities for rain droplets and hail computed using $V_{t,\text{rain}} = k[(\rho_o/\rho_{\text{air}})R]^{1/2}$ and $V_{t,\text{hail}} = [(8/3)(|g|/C_D)(\rho_i/\rho_{\text{air}})R]^{1/2}$, where $R$ = droplet or hailstone radius (m), $k = 220$ m$^{1/2}$ s$^{-1}$, $\rho_o$ = air density at sea level (1.225 kg m$^{-3}$), $\rho_{\text{air}}$ = air density at the droplet altitude (0.999$\rho_o$), $\rho_i$ = density of ice (917 kg m$^{-3}$; Kumjian and Lombardo 2020; Shpund et al. 2019), and $C_D$ = drag coefficient with a value of 0.55 (Stull 2017) or 0.5 (Kumjian and Lombardo 2020). (c) Mean droplet number density as a function of RR (see legend) derived from the optical disdrometer deployed at the DOE ARM site at Lamont (Fig. 2) based on 1-min observations from 2017 to 2021.

The number of hydrometeors, mass, and phase are complex functions of cloud microphysics and environmental thermodynamics. The number density of larger, more massive droplets with higher $v_t$ increases rapidly with RR (Fig. 3).

Evidence that blade LEE may reduce annual electricity production from wind turbines by an average of 1%–5% (Froese 2018) has spurred development of advanced methods for detection (Du et al. 2020) and prevention/reduction by application of protective tapes (Major et al. 2021) and/or use of erosion-safe mode in wind farm control where the wind turbine rotational speed is reduced during extreme hydroclimatic events (Hasager et al. 2021; Tilg et al. 2020). To accurately project the relative cost–benefit of these actions requires both accurate forecasts 1) of the total accumulated kinetic energy that is likely to be transferred into the blades during their lifetime (20–30 yr) and 2) short-term forecasts of individual events that are likely to be highly erosive. Making an assessment of the former relies on correct representation of the marginal and joint probabilities of hub–height wind speeds, rainfall rates, and also hail occurrence and diameter (Letson et al. 2020a). For the latter, there is a need for fidelity at the event level to permit costing of decisions to slow the wind turbine blade rotation to reduce blade material stresses from hydrometeor impacts that also cause lost electricity production and revenue.

Previous research that estimated kinetic energy transfer to operating wind turbines in different regions within the contiguous United States using data from dual-polarization Doppler radar found particularly high values and hence LEE potential in the SGP due to the prevalence of high wind speeds, heavy rainfall, and hail (Letson et al. 2020a; Fig. 1a). Other atmospheric phenomena are also associated with wind turbine damage. These include lightning strikes that, like hail and high RR, are also associated with deep convection and have a relatively high frequency of occurrence in the SGP (Fig. 1a). Specific to the SGP, previous analyses have suggested that, in a location with an annual rate of 5–6 lightning strikes per kilometer squared, about 5% of 1.5-MW wind turbines in a wind farm experienced some level of lightning damage to their blades (Katsaprakakis et al. 2021). While a range of lightning protective measures are available (International Electrotechnical Commission 2019), lightning attachment to the tips of wind turbine blades can result in delamination (70% of cases in the SGP), debonding, and shell and/or tip detachment (Candela Garolera et al. 2016). Degradation of aerodynamic performance and uneven loading of the wind turbine is also associated with ice accumulation during periods of freezing rain. A range of mitigation measures can be deployed to reduce ice buildup (Madi et al. 2019), but in environments with high freezing-rain frequency and up to 3% of hours in a year exhibiting meteorological icing, annual electricity production can be reduced by up to 5% (Pedersen et al. 2022). A substantial fraction of U.S. National Weather Service (NWS) Automated Surface Observing System (ASOS) stations include an icing sensor that permits detection of freezing rain (Jones et al. 2004). Data from ASOS stations within the primary study region considered here

(domain d03; Fig. 2a) indicate that, during 2017, freezing rain was detected in an average of 0.08% of all 5-min periods. This suggests icing is likely not a dominant source of lost electricity production or increased wind turbine maintenance costs in the SGP. Here, we focus on the meteorological drivers of LEE.

Here, we present a WRF simulation comprising seven months during 2017. Our research objectives are to quantify the degree to which the simulation performs the following:

1) The simulation generates a realistic representation of the hydroclimate in terms of the frequency and intensity of precipitation and the occurrence of hail and maximum estimated size of hail as derived from in situ and remote sensing observations. Specifically, we test that our a priori postulates that
   - the positive bias in hail frequency and spatial extent found in a previous WRF simulation of June–July 2014 for this model configuration and study domain (Letson et al. 2020b), and also in a simulation also performed with the Milbrandt–Yau microphysics scheme of a severe hail event in Colorado (Labriola et al. 2019b), is manifest in all seasons,
   - model fidelity for these hydroclimate properties exhibits marked seasonality due to variations in the spatial extent of convection and degree of coupling to the larger-scale atmospheric environment (Feng et al. 2019), and
   - while model-derived cREF accurately reproduces the time evolution of radar-derived measurements, there is positive bias in the spatial extent of cREF > 30 dBZ (Fan et al. 2017).
2) The simulation exhibits skill for conditions during intense convective events. For the 10 dates with greatest spatial occurrence of composite reflectivity above 30 dBZ (Nisi et al. 2018), we provide detailed assessments of model skill, including hydrometeor type, and diagnose that skill in the context of convective duration and dynamics. Specifically, we test our a priori postulate that the WRF simulation reproduces the domainwide precipitation accumulation as reported in a range of observational datasets during these dates despite excessively intense updraft velocities and too wide an area of high composite reflectivity (cREF > 45 dBZ; Fan et al. 2017).
3) The simulation reproduces the joint probability distribution of hydroclimate parameters and wind speeds of particular importance to the wind energy industry. Our a priori postulate is that this simulation will, consistent with past evaluations of WRF applied at convection-permitting resolution over the SGP, exhibit substantial skill for the marginal probabilities of key hydroclimate parameters and wind speeds. However, we further postulate that the simulation of the joint probability distributions represents a substantially more stringent test of the model and will be less good especially in aspects critical to dictating wind turbine LEE. We further evaluate whether this WRF simulation represents key spatial gradients in the occurrence of highly erosive meteorological events (i.e., co-occurrence of high wind speeds and heavy rainfall/hail).

## 2. Data and methods

### a. WRF simulation

The simulation presented herein is performed using WRF (v3.8.1) with cold restarts every 14 days and a 6-h spinup period. Triple-nested simulation domains are used (Fig. 2 and Table 1). These domains are centered on a region with very high wind energy penetration. The entire outermost domain covers an area of 4.4 million $km^2$ and is centered on northern Texas. As of April 2022, this area contained almost 40 000 wind turbines with a cumulative installed capacity (IC) of >75 GW (Hoen et al. 2018). This is over 60% of the current total U.S. installed capacity (American Clean Power 2021). Over 42 GW from a total of >22 000 wind turbines is located within the innermost simulation domain (domain d03) that is the focus of analyses presented herein.

Simulation fidelity for deep convection and related hazards is generally improved by data assimilation (Segele et al. 2013; Snook et al. 2016). Here, we do not perform data assimilation since the goal of this work is to quantify inherent model skill. We note that previous simulations performed without data assimilation with the WRF Model at a grid spacing of 4 km indicate realistic representation of structure and frequency of precipitation associated with MCSs over the central United States (Yang et al. 2017).

The simulation settings are selected to provide consistency with a prior 25-day test simulation of summer conditions (8 June–2 July 2014) over the SGP. That simulation exhibited some degree of fidelity for key meteorological properties (Letson et al. 2020b). Specifically, precipitation accumulation and RR exhibit similar magnitudes and spatial patterns to those inferred from radar and tipping-bucket rain gauges. The spatial variability of near-surface wind speeds also exhibits relatively close agreement with in situ measurements. The mean odds ratio for hail prediction across 11 radar stations is 4.6, with a range of 0.89–10.46. However, a positive bias in terms of hail frequency and spatial extent is evident. The short duration of the simulation precluded evaluation of the joint probabilities of hail or RR and wind speeds. As in that work, and other recent regional simulations (Qiu et al. 2020; Zscheischler et al. 2021), initial and lateral boundary conditions (LBCs) for the simulation presented herein are provided from the ERA-Interim reanalysis (Dee et al. 2011) and are updated every 6 hours. Daily sea surface temperature data are provided by the Real-Time Global SST dataset (Reynolds and Chelton 2010). No nudging or data assimilation is applied. One-way nesting is used. Output for parameters analyzed herein is stored every 10 min.

The calendar year 2017 is selected based on analyses that indicate that it is representative of typical radar hail climate in the study region in terms of the seasonality and absolute number of hail reports in each calendar month (Fig. 4a). The original intent had been to simulate the entire period from January to September 2017 to sample months with varying amounts of deep convection, RR, and hail frequency. However, even using 45 vertical layers and short time steps $\Delta t$ led to violations of the Courant–Friedrichs–Lewy (CFL) condition [CFL = $c(\Delta t/\Delta z) \leq 1$], where $\Delta z$ = vertical grid spacing

TABLE 1. WRF simulation settings.

| Model attribute | Setting |
|---|---|
| **Domain settings** | |
| Grid spacing and domain size | Domain 1 (d01): 12 km (175 × 175 grid cells) |
| | Domain 2 (d02): 4 km (322 × 322 grid cells) |
| | Domain 3 (d03): 1.33 km (652 × 652 grid cells) |
| Vertical resolution | 45 vertical levels up to 50 hPa |
| Model time step (s; sd01, d02, d03) | 30, 10, 3.33 |
| **Model physics settings** | |
| Microphysics | Milbrandt–Yau (Milbrandt and Yau 2005) |
| Longwave radiation | RRTM (Mlawer et al. 1997) |
| Shortwave radiation | Dudhia (Dudhia 1989) |
| Time between radiation calls | 15 min |
| Surface layer | Revised MM5 Monin–Obukhov scheme (Jiménez et al. 2012) |
| Land surface | Noah land surface model (Niu et al. 2011) |
| No. of soil layers | 4 |
| No. of land categories | 21 (MODIS) |
| Planetary boundary layer | MYNN level 2.5 (called every time step; Nakanishi and Niino 2006) |
| Cumulus parameterization | Kain–Fritsch (domain d01 only; called every 5 min; Kain 2004; Kain and Fritsch 1993) |

when high vertical velocities $c$ are simulated (De Moura and Kubrusly 2013). Tests showed a much smaller time step ($\Delta t \sim 1$ s in the innermost domain) might allow simulation of April and May, but limitations on computational resources precluded doing so.

The five falling hydrometeors treated in the Milbrandt–Yau double-moment microphysics scheme are rain, ice, snow, graupel, and hail (Milbrandt and Yau 2005). This scheme performed relatively well in our prior evaluation (Letson et al. 2020b) and in terms of precipitation generation from a squall line in the SGP but underestimated the highest RR (Fan et al. 2017). An ensemble of simulations with data assimilation and

this microphysics scheme also exhibited fidelity in terms of hail occurrence and size for the supercell storms in the SGP on 20 May 2013 (Snook et al. 2016). The microphysics parameters are used to derive estimated radar reflectivity (at 10-cm wavelength) as a diagnostic output variable using the WRF "do_radar_ref=1" namelist setting (Koch et al. 2005; Min et al. 2015).

*b. Datasets used in the model evaluation*

Two datasets from the NWS ASOS network (Fig. 2) are presented here. Sustained wind speeds at 10 m above ground level (AGL) $U_{10}$ (m s$^{-1}$) as measured using Vaisala,
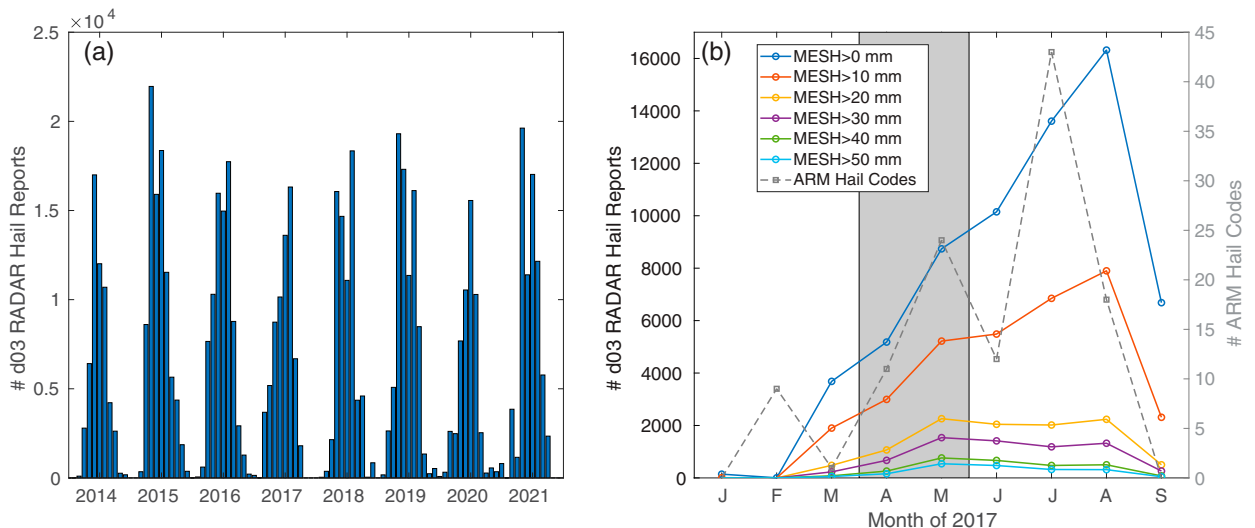


FIG. 4. (a) Monthly total radar-derived hail reports within domain d03 for 2014–21. (b) Frequency of radar hail reports in domain d03 and WMO hail codes from the optical disdrometer at the DOE ARM site (number of ARM hail codes) during January–September 2017. Colored lines denote the number of radar-derived hail reports with MESH > 0, 10, 20, 30, 40, and 50 mm. Months not simulated (April and May) are shown with a gray background.

Inc., 2D sonic anemometers and RR as sampled using a Frise Engineering Co. heated tipping-bucket rain gauge. These data are reported every 5 min and sampled at 10-min intervals for use in the WRF evaluation.

Inferred radar reflectivity, precipitation type, and RR from the WRF simulation are evaluated using nine NWS S-band dual-polarization Doppler radars (WSR-88D; Fig. 2b). The following data products from within 200 km of each radar station are regridded onto the WRF grid within domain d03 and sampled at a 10-min resolution:

1) reflectivity (dB$Z$) at six elevation angles (0.5°–3.1°),
2) cREF [dB$Z$; based on previous radar-based analyses that have employed a cREF threshold of 30 dB$Z$ as an index of storm initiation (Nisi et al. 2018), we use this threshold as an indicator of convective activity],
3) RR (mm h$^{-1}$) and total monthly precipitation accumulation [the minimum RR identified by the WSR-88D rainfall algorithm is 0.2544 mm h$^{-1}$ (0.01 in. h$^{-1}$; Fulton et al. 1998); RR are reported in 16 classes (defined in inches per hour) at 0, 2.54, 6.36, 12.7, 19.1, 25.4, 31.8 38.2, 44.5, 50.9, 63.6, 76.3, 102, 153, and 204 mm h$^{-1}$],
4) hail reports issued based on reflectivity, hydrometeor aspect ratio, vertically integrated liquid water content, and altitude of the melting layer (Crum et al. 1998; NOAA 2017; Seo et al. 2015; Wallace et al. 2019; Witt et al. 1998) [these reports include only the geographic centroid of the cell in which hail is inferred and the maximum expected hail size, which is the diameter that 75% of observed hail diameters should fall below (Ortega 2018; Wendt and Jirak 2021)], and
5) Hybrid hydrometeor classification (HHC; Park et al. 2009) [here, we present data on four of the HHC classes: hail, graupel, snow, and rain; graupel is differentiated from hail using a diameter threshold of 5 mm (American Meteorological Society 2015)].

The radar hail reports do not include the geographic extent of hail, and multiple studies have found spatial mismatches between hail swaths inferred from radar and surface hail reports due to melting between the radar detection height and the ground, the complexity and possible errors in the hail detection algorithm, and horizontal advection of hail stones as they fall (Adams-Selin et al. 2019; Brook et al. 2021). Nevertheless, dual-polarization radar is widely considered to be the best dataset for characterization of hail climates and to provide evaluation of numerical models (Murillo and Homeyer 2019). When comparing the spatial extent of hail from WRF and radar, each radar hail report is assumed to cover an area equal to 45 domain d03 grid cells or 76 km$^2$. This scaling factor is based on 1) the median size of contiguous grid cells in the WRF simulation with cREF > 40 dB$Z$, which has been used as threshold for radar hail detection (Witt et al. 1998), and 2) climatologies of hail production from southern France that found a typical storm produces hail over a 6-km-wide swath, has an average advection speed of 15 m s$^{-1}$, has a duration of 14 min (yielding a distance of 13 km), and also gives an areal extent of 76 km$^2$ (Dessens 1986). This estimate is

naturally a first-order approximation, and we do not imply that such an area would be simultaneously subject to hailfall at the ground.

Many of the fidelity assessments for precipitation presented here use radar observations because it is available with high temporal resolution (<10 min) and is available over almost all of the domain. It also provides consistency with other analyses that employ radar estimates of cREF, reflectivity, and/or hail occurrence. Nevertheless, radar-derived RR have a number of uncertainties associated with them. Thus, we also use two gridded precipitation datasets: Integrated Multi-satellitE Retrievals for the Global Precipitation Measurement (GPM) mission (IMERG; Huffman et al. 2020b). We use the multisatellite precipitation estimate with gauge calibration—precipitationCal (Huffman et al. 2020a). The data are archived at a 0.1° by 0.1° spatial resolution and a 30-min temporal resolution and have units of millimeters per hour. The IMERG data also have a quality assurance index (0–1) associated with each record, with higher values indicating higher data quality (Huffman 2019; Huffman et al. 2019a). The mean value of the data-quality flag in grid cells where nonzero precipitation occurs during the 10 days analyzed herein ranges from 0.41 (24 June) to 0.67 (29 March). Thus, based on preliminary guidance, these data are treated as being of moderate quality. We also analyze the Stage IV NCEP/Environmental Modeling Center (EMC) product that merges observations from 140 radars and ~5500 rain gauges over the continental United States (Lin and Mitchell 2005). It has a 4 km × 4 km spatial resolution and hourly temporal resolution and has been used as a reference against which other datasets are evaluated (Beck et al. 2019).

The U.S. Department of Energy operates an Atmospheric Radiation Measurement (ARM) hub within the SGP near Lamont, Oklahoma (36.6072°N, −97.4875°E; Fig. 2b). At this site an optical (Parsivel$^2$) disdrometer (Bartholomew 2020; Tokay et al. 2014) measures droplet counts in 32 classes and also encodes the presence of hail using the WMO synoptic present weather code 89. Wind speeds close to the mean wind turbine hub height (90 m AGL) are measured using a Halo Photonics Doppler lidar (Newsom and Krishnamurthy 2020).

### c. Analysis methods and skill metrics

The seven simulated months are divided into three seasons. Winter is defined as January and February and has a low hail prevalence. Summer is defined as June, July, and August, has the highest hail frequency (Fig. 4b), and lies within what is frequently referenced as the "warm" season where convection is frequent across the contiguous United States (Goines and Kennedy 2018). A transition season is defined as March and September. Both months have a moderate frequency of hail reports. These definitions are also largely consistent with the seasonality of environmental contexts/spatial extents of MCS that is described above (Feng et al. 2019).

Four subregions within domain d03 (Fig. 2b) are used to examine the degree to which the WRF simulation captures spatial gradients in the wind and hydroclimate. These subregions

are each 260 km by 260 km square and are located in the center of the four quadrants of domain d03. Observational data from these subregions illustrate marked west–east gradients of precipitation (Sun et al. 2016). For example, the mean annual total precipitation at the four ASOS stations closest to the center of the subregions computed for 2005–21 is 480, 764, 379, and 932 mm for northwest (NW), northeast (NE), southwest (SW), and southeast (SE), respectively. The wind resource and mean wind speed exhibit a northwest-to-southeast gradient across domain d03, with localized enhancement along the coast (Pryor et al. 2020). For example, the mean annual frequencies of wind speeds at 10 m AGL greater than 10 m s$^{-1}$ at those same ASOS stations are 7.8%, 5.1%, 3.4%, and 1.4%, respectively. The number of wind turbines and total installed capacity (April 2022) of wind turbines in these subregions of domain d03 are >2600 and >5 GW for NW, >2100 and >3.9 GW for NE, 5809 and >10 GW for SW, and 680 and >1.2 GW for SE.

Simulation fidelity assessment focuses on four core aspects:

1) The first aspect is climatology and marginal probability distributions of key parameters. Spatial maps of seasonal total precipitation and cumulative density functions (CDFs) of RR and MESH from WRF are compared with estimates from radar while CDF of wind speeds are compared with those from ASOS. These assessments are performed domainwide and in the four subregions. Rank (Spearman) correlation coefficients are used in the evaluation because these variables are not Gaussian distributed (Wilks 2020).

2) Another aspect is forecast accuracy. Time series of domainwide occurrence of high cREF and RR are used to assess temporal fidelity and to identify 10 days with widespread deep convection. Some analyses employ metrics based on contingency tables of categorical events in each 10-min period: i) occurrence of hail, i.e., any hail accumulation in WRF or one or more hail reports from radar; ii) deep convection where cREF > 30 dBZ covers 5% or more of d03 in either the radar mapped to the WRF grid or in the WRF simulation output; and iii) RR > 5 mm h$^{-1}$ over 5% or more of domain d03. In these cases, model skill is summarized using hit rate

$$H = \frac{a}{a + c}, \tag{1}$$

false alarm rate

$$F = \frac{b}{b + d}, \tag{2}$$

and odds ratio (Stephenson 2000)

$$\theta = \frac{H}{1 - H} \bigg/ \frac{F}{1 - F}, \tag{3}$$

where $a$ is the number of correct forecasts, $b$ is the number of event forecasts when none occurred, $c$ is the events that occurred but are not forecast, and $d$ is correct negatives, respectively. The odds ratio is the "odds of making

a good forecast (a hit) to the odds of making a bad forecast (a false alarm)" (Stephenson 2000). The term $\theta = 1$ indicates independence of forecasts and observations, whereas $\theta$ values > 1 reflect increased association and increasing forecast skill. Confidence intervals are derived for the natural logarithm of $\theta$ because it more closely approximates a Gaussian distribution (Agresti 2018) as

$$\ln(\theta) \pm z_{\alpha/2} \times SE, \tag{4}$$

where $z_{\alpha/2}$ is the value drawn from a $z$ distribution at a confidence level specified by $\alpha$ (1.96 for 95% confidence level and 1.64 for 90% confidence level) and SE is the standard error that is computed from the contingency table values ($a$, $b$, $c$, and $d$) as

$$SE = \sqrt{\frac{1}{a} + \frac{1}{b} + \frac{1}{c} + \frac{1}{d}}. \tag{5}$$

3) Another aspect is intense events. The 10 dates with highest coverage of radar-derived cREF > 30 dBZ (Fig. 5h) are (listed in descending order of the spatial coverage) 29 March, 14 February, 20 February, 15 January, 24 June, 16 January, 4 July, 6 August, 26 September, and 7 August. For these 10 days we analyze the relative spatial coverage of high RR and reflectivity, examine hydrometeor type, and provide cross-sectional transects through regions with high reflectivity.

4) The final aspect is the joint probabilities of wind speed, RR, and hail occurrence.

Analyses presented here use different RR thresholds. RR > 0 mm h$^{-1}$ is the natural definition, but even when models are applied at convection-permitting scales the excess drizzle problem is not entirely removed (Meredith et al. 2020). The 1 mm h$^{-1}$ threshold is the American Meteorological Society definition of the highest RR associated with drizzle, which is defined as comprising precipitation with droplet diameters of <0.5 mm (Huschke 1959). A threshold of 5 mm h$^{-1}$ is defined as heavy rainfall by the U.S. Geological Survey. A RR of 5 mm h$^{-1}$ is also approximately the midpoint of the World Meteorological Organization definition of moderate rainfall, which is defined as RR of 2.5–10 mm h$^{-1}$ sustained for 3 min.

Joint probability distributions are computed for the ARM site using the disdrometer and wind speeds at 90 m AGL and WRF output for the grid cell containing Lamont as well as output for all of domain d03 and subregions therein. These latter analyses use wind speeds at 10 m AGL from ASOS and RR from radar versus WRF output. In these analyses RR classes are chosen to emphasize the heaviest rainfall events. Thus, the RR classes are >0–5 mm h$^{-1}$, and in 10 mm h$^{-1}$ the classes are centered on 10, 20, 30, 40, and 50 mm h$^{-1}$. These are defined based, in part, on analyses of disdrometer data from the ARM site (2017–21). Of the 2 436 497 one-minute data records, 102 899 (~4%) indicate the presence of precipitation. For RR of 0–5, 5–15, 15–25, 25–35, 35–45, and 45–55 mm h$^{-1}$, the mean number density of rain droplets in a diameter $D$ class centered at 3.75 mm is 0.172, 1.53, 3.99, 7.46, 11.0, and 12.6 m$^{-3}$ mm$^{-1}$, respectively (Fig. 3c). There are 457 occurrences of hail, and
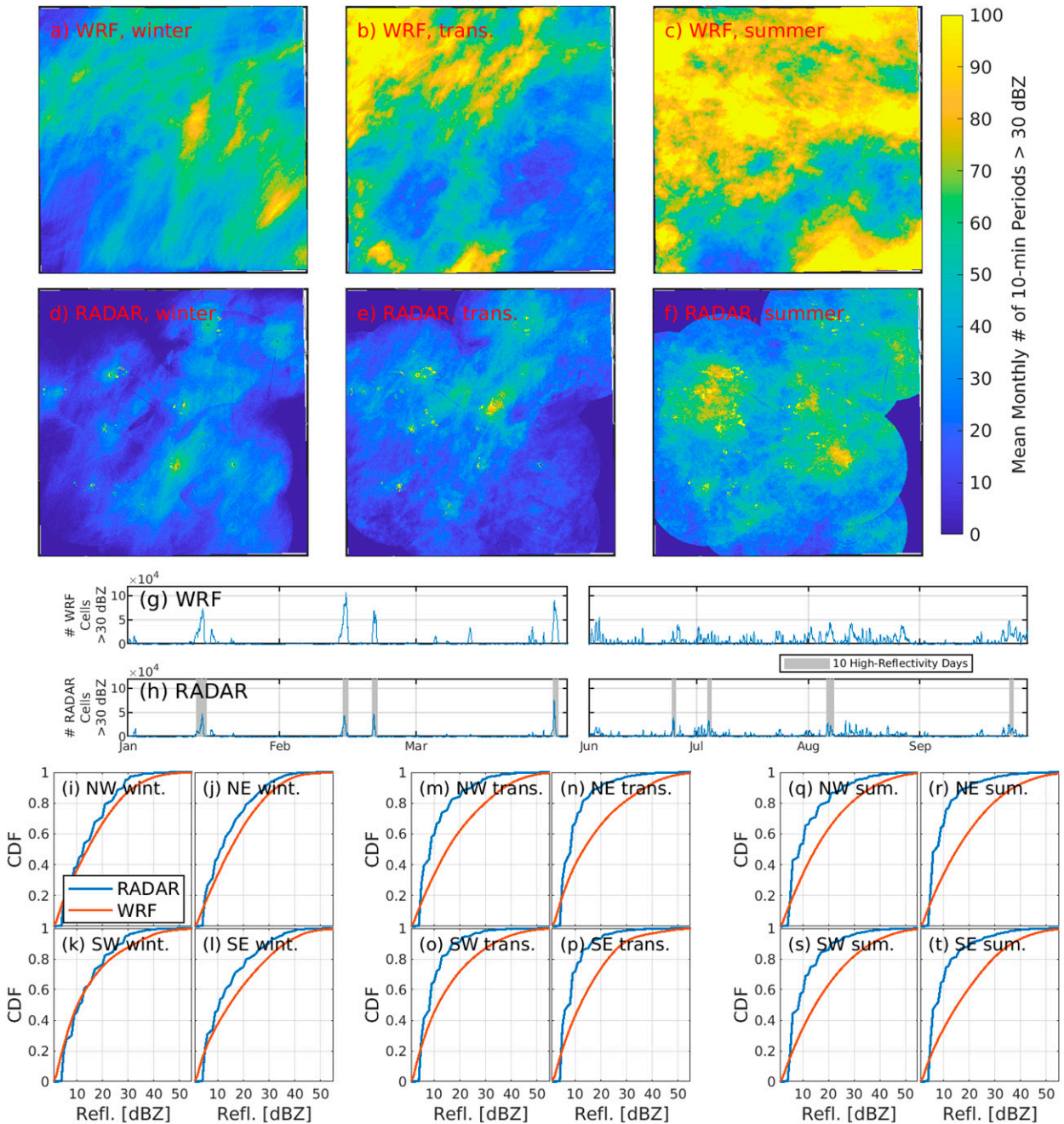
FIG. 5. Mean monthly number of 10-min periods with cREF > 30 dB$Z$ in each season from (a)–(c) WRF and (d)–(f) radar in each domain d03 grid cell, and time series of the number of d03 cells with cREF > 30 dB$Z$ from (g) WRF and (h) radar. The ten 24-h periods with highest total number of cells with cREF > 30 dB$Z$ are denoted by the gray background in (h). (i)–(t) Spatiotemporal CDFs of cREF from WRF and radar for each subdomain (see Fig. 2) in each season (wint = January and February, trans = March and September, sum = June, July, and August). These CDFs include all 10-min periods in all grid cells with cREF > 0. Data reported from radar are categorical, whereas those from WRF are continuous.

consistent with past research, for hydrometeor $D > 4$ mm, the number density of hailstones (when they occur) actually exceeds that of rain droplets. For a RR of 25–35 mm h$^{-1}$ and $D$ centered at 5.5 mm, the mean number density of hail is 2.26 m$^{-3}$ mm$^{-1}$ whereas for rain droplets it is 0.633 m$^{-3}$ mm$^{-1}$.

The wind speeds at 10 m AGL are discretized into five classes: 0–2, 2–5, 5–7, 7–15, and >15 m s$^{-1}$. Assuming a power-law relationship for wind speed dependence on height and a power-law exponent of 1/7, these classes correspond to the following conditions at the hub height. Class 1 (0–2 m s$^{-1}$) indicates wind

speeds below cut in, when the wind turbine rotor is unlikely to be turning. Class 2 indicates wind turbine blade rotation at a low and fairly constant speed. Class 3 covers the transition to the rated power and attainment of the highest (and constant) rotational speed (class 4). Class 5 defines wind speeds closest to or above cutout wind speeds. The joint probability distributions are built using a 30-km radius around each ASOS station in which the empirical estimates use the ASOS wind speed during each 10-min period and the spatial radar-derived RR within that same radius. The WRF output is sampled in these same areas.

## 3. Results

### a. *Spatiotemporal variability of cREF, precipitation, hail, and wind speeds metrics*

There are many sources of error in the WRF-derived equivalent radar reflectivity, and direct comparability to radar reflectivity is not expected (Koch et al. 2005). Nevertheless, the Spearman rank correlation between the time series of the spatial extent of modeled and radar-derived cREF > 30 dBZ is 0.79 (Figs. 5g,h). It is noteworthy that the spatial extent of grid cells with a high frequency of cREF > 30 dBZ in each season and the frequency with which large areas of domain d03 are simultaneously covered by cREF > 30 dBZ are substantially higher from WRF than in radar observations (Fig. 5). This overestimation is most marked in the summer months (cf. Figs. 5c,f) but is consistent through the entire simulation (Figs. 5g,h). The positive bias in the frequency with which high cREF is simulated is also manifest in all subregions of domain d03 (cf. Figs. 5a–f,m–t). The positive bias in the occurrence of cREF > 30 dBZ is consistent with previous research that has shown for a relatively wide array of model configurations WRF, when applied at convection-permitting scales and without data assimilation, tends to generate too wide of a region of moderate-to-high inferred cREF (Fan et al. 2017; Han et al. 2019; Tao et al. 2016). Despite the positive bias in the frequency of cREF > 30 dBZ, closer agreement is found for the spatial patterns of monthly mean total precipitation in each season and the time series of domainwide mean RR (Figs. 6a–h). The CDF plots for the subregions of domain d03 also exhibit a high degree for results from WRF and radar (Figs. 6i–t). The region of very high precipitation in the WRF output for the southeast of domain d03 during summer (cf. Figs. 6c,e) is due almost entirely to the northern displacement of Hurricane Harvey. Hurricane Harvey made landfall 25 August 2017 and between 25 and 30 August yielded rainfall totals along the coast of southern Texas in excess of 1000 mm and of over 750 mm in Houston, Texas (van Oldenborgh et al. 2017). The enhanced northern penetration of Hurricane Harvey in this simulation led to substantial (excess) precipitation in the southeast corner of domain d03.

The Spearman rank correlation coefficient *r* between the time series of 10-min domain d03 mean RR from WRF and radar is 0.67 (Figs. 6g,h). However, the simulation generates nonzero RR too frequently. Nonzero RR are reported in over

13% of the total sample of all grid cells and all 10-min time periods in WRF, but only 1.2% of radar estimates. If the sample of RR > 5 mm h$^{-1}$ is collected in space (i.e., each grid cell) and time (each 10-min period) from WRF for domain d03 and each of the four subregions of domain d03, much better agreement is found. The probability of occurrence of RR > 5 mm h$^{-1}$ in domain d03 is 0.42% in radar and 0.38% in WRF output. The ratio of the marginal probability of occurrence of RR > 5 mm h$^{-1}$ from WRF to that from radar in grid cells within the four subregions of domain d03 ranges from 0.8 to 1.5. Consistent with some past research (Kendon et al. 2021), there is also evidence that very heavy rainfall is simulated too frequently relative to radar (Fig. 6), particularly in the subregions NE and SE. This leads to a positive bias in mean monthly precipitation totals and higher domainwide mean RR during the 10 days with highest spatial coverage of cREF > 30 dBZ (Fig. 6), which is discussed in more detail below.

Hail is considerably less frequent in the winter than summer in both radar and WRF. For example, one or more hail cells are identified from radar data in 24 10-min periods in the NW subregion and 66 in the SE subregion during January and February. During the three summer months, radar-derived hail cells are identified in these subregions in 544 and 402 10-min periods. The overall probability of hail occurrence (i.e., nonzero hail accumulation) sampled in space and time in WRF simulations is 3–5 times that from radar even after scaling the radar observations by a factor of 45. This positive bias is largest in the NW subregion, where the WRF simulations exhibit nonzero hailfall in 1% of the spatiotemporal sample (i.e., all 10-min periods sampled in all grid cells), while the scaled radar data indicate a frequency ~0.2%. The bias in hail frequency is smallest in the SE subregion, where the probability from WRF is 0.33% and that from scaled radar is 0.11%.

Radar-derived hail properties including MESH have been previously evaluated (Cintineo et al. 2012; Murillo and Homeyer 2019; Ortega 2018). Specific to the current study region, one analysis of radar-derived hail occurrence and MESH found higher implied frequency of hail from radar in west Texas than is manifest in observer reports, which was largely ascribed to deficiencies in the observer-based analysis (Cintineo et al. 2012). A further study over the contiguous United States found a statistically significant, positive relationship between the daily number of severe hail observer-based reports and the area with radar-based nonzero MESH (Schlie et al. 2019). The synthesis of comparisons of the current WRF simulation with radar in terms of the overall probability of occurrence and MESH (Fig. 7) is that hail is present in the simulation too frequently but that during the transition and summer seasons the relative frequency of large hail (MESH > 25 mm) is higher in the radar observations (Figs. 7i–l). This is consistent with previous research that has indicated the Milbrandt–Yau microphysics scheme generated MESH estimates on the lower end of those from WRF microphysics schemes for a severe hail event in Colorado (Labriola et al. 2019a). Analyses of the joint probability of MESH from radar and WRF (Fig. 8) also indicate that in time periods and grid cells where both indicate the presence of hail, WRF
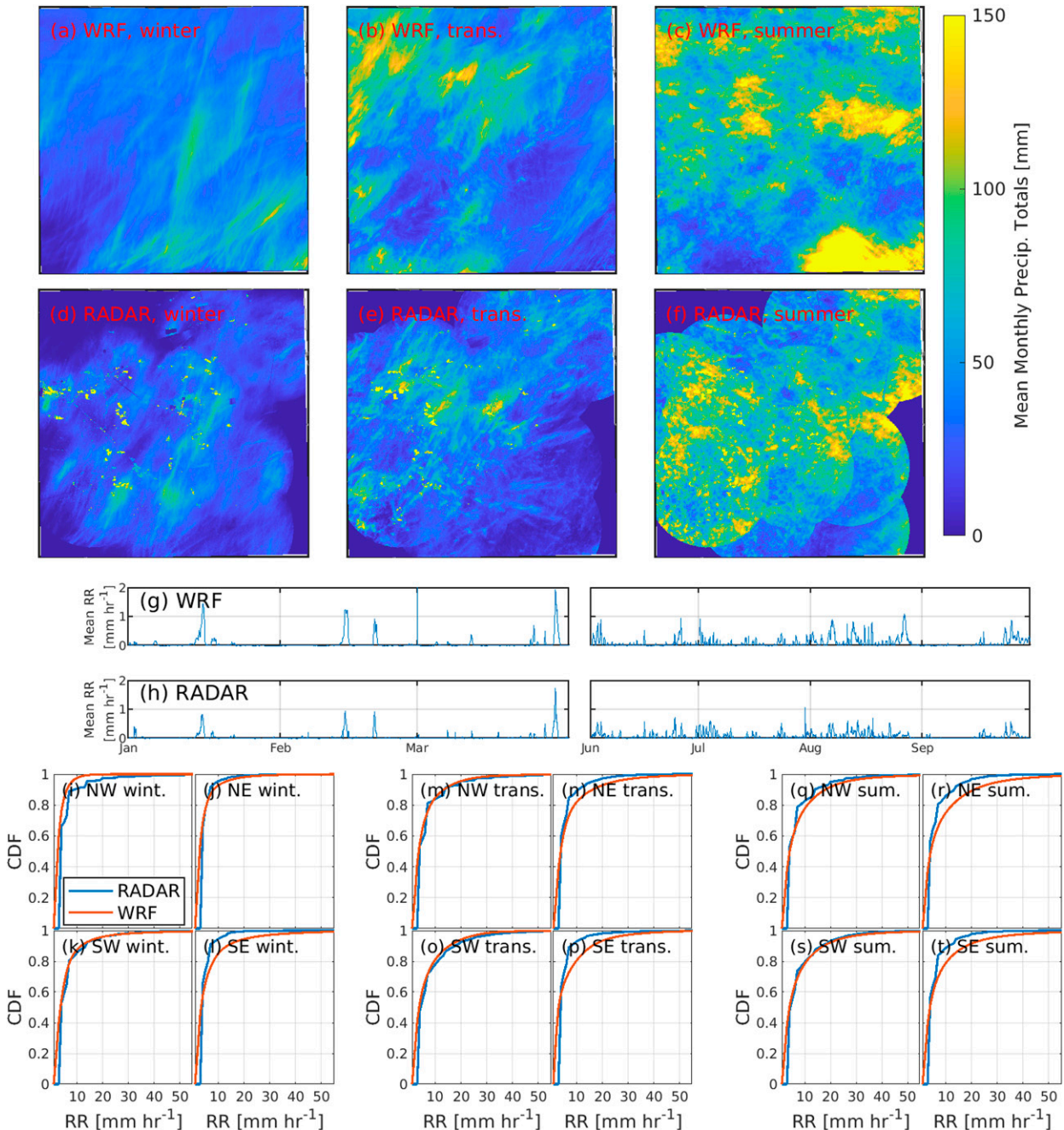
FIG. 6. Mean monthly total accumulated precipitation in each season from (a)–(c) WRF and (d)–(f) radar in each domain d03 grid cell, and time series of 10-min RRs from (g) WRF and (h) radar. (i)–(t) Spatiotemporal CDFs of RR from WRF and radar for each subregion (see Fig. 2) in each season (wint = January and February, trans = March and September, sum = June, July, and August). These CDFs include all 10-min periods in all grid cells with RR > 0. Data reported from radar are categorical, whereas those from WRF are continuous.

simulations overestimate the probability of occurrence of large MESH during January and February and underestimate the probability of occurrence of large MESH in the transition and summer months.

Odds ratios for categorical forecasts of hail occurrence, and cREF > 30 dB$Z$ or RR > 5 mm h$^{-1}$ over at least 5% of domain d03 indicate that the WRF simulation is highly skillful (Fig. 9). Ratio $\theta$ is greater than 1 for all seasons and all subregions of domain d03 and none of the 95% confidence intervals on $\ln(\theta)$ intersect zero. Forecast skill, measured by both the absolute magnitude of $\theta$ and the ratio of the width of the confidence interval on $\theta$ ($d\theta$) computed from Eq. (4) to the value of $\theta$ (i.e., $d\theta/\theta$) is consistently lowest (smallest value of $\theta$ and $d\theta/\theta$) in summer, although
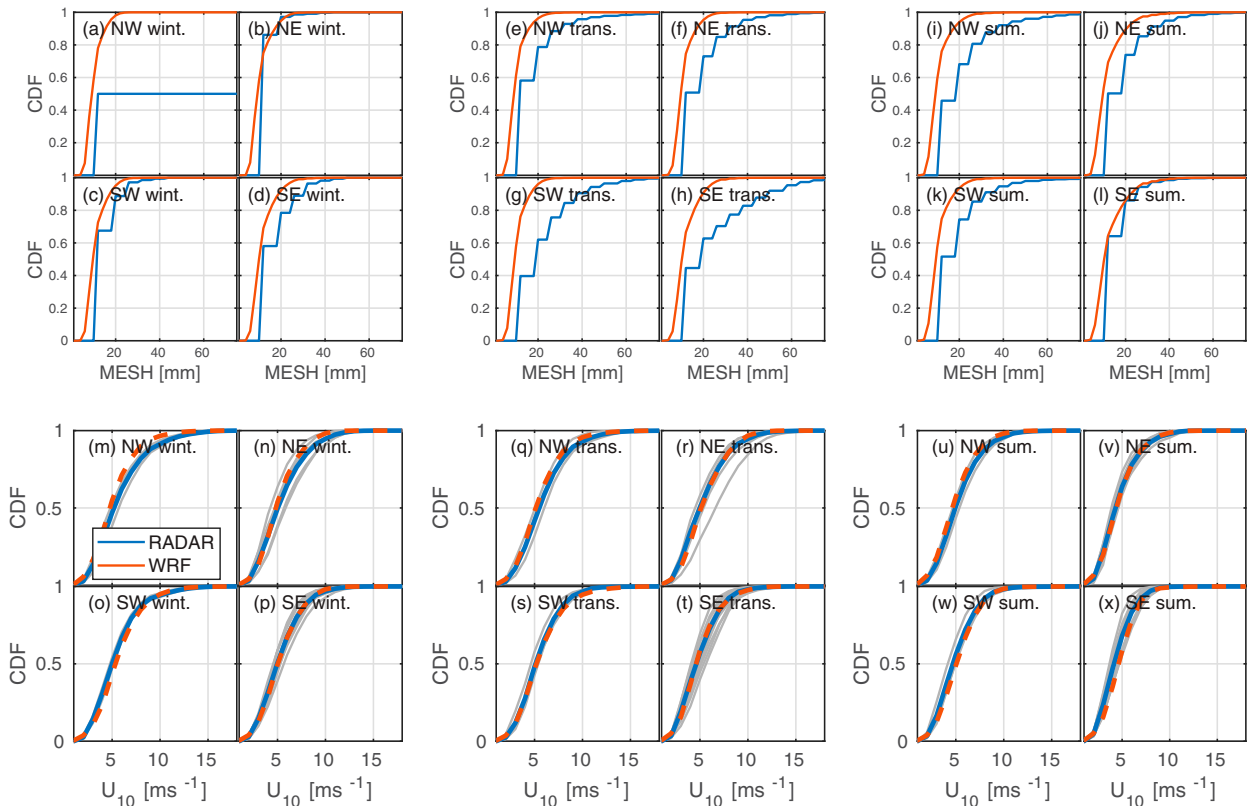
FIG. 7. (a)–(l) Spatiotemporal CDFs of MESH from WRF and radar. CDFs of MESH are for all 10-min periods when hail is present. MESH from radar is categorical. (m)–(x) Wind speeds at 10 m AGL $U_{10}$ from WRF and ASOS for each subregion in each season. Gray lines in (m)–(x) show individual ASOS stations (ASOS ind), and blue lines show the mean for all ASOS stations (ASOS all) in each subregion (Fig. 2). Red dotted lines show $U_{10}$ from WRF output in all ASOS-containing cells.

the number of 10-min periods that meet the criteria of an event is higher in summer. For example, in subregion NW the total number of radar-detected hail events is 544 [$a$ (hits) = 428 + $c$ (misses) = 116] as compared with 24 in winter and 153 in the transition months. Both hail frequency

and model skill in forecasting hail occurrence also exhibit spatial variability. In the NW subregion the radar observations indicate evidence for hail in radar data on 746 of all 10-min periods, while WRF indicates nonzero hail accumulation on 1709 10-min periods. In the SE, 536 and 956
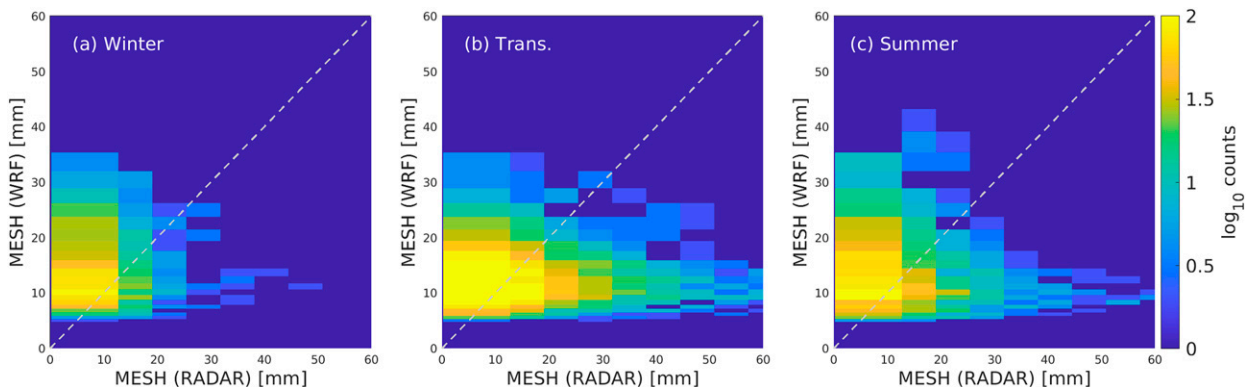


FIG. 8. Joint distributions of MESH from WRF and radar during all 10-min periods and locations (grid cells) when hail is present in both datasets. The white dotted line $y = x$ is included to facilitate comparison. Note that the frequency of occurrence of the joint classes of MESH from WRF and radar is shown on a logarithmic scale, and the scale is truncated at 100 to aid legibility. The discretization used for the radar and WRF MESH estimates reflects the unique values found in each dataset.
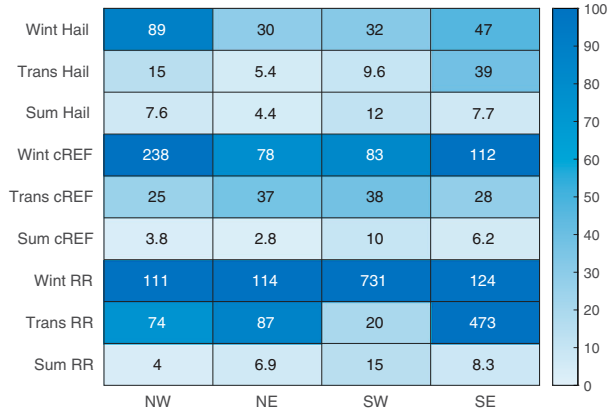
FIG. 9. Odds ratios $\theta$ for categorical forecasts from WRF vs radar for the presence of hail and cREF > 30 dBZ and RR > 5 mm h$^{-1}$ over more than 5% of the area of each subregion (see Fig. 2b) for each season. The color scale is capped at 100 to make gradations between lower $\theta$ more visible.

10-min periods fulfill these conditions. Accordingly, $\theta$ is higher for the SE than NW for the transition and summer months.

WRF-derived near-surface wind speeds exhibit a strong dependence on model configuration (particularly PBL and surface schemes; Hahmann et al. 2020) but generally exhibit fidelity in areas of flat terrain (Hahmann et al. 2020; Hawbecker et al. 2017; Letson et al. 2020b; Pryor and Hahmann 2019). Comparisons of wind speeds from WRF and ASOS are subject to a number of important caveats. Sustained 2-min mean wind speeds as reported by ASOS sonic anemometers are rounded up to the nearest knot and values below 3 kt (1.543 m s$^{-1}$) are recorded as "calm" or 0 m s$^{-1}$. Conversely, the WRF values are for the model time step and are spatial averages. With these caveats, the current simulations

reproduce the wind climate seasonality. Consistent with ASOS wind speed observations and the observed seasonal pattern of wind turbine power production (Pryor et al. 2020), wind speeds from WRF are lowest in the summer months. Spearman $r$ of 10-m wind speeds from ASOS and WRF (sampled at ASOS stations) are highest in the winter and transition season months ($r > 0.5$ in all seasons) and the ratios of the temporal standard deviations are close to 1. The simulations also reproduce key aspects of the $U_{10}$ probability distribution from ASOS stations in the different subregions of domain d03 (Figs. 7m–x).

### b. Days with large spatial coverage of high cREF

The 10 days with highest spatial coverage of cREF > 30 dBZ (Figs. 5g,h) exhibit high precipitation accumulation from both WRF and radar (Figs. 6g,h). Evaluation relative to point observations is plagued by a double penalty (for displacement in time and/or space; Prein et al. 2013). Thus, here we focus principally on domainwide precipitation over the entire day. Consistent with the other analyses presented above, the 24-h precipitation accumulation from WRF exceeds those from radar on 8 of the 10 days (Fig. 10). The ratios of mean d03 precipitation accumulation from radar to WRF range from 0.26 (4 July) and 0.41 (24 June) to 2.35 (14 February) and 2.76 (16 January).

WRF underestimates both the mean 24-h total precipitation as sampled for grid cells containing ASOS stations and spatial variability (Fig. 10a). These observations also emphasize that these 10 days are associated with very high localized precipitation of up to 100 mm in a 24-h period at some ASOS stations. WRF output exhibits reasonable accord with the total domain-d03 mean 24-h precipitation from radar, IMERG, and Stage IV for these dates. Applying a threshold of 0.25 mm as "measurable" daily accumulated
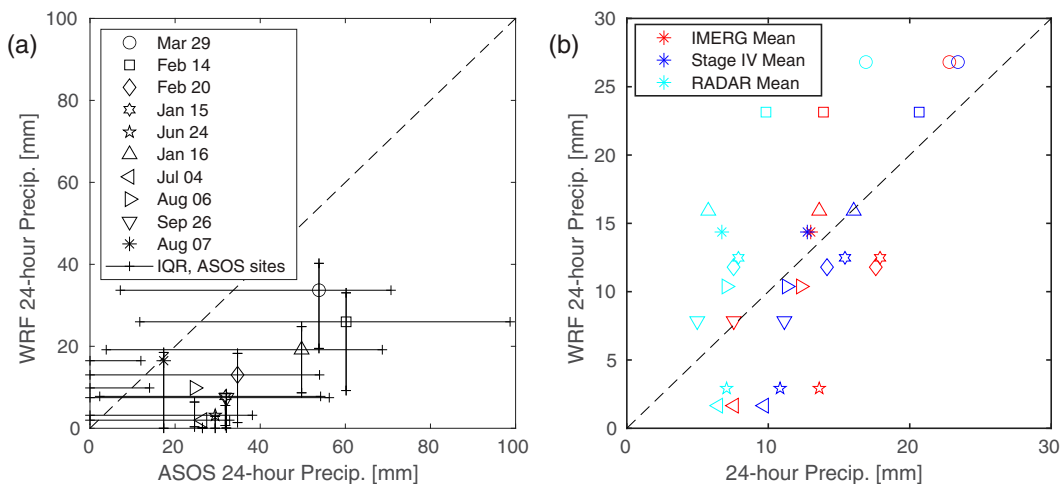


FIG. 10. (a) Scatterplot of 24-h total WRF and ASOS precipitation (mean total across all ASOS station-containing cells of snow, rain, hail, and graupel) on the 10 dates with highest spatial extent of cREF > 30 dBZ (Fig. 5; see legend). The whiskers show the interquartile range (IQR) among all ASOS stations and ASOS station–containing WRF cells. (b) Mean 24-h total precipitation over all of domain d03 from IMERG, Stage IV, and radar vs WRF precipitation on those same dates.

precipitation (Arguez et al. 2012), data from radar indicate the spatial coverage of domain d03 with nonzero precipitation on these 10 dates (listed as in Fig. 10b) is 77%, 60%, 50%, 59% (15 January), 40%, 60%, 53% (4 July), 38%, 46%, and 43%. Comparable values from the WRF output are 84%, 95%, 70%, 90% (15 January), 38%, 78%, 23% (4 July), 73%, 70%, and 61% of domain d03. The Spearman $r$ between WRF and radar of domainwide precipitation received on these dates is 0.53. Substantial precipitation is also indicated on these dates by the other observational datasets (Fig. 10). For example, the spatial coverage of daily accumulated precipitation above 0.25 mm within domain d03 from IMERG ranges from 91% (29 March) to 51% (24 June), and the domainwide mean 24-h total precipitation again from IMERG ranges from 7.6 (26 September) to 22.8 mm (29 March).

The WRF output exhibits closer accord with IMERG in terms of total precipitation accumulation than with Stage IV. The slopes and intercept values of linear fits ($y = mx + c$, where $x$ is the observation and $y$ is WRF) to the daily mean total precipitation accumulation shown in Fig. 10b yield values of $m = 1.17$ and $c = -3.2$ (IMERG), $m = 1.74$ and $c = -1.22$ (radar), and $m = 1.68$ and $c = -11.66$ (Stage IV).

Analyses of model output for 3 of the 10 dates (29 March, 24 June, and 16 January) with highest spatial coverage of cREF $> 30$ dB$Z$ illustrate the following: first, in both radar and WRF more spatially extensive areas of high reflectivity and precipitation are present in events during the transition season and winter (Fig. 11). Second, consistent with past research, these case studies indicate WRF simulates a wider swath of high cREF ($>40$ dB$Z$ or $>30$ dB$Z$) and a narrower stratiform area (Fan et al. 2017; Fig. 11). Nevertheless, the spatial extent of nonzero precipitation at the time of maximum spatial extent of cREF $> 30$ dB$Z$ is relatively well reproduced. Third, transects through a line of organized convection as indicated by radar and simulated with WRF exhibit important similarities in terms of the vertical extent of high reflectivity for 29 March and 24 June, but the transect for 16 January exhibits a greater depth of high reflectivity than is evident in the radar data, and the simulated vertical velocities from WRF within this region are much higher than in the other two cases (Fig. 11). These transects also illustrate the presence in the WRF Model output of horizontally limited intense updraft cores associated with high inferred reflectivity in the upper model levels. Last, hail production in WRF is frequently associated with information in the radar HHC that indicates either the presence of hail or either graupel and/or snow (Fig. 12). Thus, while hailfall at the ground appears to be oversimulated, radar data are consistent with the presence of solid hydrometeors in the clouds.

The excess presence of solid hydrometeors (hail and graupel; Figs. 12c,f,i,l) and the excess duration of deep convective (and nonzero precipitation; cf. Figs. 12c,f) in the current simulation of 16 January may also be linked to the very high modeled vertical velocities (Fig. 11o), excess vertical cloud development (as manifest in the vertical extent of high radar reflectivity; cf. Figs. 11i,l), and possible feedbacks from the resulting cold pool (see discussion in section 1). Simulations of a squall line that occurred on 20 May 2011 during the MC3E experiment found evidence for excess vertical extent of REF $> 30$ dB$Z$ and positive bias in vertical velocities in simulations with all of the eight microphysics schemes tested (Fan et al. 2017). Of particular relevance to the current work, the bias in updraft velocities was particularly marked in simulations of the Milbrandt–Yau microphysics scheme, although the vertical extent of REF $> 30$ dB$Z$ was not particularly marked in the simulation with the Milbrandt–Yau microphysics scheme (Fan et al. 2017).

### c. Joint probabilities of wind speeds, rainfall rates, and hail occurrence

The fidelity assessment summarized above implies the WRF simulation exhibits skill in reproducing the marginal probabilities and spatial variability of wind speeds, RR and hail, and aspects of individual convective events. For applications to wind turbine blade LEE, these are necessary prerequisites for damage assessment but insufficient to ensure accuracy of such assessments. The demand for fidelity in both wind speed and precipitation type (hydrometeor)/RR and specifically the co-occurrence of high RR and wind speed provides an extremely stringent challenge for atmospheric models. Performance in this context is described below.

Datasets collected at the DOE ARM facility allow a pointwise evaluation of WRF, but for some of the simulation period the disdrometer and/or wind profiler were not operational (e.g., January and February). This low data volume and bias toward sampling the warm-season months, plus the challenges in comparing point observations of wind speed and RR, limit detailed interpretation. Nevertheless, the WRF simulation appears to underestimate the relative frequency of very high RR at this site. At this location, as in most of domain d03, WRF rains too often but at relatively low RR; RR $> 45$ mm h$^{-1}$ are observed by the disdrometers on $\sim$0.5% of all periods with RR $> 0$ mm h$^{-1}$ but only 0.04% of WRF output from that grid cell when precipitation is simulated (Fig. 13). The compensating bias in precipitation frequency means the absolute frequency of RR $> 45$ mm h$^{-1}$ is within a factor of 2 of the observations. There is a positive bias in simulated wind speeds at/near wind turbine hub heights during periods of precipitation (Fig. 13). Wind speeds at hub height exceed 10 m s$^{-1}$ in lidar observations in $<$6% of periods with RR $> 0$, while this threshold is exceeded in $>$13% of WRF output during periods with precipitation. Such biases will offset each other in terms of inferred total kinetic energy transferred to rotating wind turbine blades. The negative bias in high RR will lead to a negative bias in the number, size, and $v_t$ from the most erosive hydrometeors, but the positive bias in wind speed at wind turbine hub height means there will be a positive bias in blade rotational speed and thus the closing velocity.

For the domainwide and subregional analyses, the relative frequency of occurrence of hail in each $U_{10}$ class is
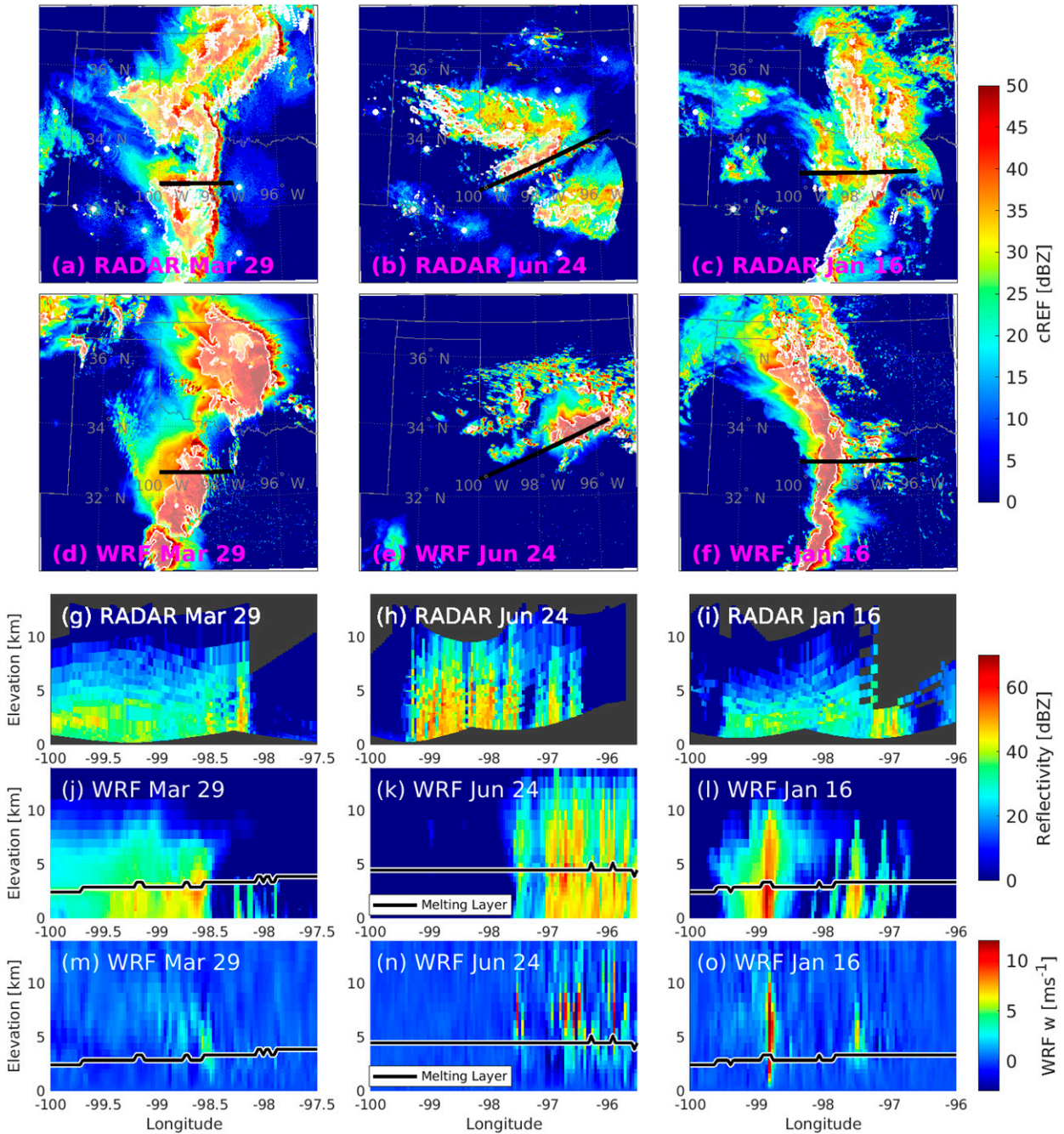
FIG. 11. The cREF from (a)–(c) radar and (d)–(f) WRF during example 10-min periods on 29 Mar, 24 Jun, and 16 Jan. Also shown by the white outlines and shading are areas where precipitation is occurring. Vertical profiles of reflectivity from (g)–(i) radar (from the elevation scans at 0.5°, 0.9°, 1.3°, 1.8°, 2.4°, and 3.1°) and (j)–(l) WRF, along with (m)–(o) vertical wind speed $w$ and height of the melting layer from WRF, along the transects shown by the black lines in (a)–(f).

well represented in the WRF simulation, while the relative frequency of liquid precipitation (of any intensity) for $U_{10} > 7$ m s$^{-1}$ exhibits a positive bias relative to radar-based observations within 30 km of each ASOS station (Fig. 14). This subsampling yields the finding that 2.8% of periods when precipitation is observed are associated with RR $> 25$ mm h$^{-1}$ and wind speeds at which the wind turbine blades would be rotating, while the comparable value from WRF is 3.8%. Considering wind speeds where the wind turbine blades would likely be at their maximum rotational speed $U_{10}$ (7–15 m s$^{-1}$), RR $> 25$ mm h$^{-1}$ are almost 2 times as frequent in the WRF output. This comparison,
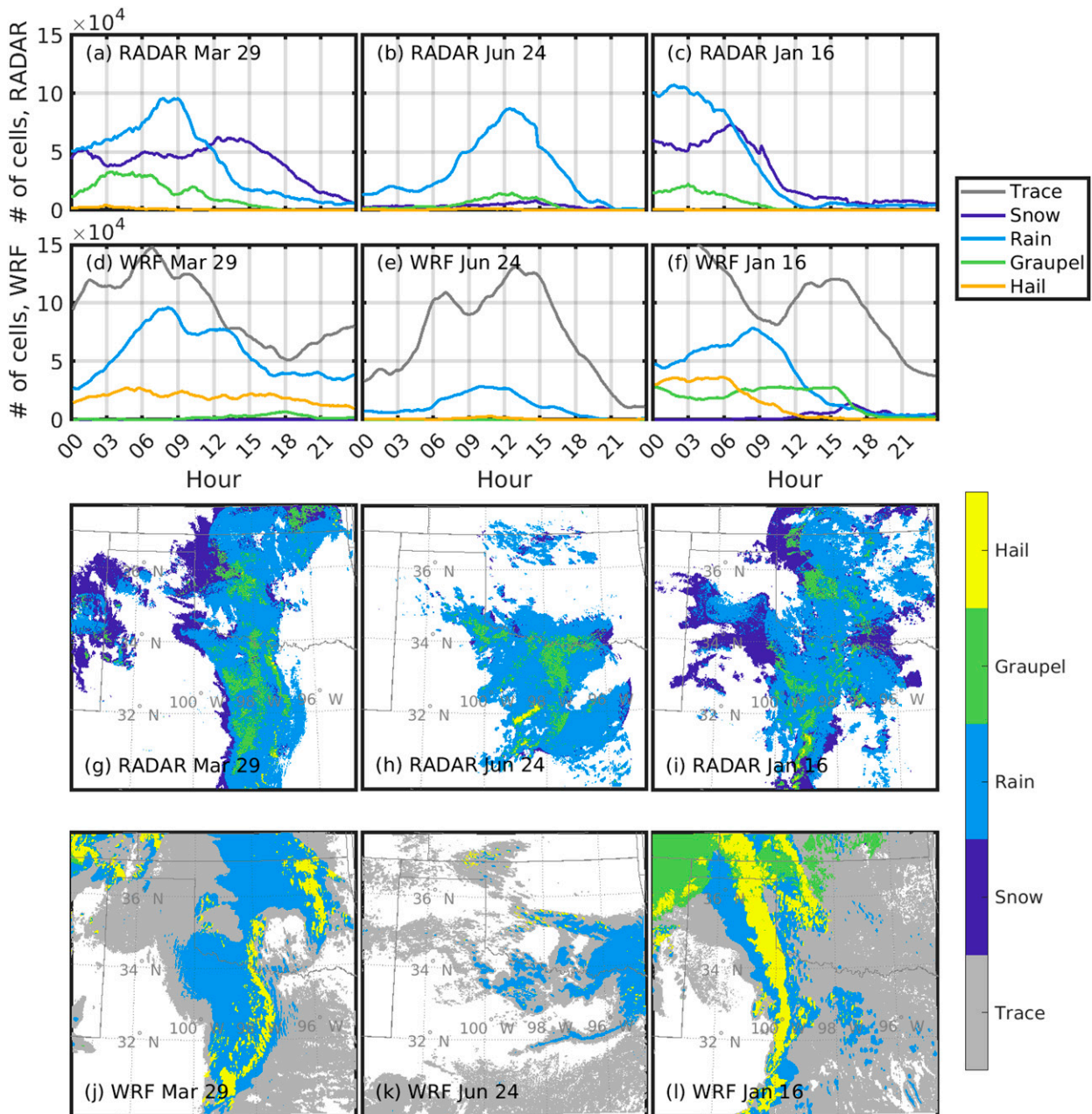
FIG. 12. Hydrometeor classes during 29 Mar, 24 Jun, and 16 Jan: time series of the number of domain d03 cells with each precipitation type from (a)–(c) radar and (d)–(f) WRF, and maps for the time of most widespread precipitation from radar, showing output from (g)–(i) radar and (j)–(l) WRF. Radar hydrometeor classes are consolidated from 10 to 4 to match the WRF hydrometeor classes. "Trace" precipitation from WRF is shown for any cell with RR $< 0.15$ mm h$^{-1}$.

in contrast to pointwise analyses at the ARM facility, implies kinetic energy transfer to the blades from liquid hydrometeor impacts is likely to be overestimated if calculated from the WRF simulation output. Both the WRF simulation and the radar estimate of hail occurrence also indicates that a substantial fraction of the time when hail is indicated also occurs during periods when the wind turbine would be rotating (Fig. 14), and further, nearly 30% of all hail events

are associated with wind speeds at which the wind turbine blades are rotating at, or close to, their maximum speed (i.e., $U_{10} > 7$ m s$^{-1}$). Hail impacts are thought to be associated with higher kinetic energy transfer and material stresses due to the hardness and relatively large diameter of the hydrometeors (Keegan et al. 2013).

When the four subregions of domain d03 are considered, the joint probabilities of $U_{10}$ and RR and the occurrence
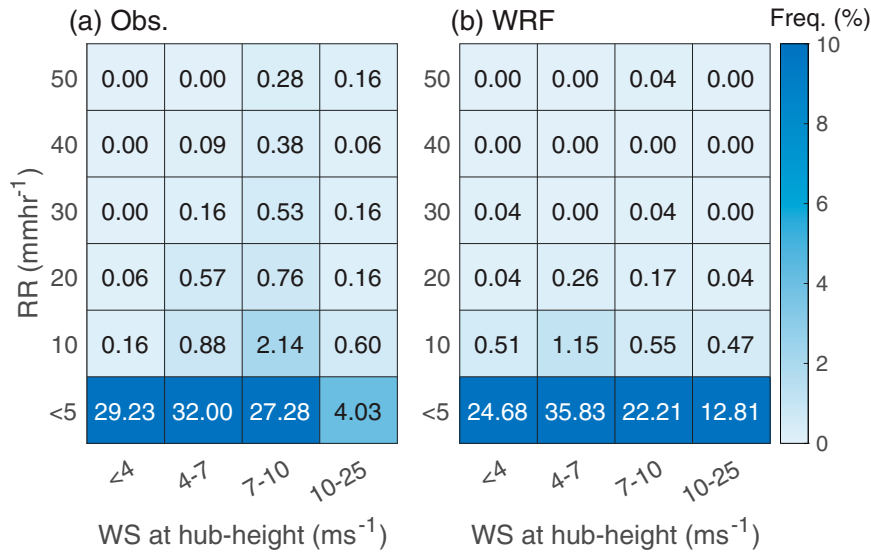
FIG. 13. Joint probabilities of wind speed at hub height (label WS) and RR for all periods when both WRF output and observations are available, and RR > 0 mm h$^{-1}$ from (a) DOE ARM observations (Obs) and (b) WRF. The color bar is truncated to highlight variations in color for lower frequency but high-impact events. Note that the classes of rainfall rate are not equal. The class denoted by <5 shows RR above 0 and less than 5 mm h$^{-1}$. All other classes have a bin width of 10 mm h$^{-1}$ and are centered on the value shown.

of hail in different wind speed classes are relatively well reproduced. However, the WRF simulation output fails to reproduce the clear west–east gradient in the co-occurrence of high $U_{10}$ and high RR evident in observations from the four subdomains (Fig. 15). Closer accord is found for NW and SW subdomains, but in the two eastern subregions, the occurrence of all RR in the $U_{10}$ class 7–15 m s$^{-1}$ is substantially overestimated.
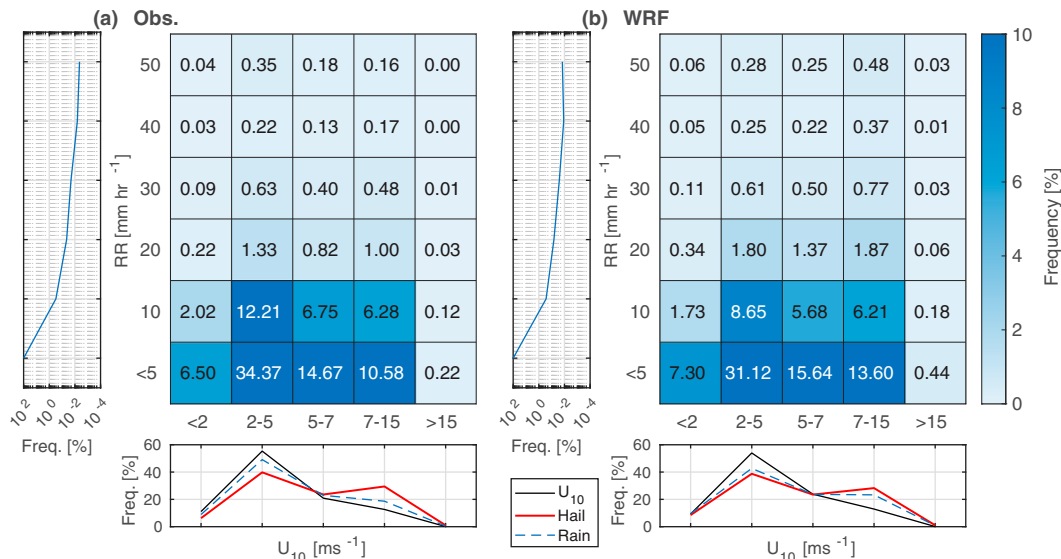


FIG. 14. Joint probabilities of 10-m wind speed $U_{10}$ and RR from (a) observations and (b) WRF in domain d03 for all periods with RR > 0 mm h$^{-1}$. The color bar is limited to frequencies of 0%–10% to help to highlight variations in color for events with lower frequency but high impact. Note that the classes of rainfall rate are not equal. The class denoted by <5 shows RR above 0 and less than 5 mm h$^{-1}$. All other classes have a bin width of 10 mm h$^{-1}$ and are centered on the value shown. The marginal probabilities of RR are shown in each left-hand subpanel (these probabilities include events with RR = 0 mm h$^{-1}$). The lower panels show the marginal probability distributions of $U_{10}$ in each class (black) along with the fraction of total rain and hail events associated with each $U_{10}$ class, shown in blue and red, respectively.
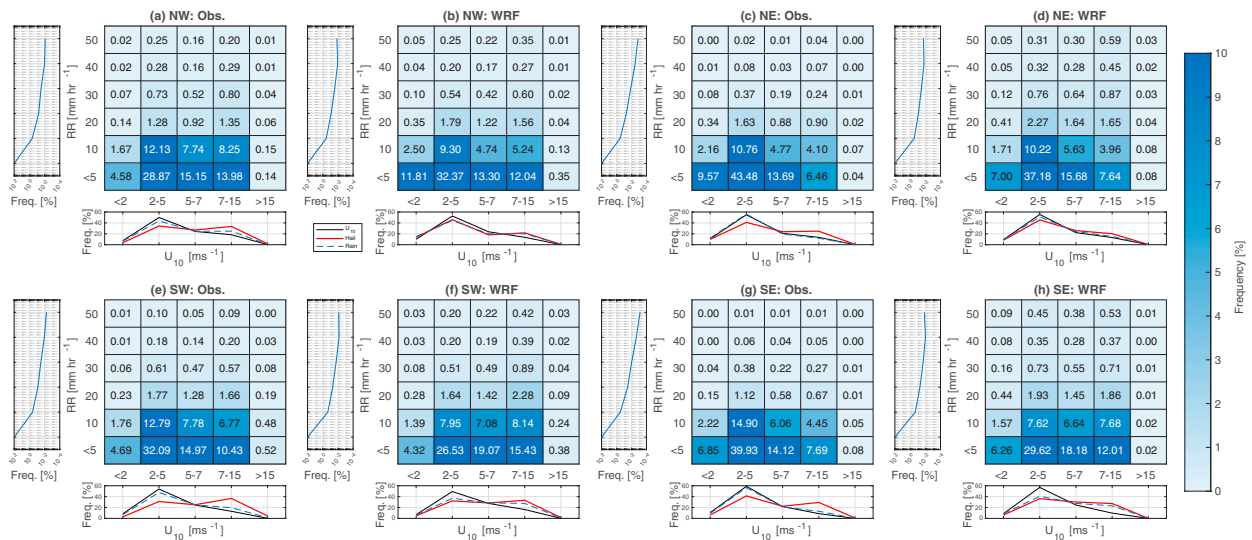
FIG. 15. As in Fig. 14, but from (a),(c),(e),(g) observations and (b),(d),(f),(h) WRF for each of the subregions of domain d03.

## 4. Summary and concluding remarks

Accurate simulation of hydroclimate conditions even in convection-permitting regional climate simulations is extremely challenging. Further, objective assessment of such simulations, particularly for hail occurrence and size, is not aided by the relative paucity of direct observations and the assumptions implicit in deriving hail estimates from radar. Nevertheless, the WRF simulation presented herein is shown to exhibit fidelity in important aspects of the hydroclimate. Returning to our original objectives, we show that the marginal probabilities and spatial patterns of RR and wind speeds exhibit close accord with radar and gridded datasets and in situ observations. Further, the odds ratios of hail occurrence and high RR are indicative of simulation skill at the event level, even in the absence of data assimilation or nudging. Consistent with our a priori expectations, there is clear positive bias in the spatial extent of high composite reflectivity and model fidelity for hail occurrence, and size is lowest in the summer months. Case study analyses of high spatial extent of cREF and precipitation equally indicate credibility with respect to the vertical structure of deep convection and the presence of solid-phase hydrometeors in clouds. They also provide preliminary evidence that the excess production of hail in the simulation is due to a combination of deep convection that is too intense during the cold season and possible misallocation of hydrometeors between the six classes treated by the microphysics scheme.

Application of WRF to generate a priori estimates of wind turbine blade LEE or to enable an erosion-safe operational mode represents both a critical research need as society makes a transition to a lower-carbon energy supply and an opportunity to consider more holistically model skill. Despite the positive aspects of the simulation fidelity assessment described above, these are not sufficient to ensure skill in the joint probabilities of hail occurrence or high RR with wind speed, particularly in comparisons for specific subregions of the simulation domain and in pointwise comparison at the DOE SGP ARM site. For example, while this 7-month WRF simulation captures some of the spatial variability in these joint probabilities, this simulation underestimates the west–east gradient in the co-occurrence of high wind speeds, when wind turbine tip speeds are maximized and RR > 25 mm h$^{-1}$.

Because of the high computational burden of simulations such as those presented herein, only selected months from a representative year in terms of the radar-derived hail climate are considered. Quantification of the degree to which model fidelity assessments presented herein are generalizable requires simulation of multiple complete years to allow sampling of a wide range of meteorological conditions and environmental contexts for deep convection. Future work should also evaluate whether different model formulations and advanced/improved microphysics schemes can achieve higher skill in terms of the joint probabilities of intense precipitation and high wind speeds. Development of such a large model ensemble should also include alternative sources of the LBC (e.g., ERA5; Hersbach et al. 2020). Improved assessment of modeling capability and relative performance of different ensemble members is key to the development of recommended best practice, prioritizing areas for model improvement, and would greatly benefit the growing renewable energy community in the Southern Great Plains and beyond.

gratitude to the three anonymous reviewers for their helpful comments and suggestions and to Brian Naess for providing access to the NLDN data.

# REFERENCES

Adams-Selin, R. D., and C. L. Ziegler, 2016: Forecasting hail using a one-dimensional hail growth model within WRF. *Mon. Wea. Rev.*, **144**, 4919–4939, https://doi.org/10.1175/MWR-D-16-0027.1.

——, A. J. Clark, C. J. Melick, S. R. Dembek, I. L. Jirak, and C. L. Ziegler, 2019: Evolution of WRF-HAILCAST during the 2014–16 NOAA/hazardous weather testbed spring forecasting experiments. *Wea. Forecasting*, **34**, 61–79, https://doi.org/10.1175/WAF-D-18-0024.1.

Agresti, A., 2018: *An Introduction to Categorical Data Analysis.* 3rd ed. John Wiley and Sons, 400 pp.

American Clean Power, 2021: Clean Power Quarterly 2020 Q4. ACP Rep., 27 pp., https://cleanpower.org/resources/american-clean-power-market-report-q4-2020/.

American Meteorological Society, 2015: "Graupel." Glossary of Meteorology, https://glossary.ametsoc.org/wiki/Graupel.

Arguez, A., I. Durre, S. Applequist, R. S. Vose, M. F. Squires, X. Yin, R. R. Heim Jr., and T. W. Owen, 2012: NOAA's 1981–2010 U.S. climate normals: An overview. *Bull. Amer. Meteor. Soc.*, **93**, 1687–1697, https://doi.org/10.1175/BAMS-D-11-00197.1.

Bang, S. D., and D. J. Cecil, 2019: Constructing a multifrequency passive microwave hail retrieval and climatology in the GPM domain. *J. Appl. Meteor. Climatol.*, **58**, 1889–1904, https://doi.org/10.1175/JAMC-D-19-0042.1.

Bartholomew, M. J., 2020: Laser disdrometer instrument handbook. U.S. Department of Energy Office of Scientific and Technical Information Tech. Rep. DOE/SC-ARM-TR-137, 22 pp., https://doi.org/10.2172/1226796.

Beck, H. E., and Coauthors, 2019: Daily evaluation of 26 precipitation datasets using Stage-IV gauge-radar data for the

CONUS. *Hydrol. Earth Syst. Sci.*, **23**, 207–224, https://doi.org/10.5194/hess-23-207-2019.

Brook, J. P., A. Protat, J. Soderholm, J. T. Carlin, H. McGowan, and R. A. Warren, 2021: HailTrack—Improving radar-based hailfall estimates by modeling hail trajectories. *J. Appl. Meteor. Climatol.*, **60**, 237–254, https://doi.org/10.1175/JAMC-D-20-0087.1.

Brown, T. M., W. H. Pogorzelski, and I. M. Giammanco, 2015: Evaluating hail damage using property insurance claims data. *Wea. Climate Soc.*, **7**, 197–210, https://doi.org/10.1175/WCAS-D-15-0011.1.

Candela Garolera, A., S. F. Madsen, M. Nissim, J. D. Myers, and J. Holboell, 2016: Lightning damage to wind turbine blades from wind farms in the US. *IEEE Trans. Power Delivery*, **31**, 1043–1049, https://doi.org/10.1109/TPWRD.2014.2370682.

Cintineo, J. L., T. M. Smith, V. Lakshmanan, H. E. Brooks, and K. L. Ortega, 2012: An objective high-resolution hail climatology of the contiguous United States. *Wea. Forecasting*, **27**, 1235–1248, https://doi.org/10.1175/WAF-D-11-00151.1.

Crum, T. D., R. E. Saffle, and J. W. Wilson, 1998: An update on the NEXRAD program and future WSR-88D support to operations. *Wea. Forecasting*, **13**, 253–262, https://doi.org/10.1175/1520-0434(1998)013<0253:AUOTNP>2.0.CO;2.

Dai, Y., I. N. Williams, and S. Qiu, 2021: Simulating the effects of surface energy partitioning on convective organization: Case study and observations in the US Southern Great Plains. *J. Geophys. Res. Atmos.*, **126**, e2020JD033821, https://doi.org/10.1029/2020JD033821.

Davenport, C. E., 2021: Environmental evolution of long-lived supercell thunderstorms in the Great Plains. *Wea. Forecasting*, **36**, 2187–2209, https://doi.org/10.1175/WAF-D-21-0042.1.

Dee, D. P., and Coauthors, 2011: The ERA-Interim reanalysis: Configuration and performance of the data assimilation system. *Quart. J. Roy. Meteor. Soc.*, **137**, 553–597, https://doi.org/10.1002/qj.828.

De Moura, C. A., and C. S. Kubrusly, Eds., 2013: *The Courant–Friedrichs–Lewy (CFL) Condition: 80 Years after Its Discovery.* Springer, 237 pp., https://doi.org/10.1007/978-0-8176-8394-8.

Dessens, J., 1986: Hail in southwestern France. I: Hailfall characteristics and hailstorm environment. *J. Appl. Meteor. Climatol.*, **25**, 35–47, https://doi.org/10.1175/1520-0450(1986)025<0035:HISFIH>2.0.CO;2.

Du, Y., S. Zhou, X. Jing, Y. Peng, H. Wu, and N. Kwok, 2020: Damage detection techniques for wind turbine blades: A review. *Mech. Syst. Signal Process.*, **141**, 106445, https://doi.org/10.1016/j.ymssp.2019.106445.

Dudhia, J., 1989: Numerical study of convection observed during the Winter Monsoon Experiment using a mesoscale two-dimensional model. *J. Atmos. Sci.*, **46**, 3077–3107, https://doi.org/10.1175/1520-0469(1989)046<3077:NSOCOD>2.0.CO;2.

Edwards, R., and R. L. Thompson, 1998: Nationwide comparisons of hail size with WSR-88D vertically integrated liquid water and derived thermodynamic sounding data. *Wea. Forecasting*, **13**, 277–285, https://doi.org/10.1175/1520-0434(1998)013<0277:NCOHSW>2.0.CO;2.

Fan, J., and Coauthors, 2017: Cloud-resolving model intercomparison of an MC3E squall line case: Part I—Convective updrafts. *J. Geophys. Res. Atmos.*, **122**, 9351–9378, https://doi.org/10.1002/2017JD026622.

Feng, Z., L. R. Leung, R. A. Houze Jr., S. Hagos, J. Hardin, Q. Yang, B. Han, and J. Fan, 2018: Structure and evolution of mesoscale convective systems: Sensitivity to cloud microphysics in convection-permitting simulations over the United

States. *J. Adv. Model. Earth Syst.*, **10**, 1470–1494, https://doi.org/10.1029/2018MS001305.

——, R. A. Houze Jr., L. R. Leung, F. Song, J. C. Hardin, J. Wang, W. I. Gustafson Jr., and C. R. Homeyer, 2019: Spatio-temporal characteristics and large-scale environments of mesoscale convective systems east of the Rocky Mountains. *J. Climate*, **32**, 7303–7328, https://doi.org/10.1175/JCLI-D-19-0137.1.

——, and Coauthors, 2021: A global high-resolution mesoscale convective system database using satellite-derived cloud tops, surface precipitation, and tracking. *J. Geophys. Res. Atmos.*, **126**, e2020JD034202, https://doi.org/10.1029/2020JD034202.

Fritsch, J. M., R. J. Kane, and C. R. Chelius, 1986: The contribution of mesoscale convective weather systems to the warm-season precipitation in the United States. *J. Climate Appl. Meteor.*, **25**, 1333–1345, https://doi.org/10.1175/1520-0450(1986)025<1333:TCOMCW>2.0.CO;2.

Froese, M., 2018: Wind-farm owners can now detect leading-edge erosion from data alone. Windpower Engineering and Development, accessed 14 August 2018, https://www.windpowerengineering.com/wind-farm-owners-can-now-detect-leading-edge-erosion-from-data-alone/.

Fulton, R. A., J. P. Breidenbach, D.-J. Seo, D. A. Miller, and T. O'Bannon, 1998: The WSR-88D rainfall algorithm. *Wea. Forecasting*, **13**, 377–395, https://doi.org/10.1175/1520-0434(1998)013<0377:TWRA>2.0.CO;2.

Gaertner, E., and Coauthors, 2020: IEA Wind TCP Task 37: Definition of the IEA 15-megawatt offshore reference wind turbine. NREL Tech. Rep. NREL/TP-5000-75698, 54 pp., https://www.osti.gov/biblio/1603478.

Gagne, D. J., II, A. McGovern, S. E. Haupt, R. A. Sobash, J. K. Williams, and M. Xue, 2017: Storm-based probabilistic hail forecasting with machine learning applied to convection-allowing ensembles. *Wea. Forecasting*, **32**, 1819–1840, https://doi.org/10.1175/WAF-D-17-0010.1.

Goines, D. C., and A. D. Kennedy, 2018: Precipitation from a multiyear database of convection-allowing WRF simulations. *J. Geophys. Res. Atmos.*, **123**, 2424–2453, https://doi.org/10.1002/2016JD026068.

Haerter, J. O., S. J. Böing, O. Henneberg, and S. B. Nissen, 2019: Circling in on convective organization. *Geophys. Res. Lett.*, **46**, 7024–7034, https://doi.org/10.1029/2019GL082092.

Hahmann, A. N., and Coauthors, 2020: The making of the New European Wind Atlas—Part 1: Model sensitivity. *Geosci. Model Dev.*, **13**, 5053–5078, https://doi.org/10.5194/gmd-13-5053-2020.

Han, B., and Coauthors, 2019: Cloud-resolving model intercomparison of an MC3E squall line case: Part II. Stratiform precipitation properties. *J. Geophys. Res. Atmos.*, **124**, 1090–1117, https://doi.org/10.1029/2018JD029596.

Hasager, C. B., F. Vejen, W. R. Skrzypiński, and A.-M. Tilg, 2021: Rain erosion load and its effect on leading-edge lifetime and potential of erosion-safe mode at wind turbines in the North Sea and Baltic Sea. *Energies*, **14**, 1959, https://doi.org/10.3390/en14071959.

Hawbecker, P., S. Basu, and L. Manuel, 2017: Realistic simulations of the July 1, 2011 severe wind event over the Buffalo Ridge Wind Farm. *Wind Energy*, **20**, 1803–1822, https://doi.org/10.1002/we.2122.

Hersbach, H., and Coauthors, 2020: The ERA5 global reanalysis. *Quart. J. Roy. Meteor. Soc.*, **146**, 1999–2049, https://doi.org/10.1002/qj.3803.

Hoen, B. D., J. E. Diffendorfer, J. T. Rand, L. A. Kramer, C. P. Garrity, and H. E. Hunt, 2018: United States wind turbine database v4.3. U.S. Geological Survey, American Clean Power Association, and Lawrence Berkeley National Laboratory, accessed 14 January 2022, https://doi.org/10.5066/F7TX3DN0.

Huffman, G. J., 2019: IMERG v06 quality index. NASA, 5 pp., https://gpm.nasa.gov/sites/default/files/2020-02/IMERGV06_QI_0.pdf.

——, D. T. Bolvin, E. J. Nelkin, E. F. Stocker, and J. Tan, 2019a: V06 IMERG release notes. NASA GSFC Doc., 15 pp., https://gpm.nasa.gov/resources/documents/imerg-v06-release-notes.

——, E. F. Stocker, D. T. Bolvin, E. J. Nelkin, and J. Tan, 2019b: GPM IMERG Final Precipitation L3 Half Hourly 0.1° × 0.1° V06, Goddard Earth Sciences Data and Information Services Center (GES DISC), accessed 2 May 2022, https://doi.org/10.5067/GPM/IMERG/3B-HH/06.

——, D. T. Bolvin, E. J. Nelkin, and J. Tan, 2020a: Integrated Multi-satellitE Retrievals for GPM (IMERG). NASA GSFC Tech. Doc. 612, 83 pp., https://docserver.gesdisc.eosdis.nasa.gov.

——, and Coauthors, 2020b: Integrated Multi-satellitE Retrievals for the Global Precipitation Measurement (GPM) mission (IMERG). *Satellite Precipitation Measurement*, V. Levizzani et al., Eds., Advances in Global Change Research, Vol. 67, Springer, 343–353.

Huschke, R. E., Ed., 1959: *Glossary of Meteorology*. Amer. Meteor. Soc., 638 pp.

International Electrotechnical Commission, 2019: Wind energy generation systems—Part 24: Lightning protection. International Standard IEC61400, International Electrotechnical Commission, 191 pp., https://standards.iteh.ai/catalog/standards/iec/6aae4b87-f0f6-474c-a3ce-da2b91697249/iec-61400-24-2019.

Jiménez, P. A., J. Dudhia, J. F. González-Rouco, J. Navarro, J. P. Montávez, and E. García-Bustamante, 2012: A revised scheme for the WRF surface layer formulation. *Mon. Wea. Rev.*, **140**, 898–918, https://doi.org/10.1175/MWR-D-11-00056.1.

Jones, K. F., A. C. Ramsay, and J. N. Lott, 2004: Icing severity in the December 2002 freezing-rain storm from ASOS data. *Mon. Wea. Rev.*, **132**, 1630–1644, https://doi.org/10.1175/1520-0493(2004)132<1630:ISITDF>2.0.CO;2.

Kain, J. S., 2004: The Kain–Fritsch convective parameterization: An update. *J. Appl. Meteor.*, **43**, 170–181, https://doi.org/10.1175/1520-0450(2004)043<0170:TKCPAU>2.0.CO;2.

——, and J. M. Fritsch, 1993: Convective parameterization for mesoscale models: The Kain–Fritsch scheme. *The Representation of Cumulus Convection in Numerical Models*, Meteor. Monogr., No. 46, Amer. Meteor. Soc., 165–170, https://doi.org/10.1007/978-1-935704-13-3_16.

Katsaprakakis, D. A., N. Papadakis, and I. Ntintakis, 2021: A comprehensive analysis of wind turbine blade damage. *Energies*, **14**, 5974, https://doi.org/10.3390/en14185974.

Keegan, M. H., D. Nash, and M. Stack, 2013: Numerical modelling of hailstone impact on the leading edge of a wind turbine blade. *Proc. EWEA Annual Wind Energy Event 2013*, Vienna, Austria, European Wind Energy Association, 1–11, https://strathprints.strath.ac.uk/id/eprint/42830.

Kendon, E. J., A. F. Prein, C. A. Senior, and A. Stirling, 2021: Challenges and outlook for convection-permitting climate modelling. *Philos. Trans. Roy. Soc.*, **A379**, 20190547, https://doi.org/10.1098/rsta.2019.0547.

Koch, S. E., B. Ferrier, M. T. Stoelinga, E. Szoke, S. J. Weiss, and J. S. Kain, 2005: The use of simulated radar reflectivity

fields in the diagnosis of mesoscale phenomena from high-resolution WRF model forecasts. Preprints, *11th Conf. on Mesoscale Processes*, Albuquerque, NM, Amer. Meteor. Soc., J4J.7, https://ams.confex.com/ams/32Rad11Meso/webprogram/Paper97032.html.

Kumjian, M. R., and K. Lombardo, 2020: A hail growth trajectory model for exploring the environmental controls on hail size: Model physics and idealized tests. *J. Atmos. Sci.*, **77**, 2765–2791, https://doi.org/10.1175/JAS-D-20-0016.1.

Labriola, J., N. Snook, Y. Jung, and M. Xue, 2019a: Explicit ensemble prediction of hail in 19 May 2013 Oklahoma City thunderstorms and analysis of hail growth processes with several multimoment microphysics schemes. *Mon. Wea. Rev.*, **147**, 1193–1213, https://doi.org/10.1175/MWR-D-18-0266.1.

——, ——, M. Xue, and K. W. Thomas, 2019b: Forecasting the 8 May 2017 severe hail storm in Denver, Colorado, at a convection-allowing resolution: Understanding rimed ice treatments in multimoment microphysics schemes and their effects on hail size forecasts. *Mon. Wea. Rev.*, **147**, 3045–3068, https://doi.org/10.1175/MWR-D-18-0319.1.

Letson, F., R. J. Barthelmie, and S. C. Pryor, 2020a: RADAR-derived precipitation climatology for wind turbine blade leading edge erosion. *Wind Energy Sci.*, **5**, 331–347, https://doi.org/10.5194/wes-5-331-2020.

——, T. J. Shepherd, R. J. Barthelmie, and S. C. Pryor, 2020b: WRF modelling of deep convection and hail for wind power applications. *J. Appl. Meteor. Climatol.*, **59**, 1717–1733, https://doi.org/10.1175/JAMC-D-20-0033.1.

Lin, Y., and K. E. Mitchell, 2005: The NCEP stage II/IV hourly precipitation analyses: Development and applications. *Proc. 19th Conf. Hydrology*, San Diego, CA, Amer. Meteor. Soc., 1.2, https://ams.confex.com/ams/Annual2005/techprogram/paper_83847.htm.

Madi, E., K. Pope, W. Huang, and T. Iqbal, 2019: A review of integrating ice detection and mitigation for wind turbine blades. *Renewable Sustainable Energy Rev.*, **103**, 269–281, https://doi.org/10.1016/j.rser.2018.12.019.

Major, D., J. Palacios, M. Maughmer, and S. Schmitz, 2021: Aerodynamics of leading-edge protection tapes for wind turbine blades. *Wind Eng.*, **45**, 1296–1316, https://doi.org/10.1177/0309524X20975446.

Makarskas, V., M. Jurevičius, J. Zakis, A. Kilikevičius, S. Borodinas, J. Matijošius, and K. Kilikevičienė, 2021: Investigation of the influence of hail mechanical impact parameters on photovoltaic modules. *Eng. Failure Anal.*, **124**, 105309, https://doi.org/10.1016/j.engfailanal.2021.105309.

Marion, G., and R. J. Trapp, 2019: The dynamical coupling of convective updrafts, downdrafts, and cold pools in simulated supercell thunderstorms. *J. Geophys. Res. Atmos.*, **124**, 664–683, https://doi.org/10.1029/2018JD029055.

Meredith, E. P., U. Ulbrich, and H. W. Rust, 2020: Subhourly rainfall in a convection-permitting model. *Environ. Res. Lett.*, **15**, 034031, https://doi.org/10.1088/1748-9326/ab6787.

Milbrandt, J. A., and M. K. Yau, 2005: A multimoment bulk microphysics parameterization. Part I: Analysis of the role of the spectral shape parameter. *J. Atmos. Sci.*, **62**, 3051–3064, https://doi.org/10.1175/JAS3534.1.

Min, K.-H., S. Choo, D. Lee, and G. Lee, 2015: Evaluation of WRF cloud microphysics schemes using radar observations. *Wea. Forecasting*, **30**, 1571–1589, https://doi.org/10.1175/WAF-D-14-00095.1.

Mlawer, E. J., S. J. Taubman, P. D. Brown, M. J. Iacono, and S. A. Clough, 1997: Radiative transfer for inhomogeneous atmospheres: RRTM, a validated correlated-*k* model for the longwave. *J. Geophys. Res.*, **102**, 16663–16682, https://doi.org/10.1029/97JD00237.

Morrison, H., and Coauthors, 2020: Confronting the challenge of modeling cloud and precipitation microphysics. *J. Adv. Model. Earth Syst.*, **12**, e2019MS001689, https://doi.org/10.1029/2019MS001689.

Murillo, E. M., and C. R. Homeyer, 2019: Severe hail fall and hailstorm detection using remote sensing observations. *J. Appl. Meteor. Climatol.*, **58**, 947–970, https://doi.org/10.1175/JAMC-D-18-0247.1.

Nakanishi, M., and H. Niino, 2006: An improved Mellor–Yamada level-3 model: Its numerical stability and application to a regional prediction of advection fog. *Bound.-Layer Meteor.*, **119**, 397–407, https://doi.org/10.1007/s10546-005-9030-8.

Newsom, R. K., and R. Krishnamurthy, 2020: Doppler lidar (DL) instrument handbook. DOE Rep. DOE/SC-ARM-TR-101, 58 pp., https://www.arm.gov/publications/tech_reports/handbooks/dl_handbook.pdf.

Nisi, L., A. Hering, U. Germann, and O. Martius, 2018: A 15-year hail streak climatology for the Alpine region. *Quart. J. Roy. Meteor. Soc.*, **144**, 1429–1449, https://doi.org/10.1002/qj.3286.

Niu, G.-Y., and Coauthors, 2011: The community Noah land surface model with multiparameterization options (Noah-MP): 1. Model description and evaluation with local-scale measurements. *J. Geophys. Res.*, **116**, D12109, https://doi.org/10.1029/2010JD015139.

NOAA, 2017: WSR-88D meteorological observations. Part C: WAS-88D products and algorithms. Federal Meteorological Handbook 11, Tech. Rep. FCM-H11C-2017, Office of the Federal Coordinator for Meteorological Services, 396 pp., https://www.icams-portal.gov/resources/ofcm/fmh/FMH11/fmh11partC.pdf.

Ortega, K. L., 2018: Evaluating multi-radar, multi-sensor products for surface hailfall diagnosis. *Electron. J. Severe Storms Meteor.*, **13**, https://ejssm.com/ojs/index.php/site/article/view/69.

Park, H. S., A. V. Ryzhkov, D. S. Zrnić, and K.-E. Kim, 2009: The hydrometeor classification algorithm for the polarimetric WSR-88D: Description and application to an MCS. *Wea. Forecasting*, **24**, 730–748, https://doi.org/10.1175/2008WAF2222205.1.

Pedersen, M. C., T. Ahsbahs, W. Langreder, and M. L. Thøgersen, 2022: On the modelling chain for production loss assessment for wind turbines in cold climates. *Proc. Int. Workshop on Atmospheric Icing of Structures*, Montreal, QC, Canada, McGill University, 047, https://www.mcgill.ca/iwais2022/papers.

Prein, A. F., and G. J. Holland, 2018: Global estimates of damaging hail hazard. *Wea. Climate Extremes*, **22**, 10–23, https://doi.org/10.1016/j.wace.2018.10.004.

——, A. Gobiet, M. Suklitsch, H. Truhetz, N. K. Awan, K. Keuler, and G. Georgievski, 2013: Added value of convection permitting seasonal simulations. *Climate Dyn.*, **41**, 2655–2677, https://doi.org/10.1007/s00382-013-1744-6.

——, R. M. Rasmussen, D. Wang, and S. E. Giangrande, 2021: Sensitivity of organized convective storms to model grid spacing in current and future climates. *Philos. Trans. Roy. Soc.*, **A379**, 20190546, https://doi.org/10.1098/rsta.2019.0546.

Pryor, S. C., and A. N. Hahmann, 2019: Downscaling wind. *Oxford Research Encyclopedia: Climate Science*, H. von Storch, Ed., Oxford University Press, 1–37.

——, F. W. Letson, and R. J. Barthelmie, 2020: Variability in wind energy generation across the contiguous United States.

*J. Appl. Meteor. Climatol.*, **59**, 2021–2039, https://doi.org/10.1175/JAMC-D-20-0162.1.

Qiu, L., E.-S. Im, J. Hur, and K.-M. Shim, 2020: Added value of very high resolution climate simulations over South Korea using WRF modeling system. *Climate Dyn.*, **54**, 173–189, https://doi.org/10.1007/s00382-019-04992-x.

Reynolds, R. W., and D. B. Chelton, 2010: Comparisons of daily sea surface temperature analyses for 2007–08. *J. Climate*, **23**, 3545–3562, https://doi.org/10.1175/2010JCLI3294.1.

Rudlosky, S. D., and H. E. Fuelberg, 2010: Pre-and postupgrade distributions of NLDN reported cloud-to-ground lightning characteristics in the contiguous United States. *Mon. Wea. Rev.*, **138**, 3623–3633, https://doi.org/10.1175/2010MWR3283.1.

Scaff, L., A. F. Prein, Y. Li, C. Liu, R. Rasmussen, and K. Ikeda, 2020: Simulating the convective precipitation diurnal cycle in North America's current and future climate. *Climate Dyn.*, **55**, 369–382, https://doi.org/10.1007/s00382-019-04754-9.

Schlemmer, L., and C. Hohenegger, 2014: The formation of wider and deeper clouds as a result of cold-pool dynamics. *J. Atmos. Sci.*, **71**, 2842–2858, https://doi.org/10.1175/JAS-D-13-0170.1.

Schlie, E. E.-J., D. Wuebbles, S. Stevens, R. Trapp, and B. Jewett, 2019: A radar-based study of severe hail outbreaks over the contiguous United States for 2000–2011. *Int. J. Climatol.*, **39**, 278–291, https://doi.org/10.1002/joc.5805.

Segele, Z. T., L. M. Leslie, and P. J. Lamb, 2013: Weather research and forecasting model simulations of extended warm-season heavy precipitation episode over the US Southern Great Plains: Data assimilation and microphysics sensitivity experiments. *Tellus*, **65A**, 19599, https://doi.org/10.3402/tellusa.v65i0.19599.

Seo, B.-C., B. Dolan, W. F. Krajewski, S. A. Rutledge, and W. Petersen, 2015: Comparison of single-and dual-polarization–based rainfall estimates using NEXRAD data for the NASA Iowa flood studies project. *J. Hydrometeor.*, **16**, 1658–1675, https://doi.org/10.1175/JHM-D-14-0169.1.

Shippert, T., R. Newsom, and L. Riihimaki, 2010: Doppler Lidar Horizontal Wind Profiles (DLPROFWIND4NEWS) wind speed dataset for the SGP Central Facility, Lamont, OK (C1), Atmospheric Radiation Measurement (ARM) Data Center. Subset used: 2 November 2010–17 April 2022, accessed 12 May 2022, https://doi.org/10.5439/1178582.

Shpund, J., and Coauthors, 2019: Simulating a mesoscale convective system using WRF with a new spectral bin microphysics: 1: Hail vs graupel. *J. Geophys. Res. Atmos.*, **124**, 14072–14101, https://doi.org/10.1029/2019JD030576.

Snook, N., Y. Jung, J. Brotzge, B. Putnam, and M. Xue, 2016: Prediction and ensemble forecast verification of hail in the supercell storms of 20 May 2013. *Wea. Forecasting*, **31**, 811–825, https://doi.org/10.1175/WAF-D-15-0152.1.

Squitieri, B. J., and W. A. Gallus Jr., 2020: On the forecast sensitivity of MCS cold pools and related features to horizontal grid spacing in convection-allowing WRF simulations. *Wea. Forecasting*, **35**, 325–346, https://doi.org/10.1175/WAF-D-19-0016.1.

Stephenson, D. B., 2000: Use of the "odds ratio" for diagnosing forecast skill. *Wea. Forecasting*, **15**, 221–232, https://doi.org/10.1175/1520-0434(2000)015<0221:UOTORF>2.0.CO;2.

Stull, R. B., 2017: *Practical Meteorology: An Algebra-Based Survey of Atmospheric Science*. University of British Columbia, 940 pp.

Sun, X., M. Xue, J. Brotzge, R. A. McPherson, X.-M. Hu, and X.-Q. Yang, 2016: An evaluation of dynamical downscaling of central plains summer precipitation using a WRF-based

regional climate model at a convection-permitting 4 km resolution. *J. Geophys. Res. Atmos.*, **121**, 13801–13825, https://doi.org/10.1002/2016JD024796.

Tao, W.-K., D. Wu, S. Lang, J.-D. Chern, C. Peters-Lidard, A. Fridlind, and T. Matsui, 2016: High-resolution NU-WRF simulations of a deep convective-precipitation system during MC3E: Further improvements and comparisons between Goddard microphysics schemes and observations. *J. Geophys. Res. Atmos.*, **121**, 1278–1305, https://doi.org/10.1002/2015JD023986.

Tilg, A.-M., C. B. Hasager, H.-J. Kirtzel, and P. Hummelshoj, 2020: Brief communication: Nowcasting of precipitation for leading edge erosion-safe mode. *Wind Energy Sci.*, **5**, 977–981, https://doi.org/10.5194/wes-5-977-2020.

Tokay, A., D. B. Wolff, and W. A. Petersen, 2014: Evaluation of the new version of the laser-optical disdrometer, OTT Parsivel². *J. Atmos. Oceanic Technol.*, **31**, 1276–1288, https://doi.org/10.1175/JTECH-D-13-00174.1.

Trapp, R. J., K. A. Hoogewind, and S. Lasher-Trapp, 2019: Future changes in hail occurrence in the United States determined through convection-permitting dynamical downscaling. *J. Climate*, **32**, 5493–5509, https://doi.org/10.1175/JCLI-D-18-0740.1.

van Oldenborgh, G. J., and Coauthors, 2017: Attribution of extreme rainfall from Hurricane Harvey, August 2017. *Environ. Res. Lett.*, **12**, 124009, https://doi.org/10.1088/1748-9326/aa9ef2.

Verrelle, A., D. Ricard, and C. Lac, 2015: Sensitivity of high-resolution idealized simulations of thunderstorms to horizontal resolution and turbulence parametrization. *Quart. J. Roy. Meteor. Soc.*, **141**, 433–448, https://doi.org/10.1002/qj.2363.

Wallace, R., K. Friedrich, E. A. Kalina, and P. Schlatter, 2019: Using operational radar to identify deep hail accumulations from thunderstorms. *Wea. Forecasting*, **34**, 133–150, https://doi.org/10.1175/WAF-D-18-0053.1.

Wang, D., M. Bartholomew, and Y. Shi, 2016: Laser Disdrometer (LD) dataset for the SGP Central Facility, Lamont, OK (C1), Atmospheric Radiation Measurement (ARM) Data Center. Subset used: 2 November 2016–8 April 2022, accessed 18 April 2022, https://doi.org/10.5439/1779709.

——, S. E. Giangrande, Z. Feng, J. C. Hardin, and A. F. Prein, 2020: Updraft and downdraft core size and intensity as revealed by radar wind profilers: MCS observations and idealized model comparisons. *J. Geophys. Res. Atmos.*, **125**, e2019JD031774, https://doi.org/10.1029/2019JD031774.

Wendt, N. A., and I. L. Jirak, 2021: An hourly climatology of operational MRMS MESH-diagnosed severe and significant hail with comparisons to storm data hail reports. *Wea. Forecasting*, **36**, 645–659, https://doi.org/10.1175/WAF-D-20-0158.1.

Wilks, D. S., 2020: *Statistical Methods in the Atmospheric Sciences*. 4th ed. Elsevier, 840 pp.

Witt, A., M. D. Eilts, G. J. Stumpf, J. T. Johnson, E. D. W. Mitchell, and K. W. Thomas, 1998: An enhanced hail detection algorithm for the WSR-88D. *Wea. Forecasting*, **13**, 286–303, https://doi.org/10.1175/1520-0434(1998)013<0286:AEHDAF>2.0.CO;2.

Yang, Q., R. A. Houze Jr., L. R. Leung, and Z. Feng, 2017: Environments of long-lived mesoscale convective systems over the central United States in convection permitting climate simulations. *J. Geophys. Res. Atmos.*, **122**, 13288–13307, https://doi.org/10.1002/2017JD027033.

Zscheischler, J., P. Naveau, O. Martius, S. Engelke, and C. C. Raible, 2021: Evaluating the dependence structure of compound precipitation and wind speed extremes. *Earth Syst. Dyn.*, **12**, 1–16, https://doi.org/10.5194/esd-12-1-2021.

## **Appendix B:**

Reference: Pryor S.C., Barthelmie R.B., Coburn J.J., Zhou X., Rodgers M., Norton M., Campobasso M.S., Lopez B.M., Hasager C.B., and Mishnaevsky Jr L. (2024): Prioritizing Research for Enhancing the Technology Readiness Level of Wind Turbine Blade Leading Edge Erosion Solutions. *Energies* **17** 6285 doi: 10.3390/en17246285. Reproduced with kind permission from the journal

*Article*

# Prioritizing Research for Enhancing the Technology Readiness Level of Wind Turbine Blade Leading-Edge Erosion Solutions

Sara C. Pryor [1,*], Rebecca J. Barthelmie [2], Jacob J. Coburn [1], Xin Zhou [1], Marianne Rodgers [3], Heather Norton [3], M. Sergio Campobasso [4], Beatriz Méndez López [5], Charlotte Bay Hasager [6] and Leon Mishnaevsky, Jr. [6]

1   Department of Earth and Atmospheric Sciences, Cornell University, Ithaca, NY 14853, USA; jjc457@cornell.edu (J.J.C.); xin.zhou@cornell.edu (X.Z.)
2   Sibley School of Mechanical and Aerospace Engineering, Cornell University, Ithaca, NY 14853, USA; rb737@cornell.edu
3   Wind Energy Institute of Canada, Tignish, PE C0B 2B0, Canada; marianne.rodgers@weican.ca (M.R.); heather.norton@weican.ca (H.N.)
4   School of Engineering, University of Lancaster, Lancaster LA1 4YW, UK; m.s.campobasso@lancaster.ac.uk
5   National Renewable Energy Center (CENER), 31621 Sarriguren, Spain; bmendez@cener.com
6   Department of Wind and Energy Systems, Technical University of Denmark, 4000 Roskilde, Denmark; cbha@dtu.dk (C.B.H.); lemi@dtu.dk (L.M.J.)
*   Correspondence: sp2279@cornell.edu; Tel.: +1-607-255-3376

**Abstract:** An enhanced understanding of the mechanisms responsible for wind turbine blade leading-edge erosion (LEE) and advancing technology readiness level (TRL) solutions for monitoring its environmental drivers, reducing LEE, detecting LEE evolution, and mitigating its impact on power production are a high priority for all wind farm owners/operators and wind turbine manufacturers. Identifying and implementing solutions has the potential to continue historical trends toward lower Levelized Cost of Energy (LCoE) from wind turbines by reducing both energy yield losses and operations and maintenance costs associated with LEE. Here, we present results from the first Phenomena Identification and Ranking Tables (PIRT) assessment for wind turbine blade LEE. We document the LEE-relevant phenomena/processes that are deemed by this expert judgment assessment tool to be the highest priorities for research investment within four themes: atmospheric drivers, damage detection and quantification, material response, and aerodynamic implications. The highest priority issues, in terms of importance to LEE but where expert judgment indicates that there is a lack of fundamental knowledge, and/or implementation in measurement, and modeling is incomplete include the accurate quantification of hydrometeor size distribution (HSD) <u>and</u> phase, the translation of water impingement to material loss/stress, the representation of operating conditions within rain erosion testers, the quantification of damage and surface roughness progression through time, and the aerodynamic losses as a function of damage morphology. We discuss and summarize examples of research endeavors that are currently being undertaken and/or could be initiated to reduce uncertainty in the identified high-priority research areas and thus enhance the TRLs of solutions to mitigate/reduce LEE.

**Keywords:** blades; expert judgment; LEE; machine learning; PIRT; TRL; wind turbine

## 1. Introduction

### 1.1. Background and Motivation

The global wind resource greatly exceeds both current electricity demand and total primary energy supply [1]. Wind energy is a potential mechanism to reduce energy-related environmental issues (e.g., anthropogenic climate forcing [2]) and to enhance energy security [3,4]. Many countries have ambitious plans to expand both onshore and offshore wind energy installed capacity [5]. Thus, it is expected that more wind turbines will be deployed, and we will become increasingly reliant on them for electricity generation.

The Levelized Cost of Energy (*LCoE*) in \$/MWh of electricity can be computed from

$$LCoE = \frac{\sum_{n=1}^{i} (CAPEX_n + O\&M_n)/(1+r)^n}{\sum_{n=1}^{i} AEP/(1+r)^n} \tag{1}$$

where *CAPEX* = capital expenditures in each year (*n*); *O&M* = operations and maintenance costs in each year; *r* = annual discount rate; *AEP* = amount of electricity (in MWh) produced each year; *i* = wind turbine lifetime in years.

In locations with good wind resources, onshore wind energy has the lowest LCoE of any electricity generation type [6]. However, LCoE from onshore wind energy is no longer declining [7], and costs for offshore deployments exceed those for onshore [8].

O&M typically account for 25–30% of the lifecycle LCoE from wind turbines [9]. Blades contribute > 20% of the overall cost of wind turbines [10], and blade integrity is a fundamental determinant of both O&M and power generation (AEP). An important contributing factor to wind turbine blade lifespan is leading-edge erosion (LEE). LEE refers to the material loss of wind turbine blade coatings leading to exposure and ultimately loss of the laminate that provides the structure of the blade. It results primarily from materials stresses induced when hydrometeors (e.g., rain droplets or hailstones) impact the rapidly rotating blades [11–14]. The material loss leads to a roughening of the surface, reducing lift and increasing drag [15], and thus negatively impacts AEP [15–19]. LEE requiring emergency blade repair can occur within two years of installation [20], which is far short of the expected lifetime of 30 years [21]. O&M expenditures associated with total blade replacement for onshore wind turbines are >\$200,000 and blade replacement may lead to multiple days of lost power production [22].

Wind turbines being deployed offshore are physically larger and have both longer blades and higher tip speeds than those deployed onshore [23]. This leads to higher closing velocities with falling hydrometeors, higher materials stresses [20], and thus a higher erosion rate [24,25]. Wind turbines being deployed at the South Fork Wind Farm off the USA East Coast are GE Haliade-X 13 MW machines with blades 107 m in length, each of which weighs 55 tons [26]. These wind turbines have maximum tip speeds of >90 ms$^{-1}$. The 22 MW reference wind turbine that has recently been released for use in offshore research [27] has even longer blades and a rated tip speed of 105 ms$^{-1}$. Manufacturing defects and damage during transportation/deployment are likely enhanced in longer blades [28,29] and even small imperfections may be important sites for the initiation of LEE [29]. Thus, LEE issues may be particularly prominent offshore where O&M costs are much higher [23], and the avoidance of excess maintenance is paramount to reducing the LCoE. In 2018, Renew.Biz reported that the consortium behind the 630 MW London Array in the UK was planning "emergency" blade repair to 140 of the project's 175 wind turbines and that 'A similar repair campaign has begun at Orsted's 400 MW Anholt wind farm off Denmark, where 87 of 111 . . . . . . turbines are being fitted with rubber-like shells to fix the problem'.

LEE thus represents an important challenge to the cost-effectiveness and reliability of wind-derived electricity and there is a need to advance the fundamental understanding of the processes that cause LEE and to advance effective solutions.

### *1.2. The Interdisciplinary Nature of LEE: Introduction to the Four LEE Themes*

Over 40 years ago, the US National Aeronautics and Space Administration introduced "technology readiness levels" (TRLs) as a conceptual framework for measuring and articulating the maturity, or readiness for deployment, of emerging technologies. TRL assessments are usually based on a 9-point scale with higher values indicating more mature technologies and lower values indicating more nascent technologies that are in the stages of basic research, or feasibility studies [30,31].

Enhancement of the TRLs for solutions to mitigate/reduce LEE requires multidisciplinary research within four linked themes (Figure 1). Theme 1 is focused on the atmospheric drivers of LEE and thus requires research primarily in the field of atmospheric

science. Theme 2 is focused on the detection and quantification of blade damage and thus requires research primarily within imaging and image processing plus acoustic monitoring. Theme 3 is focused on blade response/redesign/repair/protection and thus requires research primarily within the material science field. Theme 4 is focused on the detection of aerodynamic changes due to LEE and the estimation of resulting power reduction and thus requires research primarily within the field of aerodynamics. All themes further require advances in computational tools and measurement technologies. An introduction to each of these themes is briefly given below.
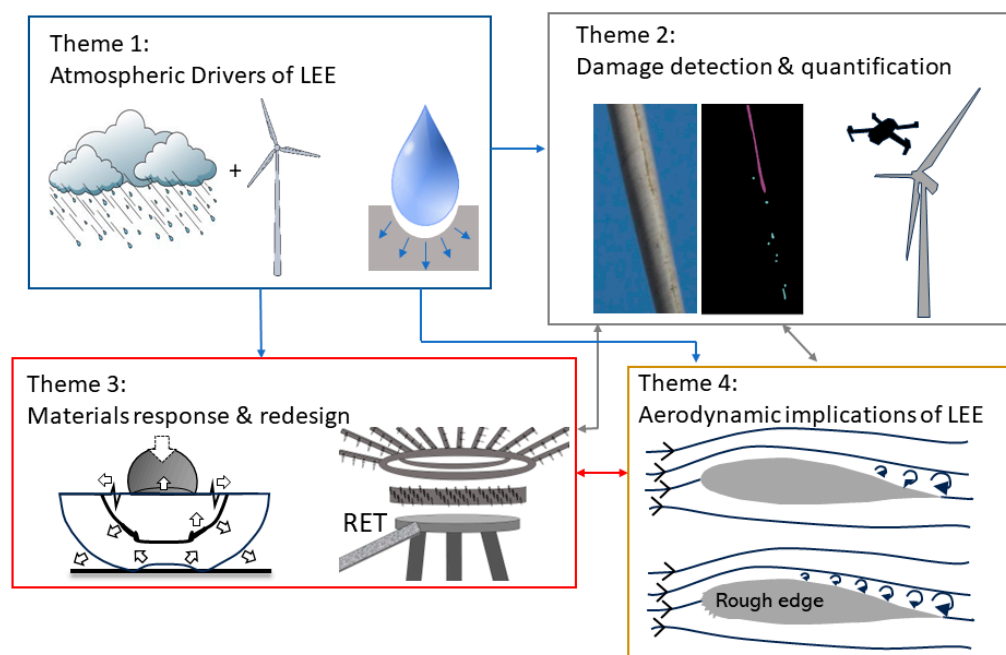


**Figure 1.** Schematic overview of the four LEE themes. RET = rain erosion tester. Arrows show primary information links between the themes.

### 1.2.1. Theme 1—Atmospheric Drivers of LEE

The amount of kinetic energy transferred into the blade from an ensemble of falling hydrometeors and the material response is dictated by the closing velocity ($v_c$) between the falling hydrometeor(s) and the rotating blades, plus the number, diameter (D), and phase of hydrometeors (i.e., hailstones, graupel, or rain droplets). The impact force and the kinetic energy transferred into the coating scales with the hydrometeor mass and closing velocity squared [32]. Larger diameter drops may be of greater importance in dictating the kinetic energy transfer to the blades and hence the duration of the incubation period (i.e., the period prior to material loss, see details below) [14,33] while smaller drops may be more critical in the transition and steady state progression [34]. The water-hammer equation describes the pressure exerted on a coating by the impact as a function of closing velocity [32,35,36]. For $v_c = 80$ ms$^{-1}$, a single 2 mm diameter rain droplet may exert a pressure of up to 120 MPa on the blade surface [32]. The hydrometeor phase is of importance because the material response to hail (ice) exceeds that due to collisions with rain (liquid) droplets [32,37–40]. As few as five hailstone impacts (D of 15 and 20 mm) at $v_c \geq 110$ ms$^{-1}$ can cause damage to a glass-fiber-reinforced plastic composite [41]. Thus, the prediction of LEE requires accurate and consistent descriptions of hydroclimate conditions, including precipitation intensity, phase, and hydrometeor size distributions (HSD) from measurements and models across the wide range of environments in which wind turbines are or will be deployed. However, as discussed in detail below, best practice for the selection and operation of precipitation sensors within the context of LEE has not yet been advanced [14], and numerical models

exhibit only partial fidelity for precipitation rate and phase, and most simulations do not explicitly simulate or output HSD.

A hierarchy of models have been generated to translate precipitation intensity/HSD and closing velocities to estimates of potential erosion. First-order erosion models rely on the volume (or depth) of impinged water without the explicit consideration of hydrometeor size and/or phase [24]. Alternatively, VN curves (velocity–number of impacts to failure, see 'material response') derived from rain erosion testers can be used to articulate functions that describe the number of impacts at a given closing velocity for a given hydrometeor diameter required for the initiation of coating damage and that can be used (with caution) to extend beyond the measured range of closing velocities. For example, assuming all hydrometeors have the same effective diameter, the accumulated distance to failure (*ADF*) of the coating is given by the following:

$$ADF = \sum_{i=1}^{j} \frac{\frac{V_{tip} \cdot I \cdot \Delta t}{v_f}}{H_0 \cdot \left(\frac{v_c}{V_0}\right)^m} \tag{2}$$

where $V_0$ is 1 ms$^{-1}$, $v_c$ is the closing velocity between the hydrometeor and blade, $v_f$ is the hydrometeor fall velocity (ms$^{-1}$), $\Delta t$ is the time interval (s) for the specification of the tip speed and precipitation intensity (*I*, in ms$^{-1}$). $H_0$ and m are fitting parameters that are specific to the coating material tested, but for one coating and D = 0.76, these fitting parameters are $2.85 \times 10^{22}$ m and $-10.5$, respectively [42]. The summation is over all time periods: *i* = 1 to *j*. Thus, the challenge is to specify a representative effective diameter to characterize the precipitation that falls from stratiform and cumulus clouds and over a wide range of intensity ranges [43]. More mechanistic models require greater specificity in terms of the HSD/phase and range of fall velocities and are described below in Theme 3.

Less is known regarding the possible contribution of other meteorological variables to LEE. Prolonged exposure to radiation within the visible range, and particularly UV-A (wavelengths ($\lambda$) = 320 and 400 nm), may lead to the degradation of polyurethane coatings [32,44]. Theoretical and experimental work has also indicated that low temperatures degrade the erosion performance of polyurethane-protective leading-edge coatings [45]. Thermal cycling (expansion and contraction of the blades) is an important source of material wear [46]. Other plausible meteorological co-stressors include impacts from aerosols (e.g., wind-blown dust/sand [47,48]) and ice accretion on blades [49].

### 1.2.2. Theme 2—Damage Detection and Quantification

LEE pattern categorization frequently employs five classes, with Class 1 "small pinholes" exhibiting an erosion depth of 0.1–0.2 mm, an average feature damage of 2 mm, and an approximate cord coverage of 3% [17]. Even Class 1 LEE may result in AEP loss. The early detection and close monitoring of damage progress can help optimize mitigation strategies and identify appropriate maintenance actions (patching and minor repair to full-scale blade removal) [50–53].

Current techniques for real-time wind turbine blade damage detection [54,55] include vibration-based techniques [56], ultrasound scanning techniques [57], acoustic emission monitoring [58], and machine vision, image, or video processing [59]. Three out of four of these LEE detection methods (acoustic emission, ultrasound, vibration-based techniques) require the use of physical sensors placed along the blade or near the wind turbine, which can be costly and vulnerable to damage in extreme meteorological conditions [60]. Image processing methods can be used to assess blade conditions from 2D and 3D images or videos captured by instrumentation deployed on unmanned aerial vehicles (UAVs) [61] or taken by technicians [62]. However, as discussed below, the fidelity of different damage detection methods has not been fully quantified.

1.2.3. Theme 3—Material Response

Wind turbine blades are made of composites (e.g., epoxy or polyester, with reinforcing glass or carbon fibers) [63] coated to protect them by distributing and absorbing energy from hydrometeor and other impacts [64]. Defects such as air bubbles in these coatings have a critical impact on crack initialization [65] and re-emphasize the importance of wind turbine blade manufacturing quality in dictating erosion rates.

Erosion mechanics comprises an incubation period during which no damage is observed but microstructural material changes can generate nucleation sites for subsequent material removal. Material removal commences when a threshold level of accumulated impacts is reached [66]. This is followed by a period during which additional impacts lead to observable damage as stress waves propagate from impact locations. This leads to the growth of pits/cracks and an increase in material loss [67–69]. The number of impacts required to reach the threshold at which material failure becomes evident is thus a nonlinear function of the number, magnitude, and phase of the hydrometeors and the hydrometeor closing velocity plus the material strength [70].

Whirling Arm Rain ERosion testers (WARERs, or more simply rain erosion testers, RET) artificially simulate the erosion process by spinning a sample of the blade, often with a leading-edge protection applied, at very high speeds and bombarding the sample with liquid droplets (of a confined droplet diameter range) supplied via needles [71]. These experiments can be used to develop VN curves and thus to derive empirical coefficients for use in Equation (2). However, the range of closing velocities sampled and used to derive the fitting parameters m and $H_0$ specified below in Equation (2) for hydrometeor D of 0.76 mm are 90 to 150 ms$^{-1}$, and thus exceed many of those that will occur.

Alternatively, a range of modeling techniques have been advanced to simulate the process of material stresses that lead to LEE as a function of hydrometeor size distribution and closing velocity [68,70,72]. The simplest method is to employ the Springer model [73,74] combined with Miner's rule to integrate across all hydrometeor diameters (and time) to quantify the accumulated distance to failure (ADF) [66,75]. However, these simple engineering models of LEE include multiple coefficients/assumptions that limit the robustness of lifetime estimates, and when invoking Miner's rule, the damage is assumed to be linearly accumulated.

1.2.4. Theme 4—Aerodynamic Implications

A smooth leading edge reduces turbulence and drag, optimizing the lift-to-drag ratio of a wind turbine blade. The outer part of the blade (toward the tip) produces most of the energy and experiences the highest relative wind speeds. Thus, the leading edge toward the blade tip is both the most vulnerable to roughening by material loss and is also where reducing lift/increasing drag maximizes the negative impacts on the AEP. The maximum lift force on blades has been modeled to be reduced for damage associated with roughness heights of 0.11 mm for a rotor with a 175 m diameter [16]. Erosion classes 3 to 5 (large patches of missing coating, the erosion of laminate, and the complete loss of laminate, respectively), are associated with AEP reductions of 1–5% [76]. Recent reports found LEE-induced AEP losses from onshore wind turbines after only 1–3 years [77], but there is a paucity of data regarding underlying blade LEE topologies. The damage location on the blade is known to play a critical role in the alteration of the aerodynamic behavior, and so there are clear links between Themes 2 and 4 [78].

The Simplified Aerodynamic Loss Tool (SALT) [79] can be used to illustrate the predicted effect of erosion on the power coefficient ($C_P$) and the AEP loss relative to clean or undamaged blades, while acknowledging that it omits many of the details of more complex models [80]. Within SALT, damage is specified in 2% increments over the outer 70% of the blade (location r as a fraction of blade radius R) using a five-level categorization. Category a is undamaged, and the lift-to-drag ratio loss factor is 1. Category e represents the most severe damage which is deeper than 0.3% of the blade chord and the lift-to-drag ratio loss factor = 0.3. For the IEA 15 MW reference wind turbine [81] and a hub-height wind speed

of 10 ms$^{-1}$, the $C_P$ for an entirely undamaged blade is ~0.4551, reducing it to ~0.2907 for category e damage. $C_P$ correction factors (multipliers to $C_P$) are shown as a function of r/R in Figure 2a for a wind speed of 10 ms$^{-1}$. The impact of the roughening of the leading edge on the blade lift and drag and the power production is a nonlinear function of inflow wind speed and is specifically important at the below-rated wind speeds (Figure 2b) and also depends on turbulence intensity [19]. Thus, the AEP loss is dependent on the site's wind climate. Assuming a Weibull distribution of hub-height wind speeds for a typical US Central Plains site [14], the AEP loss for different erosion levels along the outer 70% of the blade is shown in Figure 2c. While this analysis is useful for illustrative purposes, uniform damage is unlikely to occur across such large areas of a blade, thus the AEP loss estimates greatly exceed those that are likely to be observed. Further, the attribution of any loss in blade performance to any specific cause (e.g., LEE, gearbox wear-and-tear, the soiling of blades) is very challenging [82,83], particularly in operating wind farms.
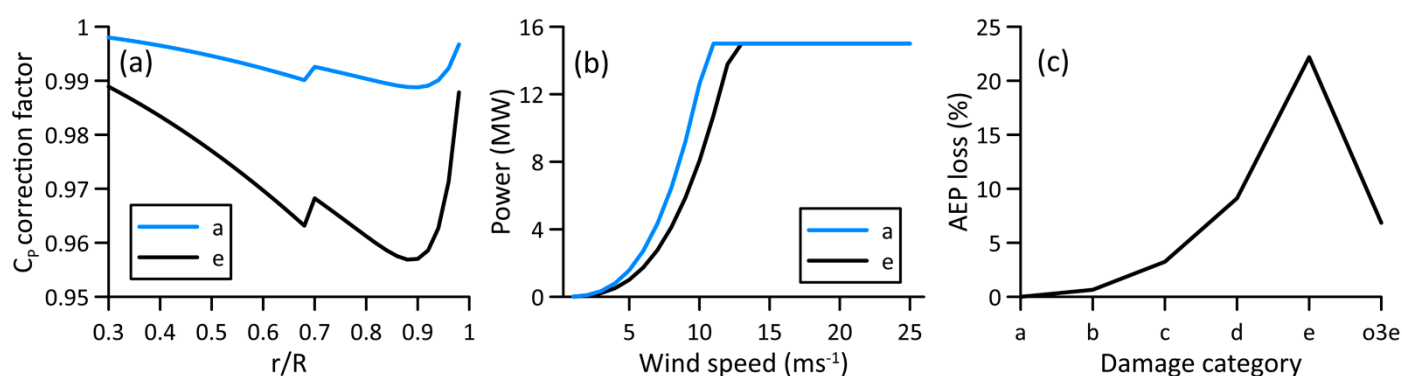


**Figure 2.** Results from the SALT model for (**a**) $C_P$ correction factors as a function of distance along the blade for a clean blade (shown by the blue line, Category a damage) and substantial damage (shown by the black line, Category e damage) along the outer two-thirds of the blade for a hub-height wind speed of 10 ms$^{-1}$ for the IEA 15 MW reference wind turbine. (**b**) Power curves (power generation as a function of hub-height wind speed) for the IEA 15 MW reference wind turbine for a clean blade (Category a damage) and a damaged blade (Category e damage). (**c**) AEP loss for damage categories a to e and o3e (level 3 damage only for the outer one-third of the blade) for the IEA 15 MW reference wind turbine and the Weibull-distributed wind speeds from a US Southern Great Plains site [14].

Optimizing O&M as LEE progresses for cost-effectiveness requires not only accurate damage assessment but also a robust, quantitative understanding of the effect of LEE on blade aerodynamics. For example, if the damage is minor pitting without material losses, the aerodynamic efficiency may only be slightly lower than its design, and potentially only impacts the aerodynamics at some tip speed ratios. In this case, unless the damage is likely to propagate, it may be more cost-effective to wait rather than to order repairs. On the other hand, if material damage has penetrated beyond the blade coating, even a small gouge may potentially leave open the possibility of further material loss and extensive delamination impacting not only the aerodynamics but necessitating costly on-site repairs.

*1.3. Possible Solutions for Leading-Edge Erosion*

Fundamentally, efforts to reduce LEE can be placed into two classes:

- Enhanced blade resilience: This may be achieved by blade redesign and/or the use of improved materials (e.g., more energy consuming coatings) [84,85], improved manufacturing, and/or the use of leading-edge protection (LEP) products. A range of LEP products are available including the following: (1) In-mould application of a gelcoat (e.g., epoxy) during blade manufacturing or co-bonding to an erosion shield (rigid/semi-rigid covers). (2) Post-mould application of flexible coatings (e.g., polyurethane [86]) using sprayers/rollers or flexible tapes [87] or thermoplastic ero-

sion shields [88]. The details of the relative merits of these solutions, including their durability have been previously reviewed [20,89,90]. Best practice for the optimal length of LEP from the tip of the blade is being investigated [91] as is the optimal thickness of application [92]. All protective solutions incur additional costs and reductions in aerodynamic performance and AEP. For example, some research has reported 2–3% AEP losses from LEP tapes [15,87]. Further, some post-mould LEP products are challenging to apply (see below, Section 3.4) and/or lack durability [93].

- Operation of wind turbines in a manner to reduce materials stresses: Specifically, use of erosion safe mode [11] wherein wind turbine operation is modified during highly erosive periods to reduce blade rotational speed, thus sacrificing the AEP to elongate blade lifetime [94].

Both classes of solution require a detailed assessment of site conditions regarding likely severity of LEE since the incubation, transition, and steady state progression of damage on the leading edge differs as a function of precipitation climate and possibly other operating conditions [16]. A quantitative comparison of overall cost effectiveness requires detailed information regarding (i) AEP loss from LEE, LEP application (including down-time if LEP is applied post-commissioning) and/or the adoption of erosion safe mode. (ii) The cost of LEP measures and the expense of deployment [22] and robust economic/financial information such as the spot market price for electricity [95]. Ultimately, an optimal solution is likely to be one which maximizes revenues over a specific period of time for a given wind farm [96]. The consideration of either solution type for a given situation demands robust knowledge of processes/phenomena in each of the four themes described above. Thus, the issue confronting the wind energy industry is how to prioritize research to reduce uncertainty and increase confidence for wind farm owners/operators and enhance the TRL for LEE mitigation.

### 1.4. Objectives of This Work

Our goal is to map priorities for LEE research that can enhance the technology readiness levels for LEE solutions such as those described in Section 1.3, and thus aid in reducing the LCoE from wind turbines. To achieve this goal, we undertook, and herein present, the first Phenomena Identification and Ranking Tables (PIRT) assessment for wind turbine blade LEE (Section 2). Following the presentation of the PIRT analysis, we discuss the research required and/or being conducted to address the highest priority research needs identified during the PIRT process and that are necessary to enhanced TRLs of LEE solutions (Section 3). We conclude in Section 4 by describing the next steps.

## 2. PIRT

The PIRT process (MATLAB R2024a from MathWorks) is a systematic way of gathering information regarding processes on a specific concept and ranking their importance to meet some decision-making objective such as the prioritization of research activities to enhance the TRL. PIRT has been widely applied within, for example, nuclear safety [22,97,98], but is gaining traction in other disciplines [99].

A schematic workflow of the PIRT process as applied in this research is given in Figure 3. Steps 1 and 2 require the identification of a topic of interest and then the articulation of the PIRT objective(s). To aid in structuring the PIRT by thematically clustering processes/phenomena, in Step 3 four LEE themes were articulated (Section 1). The PIRT analysis then proceeded by polling experts to identify key phenomena in each of these LEE themes, acknowledging that some phenomena cross the thematic boundaries. Following best practice in prior PIRT analyses [22], once each of the processes/phenomena were identified, domain experts were asked to provide for each a ranking of 'high', 'medium', or 'low' priority. To derive a mean ranking and the standard deviation (SD) across respondents, rankings of 'high' were allocated 1 point, medium as 0.5, and low as 0. As an example, the need for hydrometeor size distributions (HSD) (jointly with wind speeds) to inform LEE assessment was given a mean ranking of 0.86 and the standard deviation was 0.32

(Table 1). These rankings are because >80% of respondents gave a ranking of high, and approximately 10% gave a ranking of either medium or low.
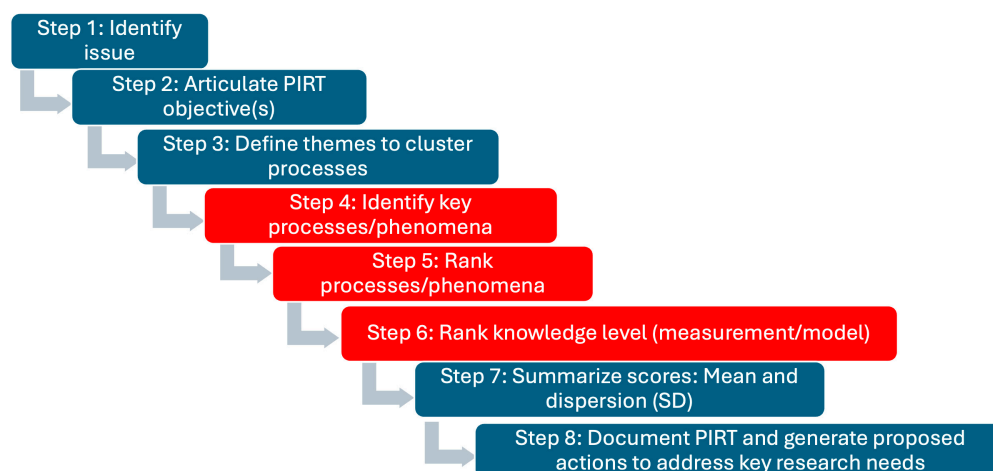


**Figure 3.** Workflow of the PIRT process. Steps in red indicate solicitation of expert judgments.

The second component of PIRT analyses (Step 6) is to evaluate the state of knowledge with respect to each process/phenomenon. Here, we broke this down into two aspects:

1. What is the state of knowledge regarding this phenomenon/process and how well has knowledge regarding this process/phenomenon been translated into measurement technologies and data analysis procedures?
2. What is the state of knowledge regarding this phenomenon/process and how well has knowledge regarding this process/phenomenon been translated into state-of-the-art modeling tools?

Conceptually, the goal of this combined rating system is to identify phenomena/processes that have high importance and where critical knowledge gaps preclude full treatment of those phenomena/processes in numerical models or current measurement technologies and data analysis tools. Such phenomena/processes will have high importance ratings but low measurement/modeling ratings. Advancing knowledge for these topics is most likely to enhance TRLs for LEE solutions. In this preliminary PIRT analysis, respondents were also encouraged to supply narratives explaining their rankings.

Based on PIRT, one can identify key processes and phenomena that are of high importance but where the state-of-the-art ability to measure or simulate them is deemed good. An example is hub-height wind speeds at operating wind farms. These wind speeds are critical to power production and blade tip speed predictions. The mean ranking for phenomena importance was >0.9 with small standard deviation (≤0.2) indicating a consensus of this ranking. But the ratings for the translation of knowledge to measurements and/or models is also rated as high. Nacelle-mounted anemometers and/or remote sensing technologies such as lidars have been demonstrated to have relatively high fidelity with respect to wind speeds within the rotor plane even in complex terrain [100] and offshore [101]. Multiple modeling exercises have also demonstrated that numerical weather prediction (NWP) models such as the Weather Research and Forecasting (WRF) model, particularly when coupled with micro-scale flow models, also exhibit relatively high fidelity [102]. This does not imply that there is not a need for continuing to improve measurement and modeling capabilities but that, in the context of LEE, other research activities should be prioritized.

**Table 1.** PIRT analysis results. Column 1: Processes/phenomena of interest. Columns 2 and 3: Mean (mean) ranking and the standard deviation (SD) of the rankings across respondents. Expert judgment evaluation of the knowledge regarding each process/phenomenon as translated into state-of-the-art measurements (columns 4 and 5) and modeling (columns 6 and 7). Items in black have high importance (mean > 0.8) and process-level understanding has been well translated to measurement technologies and/or modeling (mean > 0.5). Processes/phenomena in red have high importance (mean > 0.8) but process-level knowledge is lacking and/or translation of that knowledge to measurement and modeling capabilities is poor (mean < 0.5) and thus are defined as tier 1 for research. Items in blue are tier 2 priorities for research; moderate importance (0.5 < mean < 0.8) and process-level knowledge and translation to models and measurements are incomplete (mean < 0.6). Items in green have importance level scores (mean < 0.5). Note: processes/phenomena are listed in the order in which they were presented to the respondents to avoid confusion that the ranked order of importance is systematically a function of the row number in the PIRT.

| | Processes/Phenomena Importance Level | | Measurement | | Modeling | |
|---|---|---|---|---|---|---|
| **Theme 1: Atmospheric drivers** | Mean | SD | Mean | SD | Mean | SD |
| Hub-height wind speeds: existing wind farms | 0.92 | 0.19 | 1 | 0 | 0.73 | 0.26 |
| Hub-height wind speeds: prospective wind farms | 0.91 | 0.2 | 0.82 | 0.25 | 0.68 | 0.25 |
| Hydrometeor size distribution | 0.86 | 0.32 | 0.27 | 0.41 | 0.2 | 0.26 |
| Hydrometeor phase (rain/hail/other) | 0.91 | 0.3 | 0.36 | 0.39 | 0.14 | 0.23 |
| Hydrometeor fall velocities | 0.58 | 0.36 | 0.41 | 0.38 | 0.32 | 0.34 |
| Impinged water (blade capture efficiency as a function of droplet diameter) | 0.55 | 0.44 | 0.15 | 0.34 | 0.1 | 0.21 |
| Real-time data for 'erosion safe mode' | 0.68 | 0.25 | 0.18 | 0.34 | 0.46 | 0.33 |
| Space/time variability in hydroclimate conditions | 0.64 | 0.23 | 0.59 | 0.2 | 0.59 | 0.2 |
| Non-hydrometeor weathering stressors (e.g., UV radiation, icing, thermal expansion, aerosols (incl. dust and pollution)) | 0.55 | 0.27 | 0.18 | 0.25 | 0.27 | 0.34 |
| Reanalysis/gridded product data quality | 0.44 | 0.17 | 0.67 | 0.25 | 0.81 | 0.26 |
| **Theme 2: Damage detection and quantification** | Mean | SD | Mean | SD | Mean | SD |
| Availability of blade images and methods to quantify damage | 0.83 | 0.25 | 0.54 | 0.33 | 0.5 | 0.33 |
| Damage characterization from varying image types and methods to translate to damage classification | 0.88 | 0.23 | 0.58 | 0.29 | 0.44 | 0.3 |
| Methods for 3D characterization of damage morphology and rate of progression | 0.71 | 0.26 | 0.25 | 0.26 | 0.18 | 0.25 |
| Translating water impingement to material loss/stress (e.g., metrics: kinetic energy, Springer–ADF, VN curves) | 0.86 | 0.23 | 0.27 | 0.26 | 0.36 | 0.23 |
| Quantification of material loss | 0.71 | 0.26 | 0.5 | 0.39 | 0.27 | 0.26 |
| Quantification of equivalent surface roughness for aerodynamic loss | 0.75 | 0.26 | 0.41 | 0.3 | 0.45 | 0.27 |
| Microplastic loss for environmental impacts | 0.5 | 0.21 | 0.21 | 0.26 | 0.27 | 0.26 |

<div align="center">**Table 1.** *Cont.*</div>

| | Processes/Phenomena Importance Level | | Measurement | | Modeling | |
|---|---|---|---|---|---|---|
| **Theme 3: Material response** | Mean | SD | Mean | SD | Mean | SD |
| Rain erosion tester reliability and reproducibility | 0.92 | 0.19 | 0.59 | 0.3 | 0.4 | 0.21 |
| Rain erosion tester representation of atmospheric conditions: hydrometeors: phase (e.g., rain and hail), size distributions and collision velocities | 0.83 | 0.25 | 0.5 | 0.33 | 0.28 | 0.26 |
| Rain erosion tester representation of atmospheric conditions: flow field (e.g., impact velocities) | 0.71 | 0.33 | 0.45 | 0.28 | 0.28 | 0.36 |
| Methodologies to translate lab experimental data (incl. rain erosion tester) to field conditions and failure modes | 0.88 | 0.23 | 0.35 | 0.24 | 0.3 | 0.26 |
| Damping and energy dissipation properties of LEPs/coatings (single/multilayer) | 0.67 | 0.25 | 0.32 | 0.25 | 0.45 | 0.16 |
| Linking mechanical and viscoelastic properties to failure mechanisms/modes | 0.73 | 0.26 | 0.32 | 0.25 | 0.4 | 0.32 |
| Coating adhesion and mechanics of multi-layer materials | 0.75 | 0.26 | 0.45 | 0.44 | 0.55 | 0.28 |
| Material response to non-hydrometeor weathering stressors (e.g., UV radiation, icing, thermal expansion, aerosols (incl. dust)) | 0.64 | 0.23 | 0.36 | 0.32 | 0.35 | 0.24 |
| **Theme 4: Aerodynamic implications of LEE** | Mean | SD | Mean | SD | Mean | SD |
| Quantification of damage and surface roughness progression through time | 0.95 | 0.16 | 0.4 | 0.32 | 0.45 | 0.28 |
| Attribution of AEP loss to LEE (via effective surface roughness) | 0.88 | 0.23 | 0.35 | 0.34 | 0.5 | 0.24 |
| Attribution of AEP loss to application of LEP measures | 0.75 | 0.26 | 0.4 | 0.39 | 0.55 | 0.28 |
| Quantifying evolution of power curve through time (incl. post deployment) | 0.75 | 0.26 | 0.3 | 0.42 | 0.3 | 0.42 |
| Optimization of damage repair solution/timing | 0.9 | 0.21 | 0.35 | 0.34 | 0.5 | 0.33 |

Equally, there are processes/phenomena where understanding is lacking, but uncertainty in a process/phenomenon is not deemed to be a current primary limitation on TRLs for LEE solutions. Such a process/phenomenon might be deemed tier 2 for research effort. An example drawn from Theme 1 atmospheric drivers is non-hydrometeor stressors, which received a mean process/phenomena importance level rating of 0.55, and both measurement and modeling require improvement.

A high SD of rankings also conveys information about the divergence of opinions across the experts. An example from Theme 1 is the estimation of impingement efficiency as a function of the hydrometeor diameter [103]. The mean rating for importance was 0.55, but the variability around that was large (SD = 0.44). Thus, there is substantial variability in the opinions regarding whether the 'capture' of hydrometeors of different sizes by the blade leading edge is <1 for the hydrometeors of greatest importance to damage, and whether there is uncertainty in the D and $v_c$ dependence of impingement efficiency.

### 3. Discussion of Exemplar Research Activities Designed to Address Critical Research Needs Identified in the PIRT Process and Thus to Improve TRLs of LEE Solutions

*3.1. Phenomena/Processes Given Tier 1 Priority Within the Atmospheric Drivers Theme*

Two processes/phenomena within Theme 1 were identified as tier 1 priority: hydrometeor size distribution (HSD) <u>and</u> phase. The narratives supplied within the PIRT framework and past research suggest that although these are phenomena of importance, the knowledge or translation of knowledge to improve measurement/data analysis procedures or to modeling tools is insufficient. Materials stresses are demonstrably a function of the number and diameter of impinging hydrometeors. The HSD (and hydrometeor phase) is also a function of precipitation intensity and of temporal and spatial scale [104]. For example, an analyses of data from the US Southern Great Plains showed that 10% of 1 min precipitation rates exceeded 4.5 mmhr$^{-1}$, while the 90th percentile value for 10 min precipitation rates were <2.3 mmhr$^{-1}$ [14]. A study in Switzerland using automated hail sensors found that 75 % of local hailfalls lasted just a few minutes (from less than 4.4 min to less than 7.7 min, depending on a parameter to delineate the events) and that 75 % of the impacts occurred in less than 3.3 min to less than 4.7 min [105]. These findings imply not only a need for the robust assessments of precipitation rate, HSD, and phase but also that such data, whether from measurements or models, need to be available at high spatiotemporal resolution.

A range of technologies exist to measure the precipitation intensity (collectively referred to as rain gauges (RG)) [106] and HSD (i.e., instruments that measure hydrometeor number concentrations in size classes and are referred to as disdrometers) [14]. Some disdrometers also measure the fall velocity, phase, and sphericity (which is required to compute the hydrometeor mass and kinetic energy transfer) [14]. In the case of optical (or laser) disdrometers, the hydrometeor D is measured by the number of horizontal laser beams broken by the hydrometeor and the $v_f$ is derived from the duration of time that the beams are interrupted.

Assuming spherical droplets, the precipitation rate (*RR* in mmhr$^{-1}$) from a disdrometer is proportional to the sum of the number of size distributed hydrometeors (*n* in diameter (*D*) class *i* = 1 to *j*) as follows:

$$RR \propto \sum_{i=1}^{j} n_i D_i^3 \tag{3a}$$

or more explicitly for the OTT Parsivel$^2$ disdrometer (which has 32 diameter classes):

$$RR = \frac{\pi}{6} \frac{3.6}{10^3} \frac{1}{Ft} \sum_{i=1}^{32} n_i D_i^3 \tag{3b}$$

where *F* is the instrument 'field of view', and *t* is the duration of time during which the hydrometeor counts are made.

The implication of Equation (3a,b) is that small errors in hydrometeor diameter can yield large errors in RR. Hence, if the precipitation rate is to be derived from disdrometers, the accurate assessment of the hydrometer diameter is a necessary pre-requisite, but the axis ratio (the ratio of the vertical dimension of the hydrometeor to the horizontal dimension) for liquid hydrometeors is generally <1 and scales with the horizontal dimension [94,107]. Most disdrometers report RR computed by integrating overall hydrometeor diameters and fall velocities using proprietary software which includes correction factors, e.g., for the axis ratio of hydrometeors that are not fully specified.

When the accumulated depth of precipitation (or precipitation intensity) from disdrometers is compared with tipping or weighing rain gauges that measure only the mass or depth of water accumulated over a time interval, incomplete closure is achieved [108]. Thus, even if the first-order models of nominal erosion rates (such as those described above) are employed, the source of the precipitation data are a major source of uncertainty in lifetime estimates. For example, data were being collected at the Wind Energy Institute of Canada (WEICan) wind farm in Prince Edward Island, Canada, using an OTT Parsivel$^2$ optical disdrometer and an unheated Campbell Scientific TE525 Tipping Bucket Rain Gauge (RG) (Figure 4a). Because the RG was unheated, in the following, we selected only data

collected during the summer months to avoid periods with snowfall. Hourly summer-time accumulated precipitation from the disdrometer was consistently lower than that from an RG across a wide range of precipitation rates and wind regimes (Figure 4b,c). Although the disdrometer was more likely to report non-zero precipitation (even when the threshold to detect precipitation was set to that determined by the tip volume of the rain gauge, Figure 4d), of particular importance to LEE, the RG at WEICan exhibited twice the frequency of occurrence of precipitation rates > 10 mm/hr. When conditionally sampled to select periods when both sensors exhibited non-zero precipitation, the probability of extreme precipitation being reported by the RG was also higher than that from the disdrometer (Figure 4c).
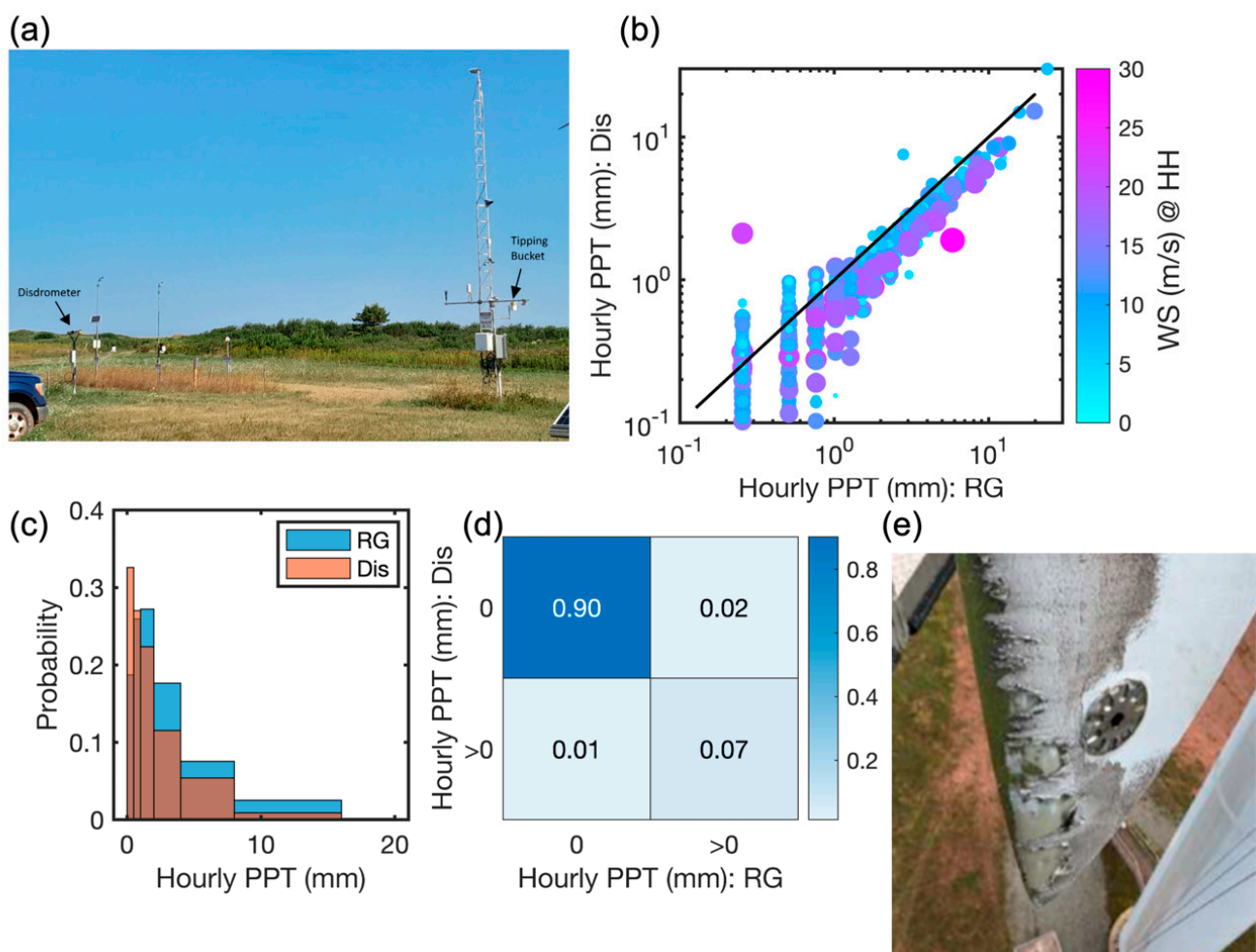


**Figure 4.** (**a**) Precipitation sensors deployed at WEICan. (**b**) Scatterplot of hourly precipitation (PPT) from the rain gauge (RG) and OTT disdrometer (Dis) for data collected during May–October of 2022 and 2023. Symbols scale with, and are colored by, prevailing wind speed at wind turbine hub-height (HH). (**c**) Histograms of hourly precipitation for all hours when both sensors report non-zero precipitation. (**d**) Heatmap of the joint probability of no precipitation (defined using a threshold of 0.126 mm, i.e., minimum reported by the RG) from RG and Dis. As shown, 7% of hours exhibited precipitation of >0.126 mm from both sensors. (**e**) Example photograph of leading-edge erosion on one of the wind turbines operating at WEICan.

More mechanistic models of material stress and erosion include information regarding HSD (i.e., the concentration of hydrometeors of given diameters, $D_i$) which can be derived

from the disdrometer measurements of the number counts ($n(i,v)$) in diameter ($i$) and fall velocity ($v_f$) classes:

$$N(D_i) = \sum_{v=1}^{x} \frac{n(i,v)}{Ftv_f(i,v)\Delta D_i} \tag{4}$$

where $x$ is the number of fall velocity classes and $\Delta D_i$ is the width of each diameter class, $i$. The implication of Equation (4) is that small errors in either hydrometer $D$ or fall velocity can yield substantial errors in the derived HSD (i.e., the expression of number concentrations as a function of hydrometeor diameter). However, measured HSD also differ across different disdrometers, and standardized data processing procedures are lacking [14,94,109]. Further, there is evidence that the relative performance of different disdrometers is a function of the prevailing climate [14]. Accordingly, when measurements from the three most commonly used disdrometers types (optical, impact, and video) were used to compute accumulated kinetic energy of transfer from hydrometeor impacts to wind turbine blades at an example site in the US Southern Great Plains, the results differed by 38% [94]. The results differed by 100% when different data analysis protocols that vary in terms of the permitted range of fall velocities regarding hydrometeor asymmetry were applied to a single disdrometer [94]. Also, even excluding effects from hydrometeor hardness, hail may be substantially more erosive than rain due to the higher diameters of these hydrometeors. Many disdrometers use proprietary empirical functions to indicate the possible presence of hail based on hydrometeor diameter and/or fall velocity rather than directly detecting it.

Research to reduce uncertainty in HSD/$v_f$/sphericity (axis ratio)/phase, and ultimately to provide best practice for measurements at prospective or operating wind farms is ongoing. This includes an experiment performed at an airport in upstate New York in which two identical OTT Parsivel$^2$ optical disdrometers were deployed close to a highly maintained Mesotech heated tipping bucket RG (part number 29000503) deployed as part of the Automated Weather Observing System operated by the US Federal Aviation Administration. The experiment ran from June to September 2024, inclusive (154 days of 1 min observations), and focused on summer months to avoid snowfall periods. It was designed to test whether the presence of large diameter hydrometeors reported at $v_f < v_t$ (where $v_t$ is the terminal fall velocity) for that $D$ [110] was due to horizontal advection of the droplets during high wind events. Accordingly, one of the disdrometers was deployed with a windshield and the other without as typified by the current deployments at operating wind farms (Figure 5a). In contrast to the data being collected at WEICan (Figure 4), good achievement was found between hourly precipitation intensity from the RG and disdrometers across the entire dynamic range of the precipitation intensities (Figure 5b). Across the range of observed wind speeds (0–12 ms$^{-1}$) and wind gusts (0–18 ms$^{-1}$) measured using a sonic anemometer deployed at 10 m AGL, the two disdrometers exhibited a high degree of agreement in terms of the detection of precipitation (Figure 5d) and the amount of precipitation (Figure 5b), and there was no evidence that the degree of agreement between the disdrometers and the RG scales with wind intensity (Figure 5b). This experiment did not suggest that the wind shielding of disdrometers greatly reduces the frequency of occurrence of hydrometeors falling with $v_f < v_t$ (Figure 5c), or greatly improves agreement with precipitation rates sampled with an RG (Figure 5b).
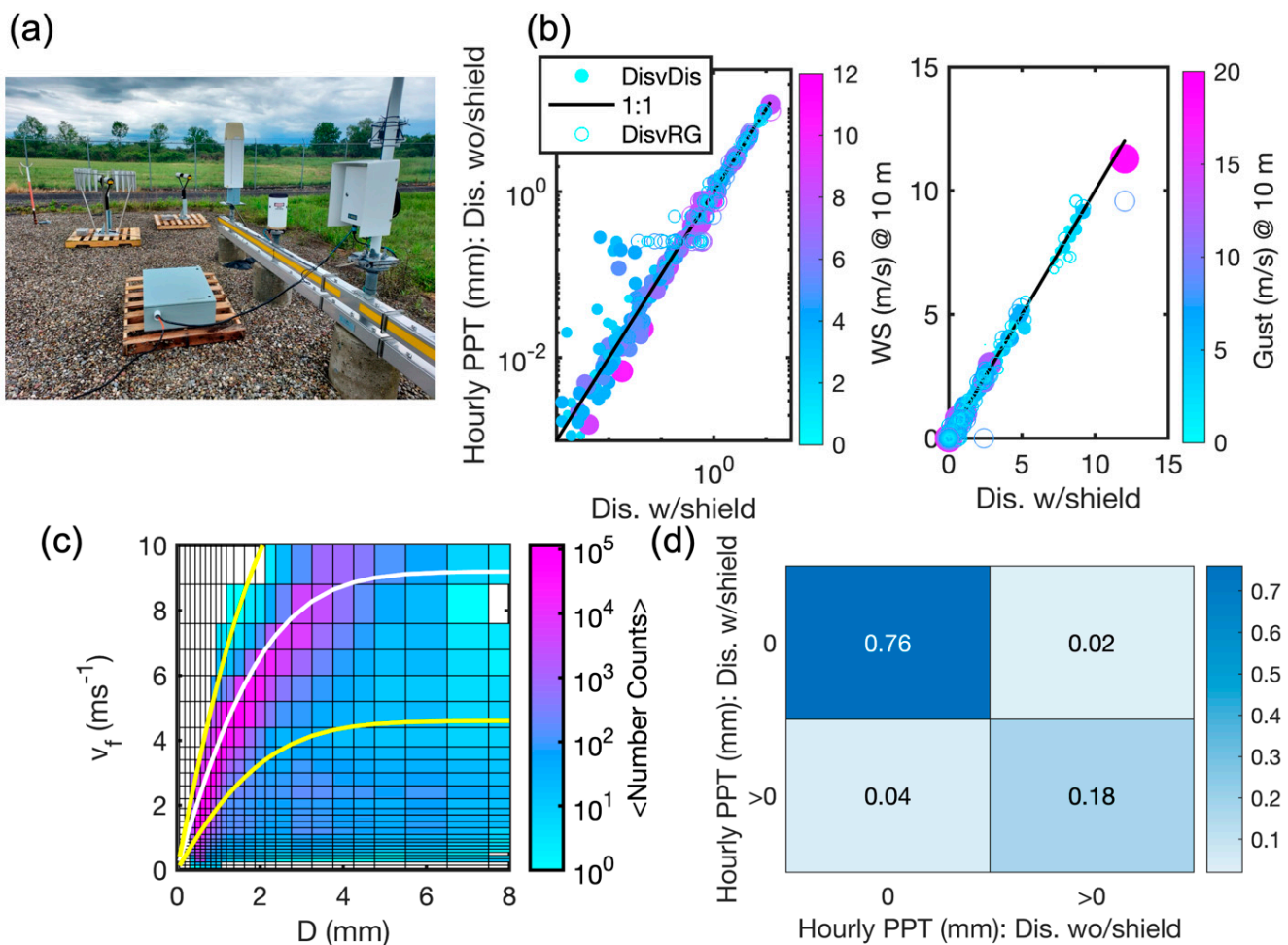
**Figure 5.** (**a**) Instruments deployed in upstate New York. (**b**) Scatterplot of hourly precipitation (PPT) from the disdrometer operated without the wind shield (Dis wo/shield) versus the disdrometer with the wind shield (Dis w/shield) (filled symbols) and the rain gauge (RG) (open symbols) on logarithmic and linear axes. Symbols are scaled with, and colored by, the prevailing wind speed at 10 m AGL (left-hand panel) and by the fastest wind gust (right panel). (**c**) Joint probability of hydrometeor diameter (D) and fall velocity ($v_f$) from Dis w/shield. White line indicates terminal fall velocity ($v_t$) as a function of D from Gunn and Kinser [110]. Yellow lines show the $\pm50\%$ bounds on $v_t$ that may indicate erroneous observations [111]. (**d**) Heatmap of the joint probability of no precipitation or precipitation from the two disdrometers.

There remains an urgent need for a comprehensive instrument inter-comparison experiment, openness from instrument manufacturers regarding hardware settings, and the development of best practice for instrument deployment and data processing to enhance the TRL for the prediction of long-term LEE and the nowcasting of erosive events for erosion-safe mode of implementation.

NWP models are sophisticated and skillful tools for weather forecasting and climate projections. However, simulated precipitation occurrence and intensity remain less skillful than other atmospheric properties and are highly dependent on model grid [112]. The PIRT analysis also identified the need for improvements in the numerical simulation of precipitation and HSD. These issues have long been recognized within the atmospheric science modeling community [113] and there are many parameterizations available to represent cloud, precipitation, and convection processes from scales of millimeters to kilometers, which can yield very different precipitation rates (see example in Figure 6). Most NWP models use bulk microphysics schemes and employ gamma distributions for cloud and hydrometeor distributions [114–118]. Binned (or classed) microphysics schemes

resolve the HSD at higher computational cost and improved flexibility [119], but different schemes yield widely varying hydrometeor characteristics [120] and they do not always out-perform bulk schemes in terms of the fidelity of RR [121]. Most modeling studies post-process simulated RR using empirical relationships between near-surface HSD and simulated RR [122]. Simulated hail production is also very sensitive to the pre-existing aerosol, frozen hydrometer density, and other factors influencing hydrometer diameters and fall velocities [123]. The land surface scheme employed and soil moisture used to initialize numerical simulations also influence precipitation simulation fidelity [124].
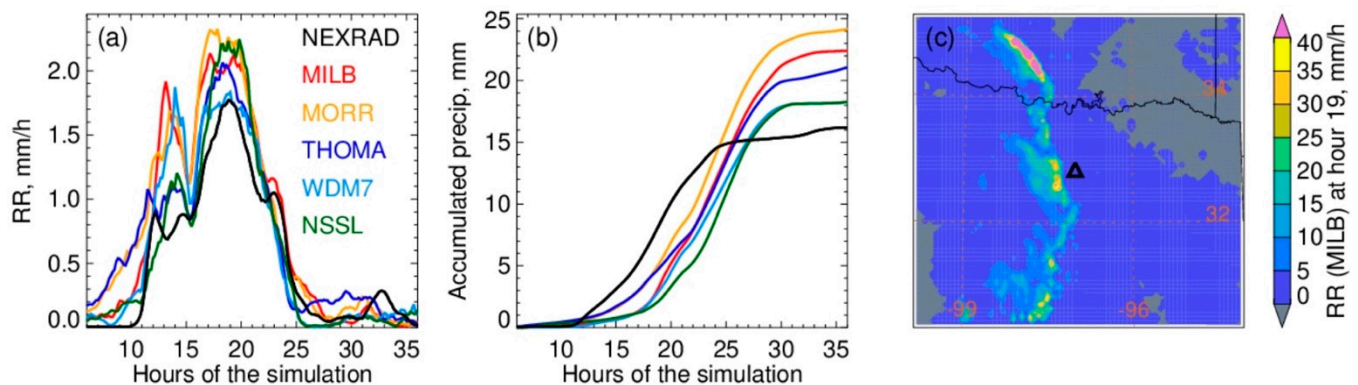


**Figure 6.** Spatial average. (**a**) Precipitation rate and (**b**) accumulated precipitation from WRF simulations (dx = 1 km) of an intense precipitation event during March 2017 over a region with many wind turbine assets [125]. The simulation [126] is performed in a short-term forecasting mode as would be used for predicting the need for erosion safe-mode operation of wind turbines. Time series denote simulations with five different microphysics schemes: Milbrandt–Yau (MILB), Morrison (MORR), Thompson aerosol aware (THOMA), WRF double-moment seven class (WDM7), and NSSL, plus RADAR (NEXRAD) observations. (**c**) The domain over which the spatial averaging is performed. Black triangle indicates Dallas Fort Worth, black lines denote the state boundaries of Texas, Oklahoma, and Arkansas.

It has been previously shown that WRF exhibits some skill for forecasting heavy precipitation and hail and the occurrence of high wind speeds, but the joint occurrence of heavy precipitation and high wind speeds and the simulation of hail diameter continue to lack the fidelity necessary to make integrative robust assessments of erosion potential or short-term forecasts of highly erosive events for erosion safe-mode operation [75,76].

The improved representation of hydroclimatic conditions with numerical models, the scoping of uncertainty, and fundamental model improvements are a focus of multiple initiatives within the atmospheric science community including the World Climate Research Programme Global Precipitation Experiment lighthouse activity [127]. Machine learning climate emulators are also being developed that seek to bridge the gap between the scales resolved by NWP models and precipitation at the local level [128]. Leveraging such initiatives can, and will, benefit the wind energy industry and enhance TRLs of LEE mitigation options. However, the specific need for model and measurement fidelity for precipitation rates and HSD particularly at high wind speeds is, to some degree, specific to the wind energy community. Effort should be invested in a detailed NWP verification and validation (V&V) framework that is specifically focused on the requirements of the wind energy community to advance the TRL for model-based prediction of LEE meteorological drivers. This is a focus of the understanding atmospheric impacts on wind turbines for better efficiency (AIRE) project (https://aire-project.eu, e.g., accessed on 10 August 2024).

*3.2. Phenomena/Processes Given Tier 1 Priority Within the Damage Detection and Quantification Theme*

This PIRT process resulted in one phenomenon/process being given tier 1 priority within the damage detection and quantification theme: translating water impingement to

material loss/stress (e.g., metrics: kinetic energy, Springer–ADF, VN curves). Although this topic could legitimately be included under Theme 3—material response, the specific theme under which it was listed is likely not a critical determinant of the PIRT rating. As described above, computing the accumulated kinetic energy (AKE) of collisions between falling hydrometeors and rotating blades through time is trivial presuming adequate data regarding the hydrometeors and hub-height wind speed are available at high time resolution. However, AKE does not directly translate to material damage.

Springer's model uses the material properties of the blade and coating and the hydrometeor impact number, diameter, velocity, and impact angle to estimate a distance to failure or the end of the incubation period for coating wear for each hydrometeor diameter that combined with Miner's rule is used to estimate ADF [94]. However, Springer's model is not very mechanistically defined and the parameter estimates are highly uncertain [66].

As described above, many RET experiments are confined to a fairly narrow range of droplet sizes and can generate only liquid droplets. However, actual precipitation comprises an ensemble of multiple hydrometeor diameters. A recommended practice from DNV [129] considers only one droplet diameter ($D$ = 2.38 mm) that naturally will not reflect the range of observed hydrometeors. Indeed, based on data from the US Southern Great Plains, where deep convection and intense precipitation is relatively common [14], the mass-weight hydrometeor mean diameter was $\geq$2.38 mm during only 6% of 1 min precipitation periods. Further, to achieve damage results in a reasonable time (i.e., to accelerate erosion), RETs are operated at higher closing velocities than is representative of real operating conditions. The resulting VN curves are then extrapolated to derive estimates at lower $v_c$ of the number of impacts at a given diameter that would yield damage. Testing viscoelastic coatings at very high closing velocities may result in rain erosion testers underestimating coating or LEP durability because wind turbines frequently operate at lower tip speeds. A comprehensive rain erosion test with multiple droplet sizes underlines the need for further research on the derivation of the VN curves from RETs [130]. More detail is given in Section 3.3.

Other phenomena/processes in the damage detection theme that are characterized as tier 2 priority for research relate to the accuracy of damage estimates. The use of drones and robots for blade inspection is becoming more routine, particularly for larger wind turbines and offshore wind farms and potentially decreases costs/time/risk of injury to technicians [131]. The full automation of damage detection data derived using such tools is leveraging advanced machine learning (ML) image processing tools [62,132]. Further innovations in this field include the construction of digital twins using high-resolution topographic leading-edge roughness (LER) data from operating/decommissioned blades that can be analyzed aerodynamically using 3D computational fluid dynamics (CFD) or wind tunnels [133].

Efforts to commercialize damage detection solutions are ongoing (e.g., using thermal imaging [134], laser profilometry [135], or gloss measurement [136]) implying relatively high TRLs, even as research is being conducted to evaluate efficacy as a function of damage severity and extent [137].

### 3.3. Phenomena/Processes Given Tier 1 Priority Within the Material Response Theme

This PIRT analysis identified two phenomena within Theme 3, material response as tier 1 priority for research that links to the usefulness of RETs, and specifically their representation of atmospheric conditions including the hydrometeors phase (e.g., rain and hail), size distributions and collision velocities [12], and whether accelerated lab tests represent the pre-stressing of blade materials that enhances hydrometeor erosion of the leading edge [138]. These concerns also link to the second tier 1 research priority: methodologies to translate lab experimental data (incl. rain erosion testers) to field conditions and failure modes (see Section 3.2).

Important new research is testing multiple key aspects of the translation of RET to real-world conditions. For example, RETs tend to operate with the continuous bombardment

of droplets, while in the real-world precipitation it is discontinuous. Experiments with a pulsating jet erosion tester have evolved evidence that the duration of time between precipitation events may play a role in dictating the number of droplet impacts required to reach the end of the incubation time [139]. Recent RET tests performed with and without UV exposure have found that UV weathering reduced the LEE coating life by about 30%, which greatly influenced the resulting VN curve parameters [140].

Experimental technologies have an important role in projecting damage emergence and progression, but mechanistically sound numerical models can permit more diagnostic analyses and sampling across a broader spectrum of conditions. An important source of uncertainty in such numerical models is that the precise composition of LEPs and/or coating is proprietary. In addition, the temperature and strain rate sensitivity of the flow stress are either ignored in modeling or at best implemented with empirical constitutive equations. This may lead to significant deviations from reality considering the adiabatic nature of hydrometeor impacts deforming surface layers at relatively high strain rates [141].

More sophisticated and explicit models such as finite element (FE) models of multiple liquid impact on multilayered viscoelastic materials take into account microscale material structure and porosity [84,142] and are preferable to empirical or semi-empirical models. However, they are relatively computationally demanding and require information regarding a range of material properties and behaviors that can be difficult to acquire. The computational cost is amplified if all possible combinations of hydrometeor D and $v_c$ are to be included in coating lifetime estimations. Thus, an emerging area of research is the construction of ML emulators conditioned using the output from numerically sophisticated models but taking the form of considerably faster closed-form architectures [143]. Such emulators can be used to more rapidly and efficiently evaluate the uncertainty space. An example is the incorporation of an ML model trained by the output of FE simulations of the spatial and temporal evolution of the stress field in the coating for various impact speeds and hydrometeor diameters (see the schematic in Figure 7). To illustrate this potential, a surrogate model based on a neural network was trained to make predictions for the peak stresses in the coating layer. A relatively small number of FE simulations was used to generate training data for droplet diameters (*D*) of 0.5 to 4 mm, and impact speeds ($v_c$) between 80 and 90 ms$^{-1}$. A neural network surrogate model was trained to predict peak von Mises stresses at each point in the coating as a function of *D* and $v_c$. An independent set of FE simulations was used to evaluate the surrogate model predictions (Figure 8). The ML predictions capture the topology of the peak stress contour, but the peak values show an error of ~10% relative to independent FE simulations. Building a larger suite of training simulations would likely aid in building a more robust surrogate model.

In principle, the workflow shown in Figure 7 could be expanded such that wind speed, rain intensity, and HSDs measured or modeled for any location can be combined with the surrogate model to obtain coating stresses for all possible combinations of impact parameters in an analogous manner to their use with the Springer model. The properties of the coating material could also be used as input to the machine learning model, and in principle this workflow can be extended to estimate not only the lifetimes of coatings, but also the levels of surface damage for estimating AEP losses.

While the use of ML-based surrogate models shows great promise, the response of viscoelastic polyurethane-based coatings depends on the loading rate, temperature, and the level of experienced strain. A more thorough experimental characterization of these materials is required, which includes high- and low-rate uniaxial data for wide strain ranges, dynamic mechanical analysis, cyclic loading–reloading, and volumetric strain measurements. Data from RET experiments can aid in determining parameters related to the fatigue behavior of coatings and to enhance the accuracy of predictions. Improvements in experimental procedures related to RET are therefore also highly valuable.
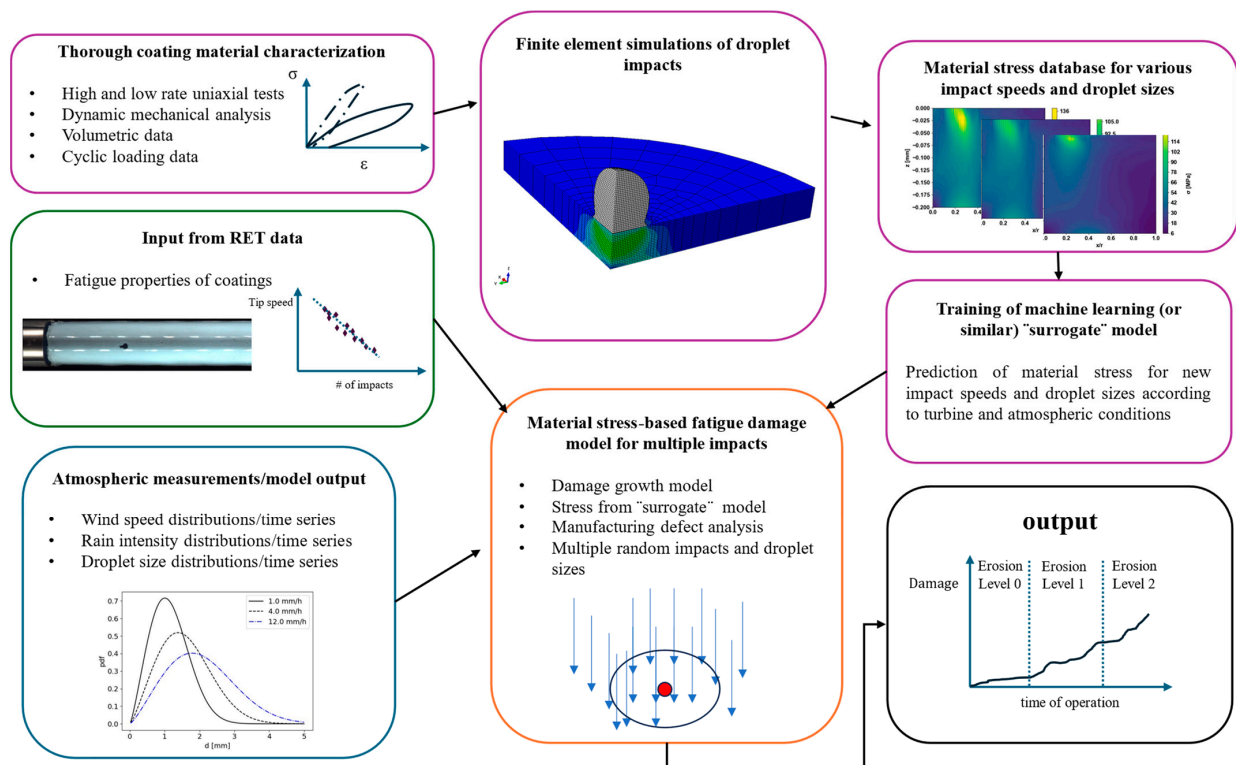
**Figure 7.** Schematic of a proposed combination of material testing and modeling; atmospheric measurements and lifetime modeling using a machine learning surrogate model. Arrows show information flow.
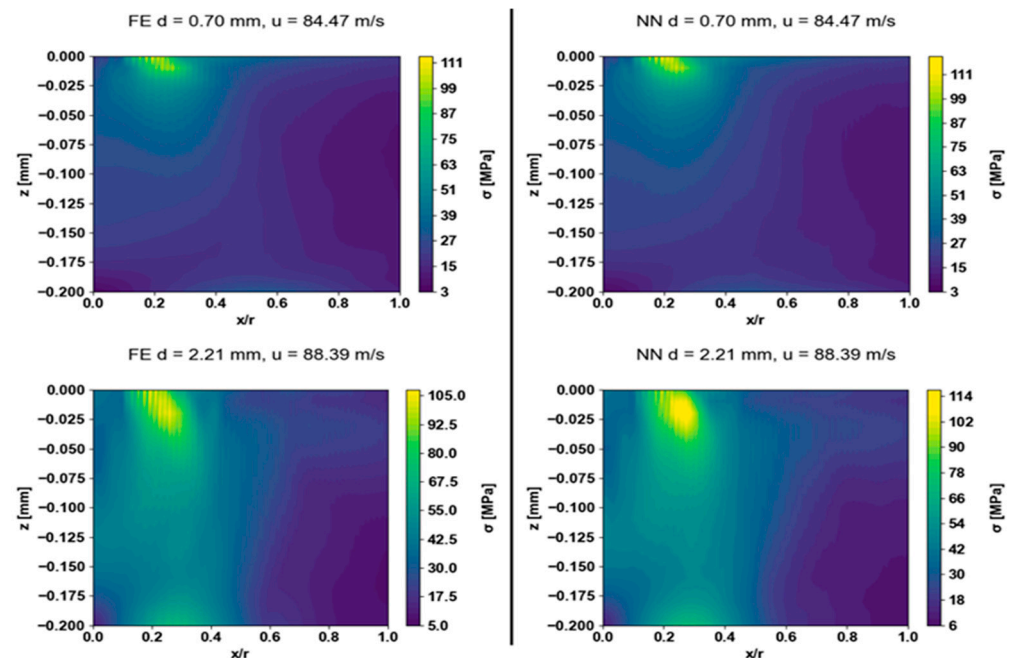


**Figure 8.** Comparison of peak von Mises stress (σ in MPa) contours over a cross section of the coating layer that spans from the top surface (z = 0) to the full layer thickness (z = 0.2 mm) and from the impact axis (x/r = 0) to a distance equal to the droplet radius r (x/r = 1) based on the finite element (FE) simulations, (**left**) and the predictions of the neural network surrogate model (NN) (**right**) for two different hydrometeor diameters (d) and closing velocities (u).

### 3.4. Phenomena/Processes Given Tier 1 Priority Within the Aerodynamics Theme

Finally, three phenomena/processes were identified as tier 1 priority in the aerodynamic implications theme: (a) Quantification of damage and surface roughness progression through time. This links strongly to Theme 2—damage detection. (b) Attribution of AEP loss to LEE (via effective surface roughness). (c) Optimization of damage repair solution/timing.

The quantification of wind turbine power and AEP losses due to LEE typically relies on blade force coefficient data obtained with wind tunnel testing or simulations with computational fluid dynamics (CFD) models [144,145]. In both cases, the geometry of damage and corresponding surface roughness at any time between installation and leading-edge resurfacing are key to achieving reliable estimates of the blade performance degradation. For moderate to intermediate LEE, which typically corresponds to damage of the thin external protection system of the leading edge (e.g., coating), the effects of roughness can be modeled by the means of the equivalent sand grain roughness [146]. The equivalent roughness height, yielding the same wall shear stress as that achieved with the observed roughness, can be obtained by using geometry, experimental data, or very high-fidelity CFD [147]. Their use for LEE applications, however, is associated with uncertainty, in part due to the difficulty of measuring blade roughness with sufficient resolution. One of the aims of the leading-edge roughness categorization (LERcat) efforts is to reduce this uncertainty [76]. When LEE becomes severe, with damage also to the leading-edge composite material, the sand grain model is no longer applicable, and the erosion geometry needs to be resolved [148]. The above highlights the importance of acquiring, with sufficient resolution, the depth and surface map of LEE and thus links to new innovations in damage characterization mentioned under Theme 2.

Once erosion topographies are acquired with adequate geometric resolution, ML can also play a key role in developing blade predictive maintenance frameworks by providing erosion aerodynamics and resulting AEP losses, as demonstrated with the AEP loss prediction system (ALPS) [144]. Determining the LEE-induced blade performance degradation for each erosion topography encountered in operation would require numerous lengthy CFD analyses and specialized expertise for each wind turbine assessment, a cost increased by the large number of turbines in a wind farm and the potentially high temporal frequency of these assessments in the wind farm lifetime. An initial (one-off) execution of many CFD simulations corresponding to many diverse erosion topographies can be used to train the fast ML metamodels that can be used to quickly determine blade force coefficients for AEP loss assessment. Preliminary work, shown in Figure 9 [144], has demonstrated the high reliability of fast ML metamodels for predicting lift coefficient ($c_l$) and drag coefficient ($c_d$) of eroded blade sections, allowing the ML models to be used for AEP loss assessment [148,149]. More development work is needed in this area to generalize these ML approaches, enable them to consider even wider LEE patterns observed in operation, and consider the variability of the nominal blade geometry among different wind turbine classes.

Optimizing the timing of blade leading-edge repair was identified as an important phenomena/process in the PIRT. The optimization of repair at any operating wind farm depends on factors such as wind turbine age, damage severity, cost of electricity, and accessibility. The considerations used by commercial wind farm owner/operators regarding repair decisions are usually considered proprietary and thus are held in confidence. Thus, information from WEICan is briefly presented below to illustrate the process by which repair decisions and LEP application were made and the results of those actions. WEICan owns and operates five 2 MW turbines on a coastal, high-wind site with turbines 1–4 being located on an escarpment and experiencing a very similar wind climate [150]. All wind turbines at WEICan have exhibited advanced levels of LEE since commissioning in 2013. WEICan have chosen to initiate repair measures prior to "moderate" or "severe" levels of erosion, and indeed before there was significant mass loss or clear detection via power curve degradation or acoustic tracking [151], due to factors such as the severity of the

winter climate which means the O&M window is relatively short, and the remote location means that access for more extensive O&M is challenging. The two main indications that trigger WEICan's decision to carry out a blade repair are as follows:

1. The rapid degradation of LEP. If an LEP product experiences significant peeling and bubbling within a year, it saves on repair expenses to replace it before the blade is completely exposed.
2. The first sign of visible fiberglass. The more fiberglass is eroded away, the more blade preparation work is required before repairs. With light erosion, only sanding and buffing of the surface is required before reapplying the LEP, which takes about half a day per blade. With moderate to heavy erosion, the blade must be sanded, built back into shape with additional fillers and fiberglass before reapplying the LEP product, which can take 1.5 days to 2 days per blade. Therefore, repairing blades at the first sign of visible fiberglass saves time and cost.
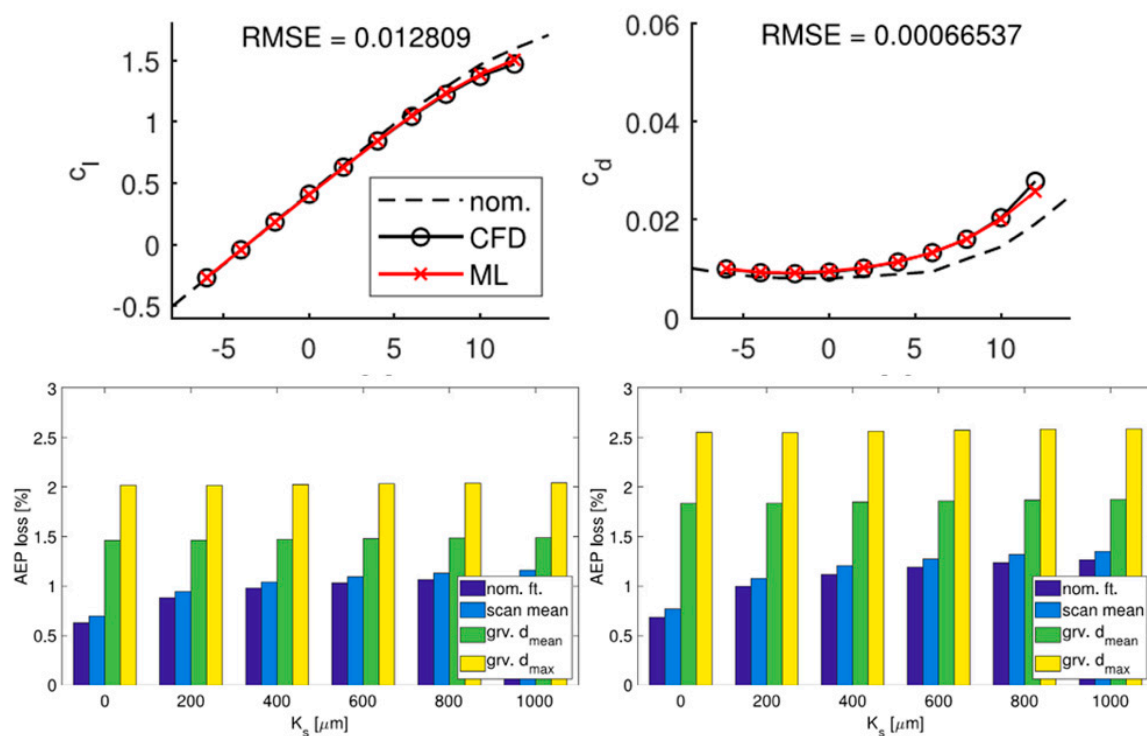


**Figure 9.** (**Top**): Eroded blade section force coefficients (lift ($C_l$) and drag ($C_d$)) for varying angles of attack (**bottom** axis) from geometry-resolving CFD ('CFD') and ML models ('ML') trained using the metadata of the erosion topography (curve labeled 'nom'. denotes nominal section performance curves) [126]. Bottom: offshore (**left**) and onshore (**right**) AEP losses for a multi-MW wind turbine derived using blade section force coefficients from ML models of type displayed in top plots for broad patterns and the extent of erosion topographies; '$K_s$' = equivalent sand grain roughness, 'nom/ft.' and 'scan mean' denote moderate to intermediate LEE severity, and 'grv. $d_{mean}$' and 'grv. $d_{max}$' denote severe LEE stages [148].

Initially, the blades on the wind turbines deployed at WEICan had no LEP, only standard polyurethane paint. In 2014, after LEE was observed visually, the blades were repaired, and standard polyurethane paint was reapplied. LEE was observed again in 2015. Since 2016, WEICan has engaged in the testing of five different LEPs, including paints, tapes, and shells. The first four LEPs were applied from 30 m to 45 m, while the fifth LEP was applied from 35 m to 45 m, measuring from the root of the blade. Each type of LEP has specific application instructions which typically require filling, sanding, and cleaning to achieve a smooth surface, and specific maximum and minimum temperatures and relative

humidities for curing and drying. Most of the wind turbine blade LEP materials have failed in one year to two years (Table 2, see example in Figure 4e), which LEP manufacturers generally have attributed to improper or inadequate surface preparation and installation. For example, the epoxies or adhesives were not appropriately activated, the surface was not adequately cleaned, the blade repairs with fillers or coatings ahead of installation were still curing, the conditions may have been appropriate at the start but were not sustained, or the skills of the technicians were not adequate. The original blade quality has also been identified as an important factor impacting LEP failure.

**Table 2.** Leading-edge protections used, dates applied, and damage and failures observed at WEICan.

| Type of LEP | Turbine | Year Applied, Year Reapplied | Year Damage Observed | Types of Damage Observed |
|---|---|---|---|---|
| Paint (2 component epoxy) | T1, T5 | 2016, 2017, 2019 | 2017, 2019, 2021 | Pitting, cracking, peeling, bubbling |
| Paint (polyurethane) | T4 | 2016, 2017, 2019 | 2017, 2019, 2021 | Pitting, peeling |
| Tape (2-component polyurethane) | T2 | 2016, 2017 | 2017, 2021 | Pitting, peeling, bubbling |
| Tape (2-component polyurethane) | T3 | 2016, 2019 | 2019, 2021 | Pitting, peeling, bubbling |
| Shell (polyurethane) | T1 | 2021, 2023 | 2023 | Peeling, bubbling |
| | T2 | 2022 | | |
| | T3 | 2022 | | |
| | T4 | 2021, 2022 | 2022 | Peeling, bubbling |
| | T5 | 2022 | | |

Current leading-edge repair work instructions have many requirements, including filling, sanding, and cleaning with maximum and minimum temperatures and relative humidities for curing and drying, as well as wind speed restrictions, depending on the method used to access the blade. This leads to small windows of time where repair is even possible and long and expensive repair times. TRLs would be enhanced by simplifying the repair process so that there are fewer restrictions, and it can be performed more quickly and economically.

A tier 2 priority in Theme 4 relates to the aerodynamic performance reductions due to LEP and their efficacy in slowing LEE. Data from the WEICan wind turbines was used in a decomposition analysis to remove effects due to prevailing meteorology (e.g., changes in the wind speed distribution before and after application) and isolate the impact of LEP on wind turbine performance. The results showed minimal to no improvements in performance due to LEP application and the resulting smoothing of the blade [151]. This is likely due to the high proportion of time that WEICan's wind turbines spend operating at rated power when AEP loss due to LEE is minimum, as well as the fact that WEICan repairs blades before any reduction in performance is observed.

Ultimately, decision-making with regard to LEE at WEICan relies on information from many of the tier 1 and tier 2 Themes: the existing and expected progression of damage, the resulting AEP reductions, and the impacts of LEP options. The uncertain durability of LEP options, perhaps resulting from unreliable LEP installation, has been the most substantial barrier to effective O&M planning for this site.

## 4. Concluding Remarks and Next Steps

The PIRT presented herein represents the first attempt to collate expert judgments on research priorities to enhance the TRL for solutions to reduce AEP (and revenue) losses and wind turbine operation and maintenance costs caused by wind turbine blade LEE. We used

a snowball sampling technique to identify possible respondents [81] and had a relatively small sample size ($n < 20$). Thus, the results must be considered preliminary. Nevertheless, the PIRT presented herein yields some important insights and lays the foundation for a comprehensive PIRT survey of wind energy experts that will be conducted during 2025 via the International Energy Agency Wind Energy (IEA) Technology Collaboration Programme (TCP) Task 46: Leading-Edge Erosion.

PIRT analyses are valuable because they allow the systematic identification of phenomena/processes of importance and that require further research to enhance TRLs or reduce safety risks. However, PIRT analyses are inherently subjective, since they leverage expert knowledge and judgment [82]. While some have advocated that PIRT methodologies should be based on literature-based meta-analyses [83], these too are not fully objective due to inherent biases in publishing [84]. An important advancement of this PIRT analysis is that the standard deviation of rankings across respondents is captured and presented to provide quantitative information about the presence or absence of consensus in the rankings. A divergence of opinions may derive from knowledge gaps due to the transdisciplinary nature of a topic or the rapidly evolving nature of a complex topic. Expert knowledge-based frameworks for research priority identification using PIRT may also not fully reflect emerging issues. An example of this that was identified in the PIRT but not given a tier 1 ranking is the possibility of micro-plastic shedding in the ocean environments. This research topic is being addressed in the PREventing MIcroplastics pollution in SEa water from offshore wind (PREMISE) project [152]. The emergence of such new topics strongly advocates for PIRT assessments to be continuously updated to ensure they evolve as knowledge is advanced.

The PIRT process and discussions summarized above indicate that the TRL for LEE solutions remains relatively low. However, investment in the priority areas articulated herein will enhance fundamental understanding and can be used to evolve a robust framework for end-to-end LEE prediction (Figure 7). Investments should be made in building a robust model V&V framework for each component of such a model chain [153]. Successful implementation of such a framework will require the sharing of a range of data from industrial partners. Needed information includes LEP product material properties, greater transparency regarding hardware settings in meteorological sensors, and data from operating wind farms linking the LEE state and the AEP. The end-to-end assessment of damage as a function of operating climate would also greatly benefit from sharing blade damage reports/images from operating wind farms for use in the evaluation of location-specific meteorologically driven LEE predictions [34]. Availability of time histories of wind turbine Supervisory Control and Data Acquisition (SCADA) data and adequately resolved LEE topographies for eroded blades will enable faster progress in blade predictive maintenance technologies.

**Data Availability Statement:** The PIRT results are summarized in Table 1. All other data can be provided upon request to the authors.

**Conflicts of Interest:** The authors declare no conflicts of interest.

## Nomenclature

| | |
|---|---|
| ADF | Accumulated Distance to Failure |
| AEP | Annual Energy (electricity) Production |
| AKE | Accumulated Kinetic Energy |
| CAPEX | CAPital EXpenditures |
| CFD | Computational Fluid Dynamics |
| D | Hydrometeor Diameter |
| Dis | Disdrometer |
| FE | Finite Element |
| HSD | Hydrometeor Size Distribution |
| IEA | International Energy Agency |
| LCoE | Levelized Cost of Energy |
| LEE | Leading-Edge Erosion |
| LEP | Leading-Edge Protection |
| LER | Leading-Edge Roughness |
| LERcat | Leading-Edge Roughness categorization |
| ML | Machine Learning |
| NWP | Numerical Weather Prediction |
| O&M | Operations and Maintenance |
| PIRT | Phenomena Identification and Ranking Tables |
| PPT | Precipitation |
| RET | Rain Erosion Tester |
| RG | Rain Gauge |
| RR | Precipitation (or Rain) Rate |
| SALT | Simplified Aerodynamic Loss Tool |
| SCADA | Supervisory Control and Data Acquisition |
| SD | Standard Deviation |
| TRL | Technology Readiness Level |
| UAV | Unmanned Aerial Vehicle |
| USA | United States of America |
| UV-A | Ultraviolet radiation at wavelengths ($\lambda$) = 320 and 400 nm |
| VN curves | Velocity–Number of impacts to failure |
| V&V | Verification and Validation |
| WARERs | Whirling Arm Rain ERosion testers |
| WRF | Weather Research and Forecasting |
| $v_c$ | Closing velocity |
| $v_f$ | Fall velocity |
| $v_t$ | Terminal fall velocity |

## References

1. Pryor, S.C.; Barthelmie, R.J.; Bukovsky, M.S.; Leung, L.R.; Sakaguchi, K. Climate change impacts on wind power generation. *Nat. Rev. Earth Environ.* **2020**, *1*, 627–643. [CrossRef]
2. Barthelmie, R.J.; Pryor, S.C. Climate Change Mitigation Potential of Wind Energy. *Climate* **2021**, *9*, 136. [CrossRef]
3. Gökgöz, F.; Güvercin, M.T. Energy security and renewable energy efficiency in EU. *Renew. Sustain. Energy Rev.* **2018**, *96*, 226–239. [CrossRef]
4. Borba, P.C.S.; Júnior, W.C.S.; Shadman, M.; Pfenninger, S. Enhancing drought resilience and energy security through complementing hydro by offshore wind power—The case of Brazil. *Energy Convers. Manag.* **2023**, *277*, 116616. [CrossRef]

5.  GWEC. *Global Wind Report 2024*; Global Wind Energy Council: Brussels, Belgium, 2024; p. 168. Available online: https://gwec.net/global-wind-report-2024/ (accessed on 20 October 2024).

6.  Lazard. Lazard's Levelized Cost of Energy Analysis—Version 16.0 [Online]. Zurich, Switzerland, 2023. Available online: https://www.lazard.com/research-insights/levelized-cost-of-energyplus/ (accessed on 10 July 2024).

7.  Bolinger, M.; Wiser, R.; O'Shaughnessy, E. Levelized cost-based learning analysis of utility-scale wind and solar in the United States. *Iscience* **2022**, *25*, 104378. [CrossRef]

8.  Barthelmie, R.J.; Larsen, G.C.; Pryor, S.C. Modeling Annual Electricity Production and Levelized Cost of Energy from the US East Coast Offshore Wind Energy Lease Areas. *Energies* **2023**, *16*, 4550. [CrossRef]

9.  Rinaldi, G.; Thies, P.R.; Johanning, L. Current status and future trends in the operation and maintenance of offshore wind turbines: A review. *Energies* **2021**, *14*, 2484. [CrossRef]

10. Du, Y.; Zhou, S.; Jing, X.; Peng, Y.; Wu, H.; Kwok, N. Damage detection techniques for wind turbine blades: A review. *Mech. Syst. Signal Process.* **2020**, *141*, 106445. [CrossRef]

11. Bech, J.I.; Hasager, C.B.; Bak, C. Extending the life of wind turbine blade leading edges by reducing the tip speed during extreme precipitation events. *Wind Energy Sci.* **2018**, *3*, 729–748. [CrossRef]

12. Bartolomé, L.; Teuwen, J. Prospective challenges in the experimentation of the rain erosion on the leading edge of wind turbine blades. *Wind Energy* **2019**, *22*, 140–151. [CrossRef]

13. Zhang, S.; Dam-Johansen, K.; Nørkjær, S.; Bernad, P.L., Jr.; Kiil, S. Erosion of wind turbine blade coatings–design and analysis of jet-based laboratory equipment for performance evaluation. *Prog. Org. Coat.* **2015**, *78*, 103–115. [CrossRef]

14. Pryor, S.C.; Barthelmie, R.J.; Cadence, J.; Dellwik, E.; Hasager, C.B.; Kral, S.T.; Reuder, J.; Rodgers, M.; Veraart, M. Atmospheric Drivers of Wind Turbine Blade Leading Edge Erosion: Review and Recommendations for Future Research. *Energies* **2022**, *15*, 8553. [CrossRef]

15. Sareen, A.; Sapre, C.A.; Selig, M.S. Effects of leading edge erosion on wind turbine blade performance. *Wind Energy* **2014**, *17*, 1531–1542. [CrossRef]

16. Mishnaevsky, L., Jr.; Hasager, C.B.; Bak, C.; Tilg, A.-M.; Bech, J.I.; Rad, S.D.; Fæster, S. Leading edge erosion of wind turbine blades: Understanding, prevention and protection. *Renew. Energy* **2021**, *169*, 953–969. [CrossRef]

17. Gaudern, N. A practical study of the aerodynamic impact of wind turbine blade leading edge erosion. *J. Phys. Conf. Ser.* **2014**, *524*, 012031. [CrossRef]

18. Froese, M. Wind-farm owners can now detect leading-edge erosion from data alone. *Wind. Eng. Dev.* **2018**, *14*. Available online: https://www.windpowerengineering.com/wind-farm-owners-can-now-detect-leading-edge-erosion-from-data-alone/ (accessed on 10 October 2024).

19. Campobasso, M.S.; Castorrini, A.; Ortolani, A.; Minisci, E. Probabilistic analysis of wind turbine performance degradation due to blade erosion accounting for uncertainty of damage geometry. *Renew. Sustain. Energy Rev.* **2023**, *178*, 113254. [CrossRef]

20. Herring, R.; Dyer, K.; Martin, F.; Ward, C. The increasing importance of leading edge erosion and a review of existing protection solutions. *Renew. Sustain. Energy Rev.* **2019**, *115*, 109382. [CrossRef]

21. Wiser, R.; Jenni, K.; Seel, J.; Baker, E.; Hand, M.; Lantz, E.; Smith, A. Expert elicitation survey on future wind energy costs. *Nat. Energy* **2016**, *1*, 16135. [CrossRef]

22. Mishnaevsky, L., Jr.; Thomsen, K. Costs of repair of wind turbine blades: Influence of technology aspects. *Wind Energy* **2020**, *23*, 2247–2255. [CrossRef]

23. Pryor, S.C.; Barthelmie, R.J.; Shepherd, T.J. Wind power production from very large offshore wind farms. *Joule* **2021**, *5*, 2663–2686. [CrossRef]

24. Maniaci, D.C.; Westergaard, C.; Hsieh, A.; Paquette, J.A. Uncertainty quantification of leading edge erosion impacts on wind turbine performance. *Proc. J. Phys. Conf. Ser.* **2020**, *1618*, 052082. [CrossRef]

25. Shankar Verma, A.; Jiang, Z.; Ren, Z.; Hu, W.; Teuwen, J.J. Effects of onshore and offshore environmental parameters on the leading edge erosion of wind turbine blades: A comparative study. *J. Offshore Mech. Arct. Eng.* **2021**, *143*, 042001. [CrossRef]

26. McMorland, J.; Flannigan, C.; Carroll, J.; Collu, M.; McMillan, D.; Leithead, W.; Coraddu, A. A review of operations and maintenance modelling with considerations for novel wind turbine concepts. *Renew. Sustain. Energy Rev.* **2022**, *165*, 112581. [CrossRef]

27. Zahle, F.; Barlas, T.; Lonbaek, K.; Bortolotti, P.; Zalkind, D.; Wang, L.; Labuschagne, C.; Sethuraman, L.; Barter, G. *Definition of the IEA Wind 22-Megawatt Offshore Reference Wind Turbine*; Technical University of Denmark (DTU): Lyngby, Denmark; National Renewable Energy Laboratory (NREL): Golden, CO, USA, 2024; 69p.

28. Shohag, M.A.S.; Hammel, E.C.; Olawale, D.O.; Okoli, O.I. Damage mitigation techniques in wind turbine blades: A review. *Wind Eng.* **2017**, *41*, 185–210. [CrossRef]

29. Mishnaevsky, L., Jr. Root causes and mechanisms of failure of wind turbine blades: Overview. *Materials* **2022**, *15*, 2959. [CrossRef]

30. Mankins, J.C. Technology Readiness Levels. 1995, p. 5. Available online: http://www.artemisinnovation.com/images/TRL_White_Paper_2004-Edited.pdf (accessed on 10 October 2024).

31. Mankins, J.C. Technology readiness assessments: A retrospective. *Acta Astronaut.* **2009**, *65*, 1216–1223. [CrossRef]

32. Keegan, M.H.; Nash, D.; Stack, M. On erosion issues associated with the leading edge of wind turbine blades. *J. Phys. D Appl. Phys.* **2013**, *46*, 383001. [CrossRef]

33. Letson, F.; Barthelmie, R.J.; Pryor, S.C. RADAR-derived precipitation climatology for wind turbine blade leading edge erosion. *Wind Energy Sci.* **2020**, *5*, 331–347. [CrossRef]

34. Visbech, J.; Göçmen, T.; Hasager, C.B.; Shkalov, H.; Handberg, M.; Nielsen, K.P. Introducing a data-driven approach to predict site-specific leading edge erosion. *Wind Energy Sci.* **2023**, *8*, 173–191. [CrossRef]

35. Preece, C.M. *Treatise on Materials Science and Technology*; Academic: Cambridge, MA, USA, 1979; Volume 16, p. 450.

36. Slot, H.; Gelinck, E.; Rentrop, C.; van der Heide, E. Leading edge erosion of coated wind turbine blades: Review of coating life models. *Renew. Energy* **2015**, *80*, 837–848. [CrossRef]

37. Zhu, X.; Fu, X.; Liu, L.; Xu, K.; Luo, G.; Zhao, Z.; Chen, W. Damage mechanism of composite laminates under multiple ice impacts at high velocity. *Int. J. Impact Eng.* **2022**, *168*, 104296. [CrossRef]

38. Heymsfield, A.; Szakáll, M.; Jost, A.; Giammanco, I.; Wright, R. A comprehensive observational study of graupel and hail terminal velocity, mass flux, and kinetic energy. *J. Atmos. Sci.* **2018**, *75*, 3861–3885. [CrossRef]

39. Macdonald, J.; Stack, M. Some thoughts on modelling hail impact on surfaces. *J. Bio-Tribo-Corros.* **2021**, *7*, 37. [CrossRef]

40. Kim, H.; Kedward, K.T. Modeling hail ice impacts and predicting impact damage initiation in composite structures. *AIAA J.* **2000**, *38*, 1278–1288. [CrossRef]

41. Savana, R. Effect of Hail Impact on Leading Edge Polyurethane Composites. TUDelft, 2022. Available online: http://repository.tudelft.nl/ (accessed on 10 October 2024).

42. Hannesdóttir, Á.; Kral, S.T.; Reuder, J.; Hasager, C.B. Rain erosion atlas for wind turbine blades based on ERA5 and NORA3 for Scandinavia. *Results Eng.* **2024**, *22*, 102010. [CrossRef]

43. Dolan, B.; Fuchs, B.; Rutledge, S.; Barnes, E.; Thompson, E. Primary modes of global drop size distributions. *J. Atmos. Sci.* **2018**, *75*, 1453–1476. [CrossRef]

44. Mayer, P.; Lubecki, M.; Stosiak, M.; Robakowska, M. Effects of surface preparation on the adhesion of UV-aged polyurethane coatings. *Int. J. Adhes. Adhes.* **2022**, *117*, 103183. [CrossRef]

45. Godfrey, M.; Siederer, O.; Zekonyte, J.; Barbaros, I.; Wood, R. The effect of temperature on the erosion of polyurethane coatings for wind turbine leading edge protection. *Wear* **2021**, *476*, 203720. [CrossRef]

46. Lachenal, X.; Daynes, S.; Weaver, P.M. Review of morphing concepts and materials for wind turbine blade applications. *Wind Energy* **2013**, *16*, 283–307. [CrossRef]

47. Wan, D.; Chen, S.; Li, D.; Zhen, Q.; Zhang, B. Sand-Laden Wind Erosion Pair Experimental Analysis of Aerodynamic Performance of the Wind Turbine Blades. *Energies* **2024**, *17*, 2279. [CrossRef]

48. Alajmi, A.F.; Ramulu, M. Characterization of the Leading-Edge Erosion of Wind Turbine Blades by Sand Particles Impingement. In *Proceedings of the ASME International Mechanical Engineering Congress and Exposition*; American Society of Mechanical Engineers: New York, NY, USA, 2021; p. V08BT08A033.

49. Vinnes, M.K.; Hearst, R.J. Aerodynamics of an airfoil with leading-edge icing. *Wind Energy* **2021**, *24*, 795–811. [CrossRef]

50. Rempel, L. Rotor blade leading edge erosion-real life experiences. *Wind Syst. Mag.* **2012**, *11*, 22–24.

51. Amirat, Y.; Benbouzid, M.E.H.; Al-Ahmar, E.; Bensaker, B.; Turri, S. A brief status on condition monitoring and fault diagnosis in wind energy conversion systems. *Renew. Sustain. Energy Rev.* **2009**, *13*, 2629–2636. [CrossRef]

52. Song, X.; Xing, Z.; Jia, Y.; Song, X.; Cai, C.; Zhang, Y.; Wang, Z.; Guo, J.; Li, Q. Review on the damage and fault diagnosis of wind turbine blades in the germination stage. *Energies* **2022**, *15*, 7492. [CrossRef]

53. Lopez, J.C.; Kolios, A. An autonomous decision-making agent for offshore wind turbine blades under leading edge erosion. *Renew. Energy* **2024**, *227*, 120525. [CrossRef]

54. Kong, K.; Dyer, K.; Payne, C.; Hamerton, I.; Weaver, P.M. Progress and trends in damage detection methods, maintenance, and data-driven monitoring of wind turbine blades–A review. *Renew. Energy Focus* **2023**, *44*, 390–412. [CrossRef]

55. Cao, Z.; Li, S.; Li, C.; Li, P.; Ko, T.J. Formation mechanism and detection and evaluation methods as well as repair technology of crack damage in fiber-reinforced composite wind turbine blade: A review. *Int. J. Adv. Manuf. Technol.* **2022**, *120*, 5649–5672. [CrossRef]

56. Yan, Y.; Cheng, L.; Wu, Z.; Yam, L. Development in vibration-based structural damage detection technique. *Mech. Syst. Signal Process.* **2007**, *21*, 2198–2211. [CrossRef]

57. Juengert, A.; Grosse, C.U. Inspection techniques for wind turbine blades using ultrasound and sound waves. In Proceedings of the Non-Destructive Testing in Civil Engineering: NDTCE, Nantes, France, 30 June–3 July 2009; p. 8.

58. Van Dam, J.; Bond, L.J. Acoustic emission monitoring of wind turbine blades. In *Proceedings of the Smart Materials and Nondestructive Evaluation for Energy Systems*; SPIE: San Diego, CA, USA, 2015; pp. 55–69.

59. Xu, D.; Wen, C.; Liu, J. Wind turbine blade surface inspection based on deep learning and UAV-taken images. *J. Renew. Sustain. Energy* **2019**, *11*, 053305. [CrossRef]

60. Sørensen, B.F.; Lading, L.; Sendrup, P. *Fundamentals for Remote Structural Health Monitoring of Wind Turbine Blades-a Pre-Project*; Report # RISO-R-1336(EN); Risoe National Laboratory: Roskilde, Denmark, 2002; p. 37. Available online: https://www.osti.gov/etdeweb/biblio/20273791 (accessed on 10 October 2024).

61. Shihavuddin, A.; Chen, X.; Fedorov, V.; Nymark Christensen, A.; Andre Brogaard Riis, N.; Branner, K.; Bjorholm Dahl, A.; Reinhold Paulsen, R. Wind turbine surface damage detection by deep learning aided drone inspection analysis. *Energies* **2019**, *12*, 676. [CrossRef]

62. Aird, J.A.; Barthelmie, R.J.; Pryor, S.C. Automated Quantification of Wind Turbine Blade Leading Edge Erosion from Field Images. *Energies* **2023**, *16*, 2820. [CrossRef]
63. Mishnaevsky, L.; Branner, K.; Petersen, H.; Beauson, J.; McGugan, M.; Sørensen, B. Materials for wind turbine blades: An overview. *Materials* **2017**, *10*, 1285. [CrossRef] [PubMed]
64. Brøndsted, P.; Lilholt, H.; Lystrup, A. Composite materials for wind power turbine blades. *Annu. Rev. Mater. Res.* **2005**, *35*, 505–538. [CrossRef]
65. Fæster, S.; Johansen, N.F.J.; Mishnaevsky, L., Jr.; Kusano, Y.; Bech, J.I.; Madsen, M.B. Rain erosion of wind turbine blades and the effect of air bubbles in the coatings. *Wind Energy* **2021**, *24*, 1071–1082. [CrossRef]
66. Hoksbergen, N.; Akkerman, R.; Baran, I. The Springer model for lifetime prediction of wind turbine blade leading edge protection systems: A review and sensitivity study. *Materials* **2022**, *15*, 1170. [CrossRef]
67. Cortés, E.; Sánchez, F.; O'Carroll, A.; Madramany, B.; Hardiman, M.; Young, T.M. On the Material Characterisation of Wind Turbine Blade Coatings: The Effect of Interphase Coating–Laminate Adhesion on Rain Erosion Performance. *Materials* **2017**, *10*, 1146. [CrossRef]
68. Eisenberg, D.; Laustsen, S.; Stege, J. Wind turbine blade coating leading edge rain erosion model: Development and validation. *Wind Energy* **2018**, *21*, 942–951. [CrossRef]
69. Traphan, D.; Herráez, I.; Meinlschmidt, P.; Schlüter, F.; Peinke, J.; Gülker, G. Remote surface damage detection on rotor blades of operating wind turbines by means of infrared thermography. *Wind Energy Sci.* **2018**, *3*, 639–650. [CrossRef]
70. Verma, A.S.; Castro, S.G.; Jiang, Z.; Teuwen, J.J. Numerical investigation of rain droplet impact on offshore wind turbine blades under different rainfall conditions: A parametric study. *Compos. Struct.* **2020**, *241*, 112096. [CrossRef]
71. Nash, D.; Leishman, G.; Mackie, C.; Dyer, K.; Yang, L. A staged approach to erosion analysis of wind turbine blade coatings. *Coatings* **2021**, *11*, 681. [CrossRef]
72. Castorrini, A.; Venturini, P.; Bonfiglioli, A. Generation of Surface Maps of Erosion Resistance for Wind Turbine Blades under Rain Flows. *Energies* **2022**, *15*, 5593. [CrossRef]
73. Springer, G.S. *Erosion by Liquid Impact*; John Wiley and Sons: New York, NY, USA, 1976; p. 278.
74. Springer, G.S.; Yang, C.-I.; Larsen, P.S. Analysis of rain erosion of coated materials. *J. Compos. Mater.* **1974**, *8*, 229–252. [CrossRef]
75. Herring, R.; Domenech, L.; Renau, J.; Šakalytė, A.; Ward, C.; Dyer, K.; Sánchez, F. Assessment of a wind turbine blade erosion lifetime prediction model with industrial protection materials and testing methods. *Coatings* **2021**, *11*, 767. [CrossRef]
76. Maniaci, D.C.; MacDonald, H.; Paquette, J.; Clarke, R. Leading Edge Erosion Classification System. Technical Report from IEA Wind Task 46 Erosion of Wind Turbine Blades. 2022, p. 52. Available online: https://iea-wind.org/task46/t46-results/ (accessed on 20 October 2024).
77. Panthi, K.; Iungo, G.V. Quantification of wind turbine energy loss due to leading-edge erosion through infrared-camera imaging, numerical simulations, and assessment against SCADA and meteorological data. *Wind Energy* **2023**, *26*, 266–282. [CrossRef]
78. Saenz, E.; Mendez, B.; Muñoz, A. Effect of erosion morphology on wind turbine production losses. *J. Phys. Conf. Ser.* **2022**, *2265*, 032059. [CrossRef]
79. Bak, C. A simple model to predict the energy loss due to leading edge roughness. *J. Phys. Conf. Ser.* **2022**, *2265*, 032038. [CrossRef]
80. Özçakmak, Ö.S.; Bretos, D.; Méndez, B.; Bak, C. Determination of annual energy production loss due to erosion on wind turbine blades. *J. Phys. Conf. Ser.* **2024**, *2767*, 022066. [CrossRef]
81. Gaertner, E.; Rinker, J.; Sethuraman, L.; Zahle, Z.; Anderson, B.; Barter, G.; Abbas, B.; Meng, F.; Bortolotti, F.; Skrzypinski, W.; et al. *Definition of the IEA 15-Megawatt Offshore Reference Wind Turbine*; NREL/TP-5000-75698; National Renewable Energy Laboratory: Golden, CO, USA, 2020. Available online: https://www.nrel.gov/docs/fy20osti/75698.pdf (accessed on 20 October 2024).
82. Malik, T.H.; Bak, C. Challenges in Detecting Wind Turbine Power Loss: The Effects of Blade Erosion, Turbulence and Time Averaging. *Wind Energy Sci. Discuss.* **2024**, *2024*, 1–23. [CrossRef]
83. Han, W.; Kim, J.; Kim, B. Effects of contamination and erosion at the leading edge of blade tip airfoils on the annual energy production of wind turbines. *Renew. Energy* **2018**, *115*, 817–823. [CrossRef]
84. Mishnaevsky, L., Jr.; Tempelis, A.; Kuthe, N.; Mahajan, P. Recent developments in the protection of wind turbine blades against leading edge erosion: Materials solutions and predictive modelling. *Renew. Energy* **2023**, 118966. [CrossRef]
85. Verma, A.S.; Yan, J.; Hu, W.; Jiang, Z.; Shi, W.; Teuwen, J.J. A review of impact loads on composite wind turbine blades: Impact threats and classification. *Renew. Sustain. Energy Rev.* **2023**, *178*, 113261. [CrossRef]
86. Dashtkar, A.; Johansen, N.F.-J.; Mishnaevsky, L., Jr.; Williams, N.A.; Hasan, S.W.; Wadi, V.S.; Silvello, A.; Hadavinia, H. Graphene/sol–gel modified polyurethane coating for wind turbine blade leading edge protection: Properties and performance. *Polym. Polym. Compos.* **2022**, *30*, 09673911221074197. [CrossRef]
87. Major, D.; Palacios, J.; Maughmer, M.; Schmitz, S. Aerodynamics of leading-edge protection tapes for wind turbine blades. *Wind Eng.* **2021**, *45*, 1296–1316. [CrossRef]
88. Kyle, R.; Wang, F.; Forbes, B. The effect of a leading edge erosion shield on the aerodynamic performance of a wind turbine blade. *Wind Energy* **2020**, *23*, 953–966. [CrossRef]
89. Bera, P.; Lakshmi, R.; Pathak, S.M.; Bonu, V.; Mishnaevsky, L., Jr.; Barshilia, H.C. Recent Progress in the Development and Evaluation of Rain and Solid Particle Erosion Resistant Coatings for Leading Edge Protection of Wind Turbine Blades. *Polym. Rev.* **2024**, *64*, 639–689. [CrossRef]

90. Jones, S.M.; Rehfeld, N.; Schreiner, C.; Dyer, K. The Development of a Novel Thin Film Test Method to Evaluate the Rain Erosion Resistance of Polyaspartate-Based Leading Edge Protection Coatings. *Coatings* **2023**, *13*, 1849. [CrossRef]

91. Verma, A.S.; Noi, S.D.; Ren, Z.; Jiang, Z.; Teuwen, J.J. Minimum leading edge protection application length to combat rain-induced erosion of wind turbine blades. *Energies* **2021**, *14*, 1629. [CrossRef]

92. Ansari, Q.M.; Sánchez, F.; Mishnaevsky, L., Jr.; Young, T.M. Evaluation of offshore wind turbine blades coating thickness effect on leading edge protection system subject to rain erosion. *Renew. Energy* **2024**, *226*, 120378. [CrossRef]

93. Katsivalis, I.; Chanteli, A.; Finnegan, W.; Young, T.M. Mechanical and interfacial characterisation of leading-edge protection materials for wind turbine blade applications. *Wind Energy* **2022**, *25*, 1758–1774. [CrossRef]

94. Letson, F.; Pryor, S.C. From Hydrometeor Size Distribution Measurements to Projections of Wind Turbine Blade Leading Edge Erosion. *Energies* **2023**, *5*, 3906. [CrossRef]

95. Skrzypiński, W.; Bech, J.; Hasager, C.B.; Tilg, A.; Bak, F.; Ch, V. Optimization of the erosion-safe operation of the IEA Wind 15 MW Reference Wind Turbine. *J. Phys. Conf. Ser.* **2020**, *1618*, 052034. [CrossRef]

96. Visbech, J.; Göçmen, T.; Réthoré, P.-E.; Hasager, C.B. Erosion-safe operation using double deep Q-learning. *J. Phys. Conf. Ser.* **2024**, *2767*, 032047. [CrossRef]

97. Oliver, T.J.; Nowlen, S.P. *A Phenomena Identification and Ranking Table (PIRT) Exercise for Nuclear Power Plant Fire Modeling Applications*; Report # NUREG/CR-6978; Sandia National Laboratory: Albuquerque, NM, USA, 2008; p. 441.

98. Singh, P.M.; Chan, K.J.; Deo, C.S.; Deodeshmukh, V.; Keiser, J.R.; Ren, W.; Sham, T.; Wilson, D.F.; Yoder, G.; Zhang, J. Phenomena Identification and Ranking Table (PIRT) study for metallic structural materials for advanced High-Temperature reactor. *Ann. Nucl. Energy* **2019**, *123*, 222–229. [CrossRef]

99. Maniaci, D.C.; Naughton, J.W. *V&V Integrated Program Planning for Wind Plant Performance*; Sandia National Lab. (SNL-NM): Albuquerque, NM, USA, 2019.

100. Klaas-Witt, T.; Emeis, S. The five main influencing factors for lidar errors in complex terrain. *Wind Energy Sci.* **2022**, *7*, 413–431. [CrossRef]

101. Wagner, R.; Pedersen, T.F.; Courtney, M.; Antoniou, I.; Davoust, S.; Rivera, R.L. Power curve measurement with a nacelle mounted lidar. *Wind Energy* **2014**, *17*, 1441–1453. [CrossRef]

102. Haupt, S.E.; Kosovic, B.; Shaw, W.; Berg, L.K.; Churchfield, M.; Cline, J.; Draxl, C.; Ennis, B.; Koo, E.; Kotamarthi, R. On bridging a modeling scale gap: Mesoscale to microscale coupling for wind energy. *Bull. Am. Meteorol. Soc.* **2019**, *100*, 2533–2550. [CrossRef]

103. Prieto, R.; Karlsson, T. A model to estimate the effect of variables causing erosion in wind turbine blades. *Wind Energy* **2021**, *24*, 1031–1044. [CrossRef]

104. Lochbihler, K.; Lenderink, G.; Siebesma, A.P. The spatial extent of rainfall events and its relation to precipitation scaling. *Geophys. Res. Lett.* **2017**, *44*, 8629–8636. [CrossRef]

105. Kopp, J.; Manzato, A.; Hering, A.; Germann, U.; Martius, O. How observations from automatic hail sensors in Switzerland shed light on local hailfall duration and compare with hailpads measurements. *Atmos. Meas. Tech.* **2023**, *16*, 3487–3503. [CrossRef]

106. Lanza, L.G.; Cauteruccio, A.; Stagnaro, M. Rain gauge measurements. In *Rainfall*; Elsevier: Amsterdam, The Netherlands, 2022; pp. 77–108.

107. Pruppacher, H.R.; Beard, K. A wind tunnel investigation of the internal circulation and shape of water drops falling at terminal velocity in air. *Q. J. R. Meteorol. Soc.* **1970**, *96*, 247–256. [CrossRef]

108. Ro, Y.; Chang, K.-H.; Hwang, H.; Kim, M.; Cha, J.-W.; Lee, C. Comparative study of rainfall measurement by optical disdrometer, tipping-bucket rain gauge, and weighing precipitation gauge. *Nat. Hazards* **2024**, *120*, 2829–2845. [CrossRef]

109. Méndez, B.; Saenz, E.; Pires, Ó.; Cantero, E.; Bech, J.; Polls, F.; Peinó, E.; Udina, M.; Garcia-Benadí, A. Experimental campaign for the characterization of precipitation in a complex terrain site using high resolution observations. *J. Phys. Conf. Ser.* **2024**, *2767*, 042016. [CrossRef]

110. Gunn, R.; Kinzer, G.D. The terminal velocity of fall for water droplets in stagnant air. *J. Atmos. Sci.* **1949**, *6*, 243–248. [CrossRef]

111. Tokay, A.; Petersen, W.A.; Gatlin, P.; Wingo, M. Comparison of raindrop size distribution measurements by collocated disdrometers. *J. Atmos. Ocean. Technol.* **2013**, *30*, 1672–1690. [CrossRef]

112. Prein, A.; Rasmussen, R.; Wang, D.; Giangrande, S. Sensitivity of organized convective storms to model grid spacing in current and future climates. *Philos. Trans. R. Soc. A* **2021**, *379*, 20190546. [CrossRef]

113. Fridlind, A.M.; Li, X.; Wu, D.; van Lier-Walqui, M.; Ackerman, A.S.; Tao, W.-K.; McFarquhar, G.M.; Wu, W.; Dong, X.; Wang, J. Derivation of aerosol profiles for MC3E convection studies and use in simulations of the 20 May squall line case. *Atmos. Chem. Phys.* **2017**, *17*, 5947–5972. [CrossRef]

114. Hong, S.-Y.; Dudhia, J.; Chen, S.-H. A revised approach to ice microphysical processes for the bulk parameterization of clouds and precipitation. *Mon. Weather Rev.* **2004**, *132*, 103–120. [CrossRef]

115. Morrison, H.; Curry, J.; Khvorostyanov, V. A new double-moment microphysics parameterization for application in cloud and climate models. *Part I Description. J. Atmos. Sci.* **2005**, *62*, 1665–1677.

116. Milbrandt, J.; Yau, M. A multimoment bulk microphysics parameterization. Part II: A proposed three-moment closure and scheme description. *J. Atmos. Sci.* **2005**, *62*, 3065–3081. [CrossRef]

117. Milbrandt, J.A.; Yau, M.K. A Multimoment Bulk Microphysics Parameterization. Part I: Analysis of the Role of the Spectral Shape Parameter. *J. Atmos. Sci.* **2005**, *62*, 3051–3064. [CrossRef]

118. Thompson, G.; Field, P.R.; Rasmussen, R.M.; Hall, W.D. Explicit forecasts of winter precipitation using an improved bulk microphysics scheme. Part II: Implementation of a new snow parameterization. *Mon. Weather Rev.* **2008**, *136*, 5095–5115. [CrossRef]

119. Khain, A.; Beheng, K.; Heymsfield, A.; Korolev, A.; Krichak, S.; Levin, Z.; Pinsky, M.; Phillips, V.; Prabhakaran, T.; Teller, A. Representation of microphysical processes in cloud-resolving models: Spectral (bin) microphysics versus bulk parameterization. *Rev. Geophys.* **2015**, *53*, 247–322. [CrossRef]

120. Xue, L.; Fan, J.; Lebo, Z.J.; Wu, W.; Morrison, H.; Grabowski, W.W.; Chu, X.; Geresdi, I.; North, K.; Stenz, R. Idealized simulations of a squall line from the MC3E field campaign applying three bin microphysics schemes: Dynamic and thermodynamic structure. *Mon. Weather Rev.* **2017**, *145*, 4789–4812. [CrossRef]

121. Fan, J.; Han, B.; Varble, A.; Morrison, H.; North, K.; Kollias, P.; Chen, B.; Dong, X.; Giangrande, S.E.; Khain, A. Cloud-resolving model intercomparison of an MC3E squall line case: Part I—Convective updrafts. *J. Geophys. Res. Atmos.* **2017**, *122*, 9351–9378. [CrossRef]

122. Yang, Q.; Zhang, S.; Dai, Q.; Zhuang, H. WRF Rainfall Modeling Post-Processing by Adaptive Parameterization of Raindrop Size Distribution: A Case Study on the United Kingdom. *Atmosphere* **2021**, *13*, 36. [CrossRef]

123. Shpund, J.; Khain, A.; Lynn, B.; Fan, J.; Han, B.; Ryzhkov, A.; Snyder, J.; Dudhia, J.; Gill, D. Simulating a Mesoscale Convective System Using WRF With a New Spectral Bin Microphysics: 1:Hail vs Graupel. *J. Geophys. Res. Atmos.* **2019**, *124*, 14072–14101. [CrossRef]

124. Collow, T.W.; Robock, A.; Wu, W. Influences of soil moisture and vegetation on convective precipitation forecasts over the United States Great Plains. *J. Geophys. Res. Atmos.* **2014**, *119*, 9338–9358. [CrossRef]

125. Pryor, S.C.; Letson, F.; Shepherd, T.J.; Barthelmie, R.J. Evaluation of WRF simulation of deep convection in the US Southern Great Plains. *J. Appl. Meteorol. Climatol.* **2023**, *62*, 41–62. [CrossRef]

126. Zhou, X.; Letson, F.; Crippa, P.; Pryor, S.C. Urban effect on precipitation and deep convective systems over Dallas-Fort Worth. *J. Geophys. Res. Atmos.* **2024**, *129*, e2023JD039972. [CrossRef]

127. Zeng, X.; Alves, L.; Boucher, M.-A.; Cherchi, A.; DeMott, C.; Dimri, A.; Gettelman, A.; Hanna, E.; Horinouchi, T.; Huang, J. Global Precipitation Experiment-A New World Climate Research Programme Lighthouse Activity. *Bull. Am. Meteorol. Soc.* **2024**. [CrossRef]

128. Yu, S.; Hannah, W.; Peng, L.; Lin, J.; Bhouri, M.A.; Gupta, R.; Lütjens, B.; Will, J.C.; Behrens, G.; Busecke, J. ClimSim: A large multi-scale dataset for hybrid physics-ML climate emulation. In Proceedings of the Advances in Neural Information Processing Systems 36 (NeurIPS 2023), New Orleans, LA, USA, 10–16 December 2023; p. 14.

129. DNVGL. DNV-RP-0171 Testing of Rotor Blade Erosion Protection Systems; 2018. Available online: https://www.dnv.com/energy/standards-guidelines/dnv-rp-0171-testing-of-rotor-blade-erosion-protection-systems/ (accessed on 20 October 2024).

130. Bech, J.I.; Johansen, N.F.-J.; Madsen, M.B.; Hannesdóttir, Á.; Hasager, C.B. Experimental study on the effect of drop size in rain erosion test and on lifetime prediction of wind turbine blades. *Renew. Energy* **2022**, *197*, 776–789. [CrossRef]

131. Márquez, F.P.G.; Chacón, A.M.P. A review of non-destructive testing on wind turbines blades. *Renew. Energy* **2020**, *161*, 998–1010. [CrossRef]

132. Rizk, P.; Rizk, F.; Karganroudi, S.S.; Ilinca, A.; Younes, R.; Khoder, J. Advanced wind turbine blade inspection with hyperspectral imaging and 3D convolutional neural networks for damage detection. *Energy AI* **2024**, *16*, 100366. [CrossRef]

133. Forsting, A.M.; Olsen, A.; Sørensen, N.; Fischer, A.; Markussen, C.; Bak, C. An aerodynamic digital twin of real-world leading edge erosion: Acquisition, Generation and 3D CFD. *J. Phys. Conf. Ser.* **2024**, *2767*, 022021. [CrossRef]

134. Hwang, S.; An, Y.-K.; Yang, J.; Sohn, H. Remote inspection of internal delamination in wind turbine blades using continuous line laser scanning thermography. *Int. J. Precis. Eng. Manuf.-Green Technol.* **2020**, *7*, 699–712. [CrossRef]

135. Ding, K.; Wu, C.; Luo, M.; Su, Z.; Ding, H.; Ye, Y.; Zhang, D. Surface Profile Inspection for Large Structures with Laser Scanning. *Surf. Topogr. Metrol. Prop.* **2024**, *12*, 035039. [CrossRef]

136. Leishman, G.; Nash, D.; Yang, L.; Dyer, K. A novel approach for wind turbine blade erosion characterization: An investigation using surface gloss measurement. *Coatings* **2022**, *12*, 928. [CrossRef]

137. Zhang, Y.; Avallone, F.; Watson, S. Leading edge erosion detection for a wind turbine blade using far-field aerodynamic noise. *Appl. Acoust.* **2023**, *207*, 109365. [CrossRef]

138. Pugh, K.; Rasool, G.; Stack, M.M. Raindrop erosion of composite materials: Some views on the effect of bending stress on erosion mechanisms. *J. Bio-Tribo-Corros.* **2019**, *5*, 45. [CrossRef]

139. Verma, A.S.; Wu, C.-Y.; Díaz, M.A.; Teuwen, J.J. Analyzing rain erosion using a Pulsating Jet Erosion Tester (PJET): Effect of droplet impact frequencies and dry intervals on incubation times. *Wear* **2024**, *562–563*, 205614. [CrossRef]

140. Castorrini, A.; Barnabei, V.F.; Domenech, L.; Šakalytė, A.; Sánchez, F.; Campobasso, M.S. Impact of meteorological data factors and material characterization method on the predictions of leading edge erosion of wind turbine blades. *Renew. Energy* **2024**, *227*, 120549. [CrossRef]

141. Hassani-Gangaraj, M.; Veysset, D.; Nelson, K.A.; Schuh, C.A. Melt-driven erosion in microparticle impact. *Nat. Commun.* **2018**, *9*, 5077. [CrossRef] [PubMed]

142. Tempelis, A.; Mishnaevsky, L., Jr. Surface roughness evolution of wind turbine blade subject to rain erosion. *Mater. Des.* **2023**, *231*, 112011. [CrossRef]

143. Reichert, P.; White, G.; Bayarri, M.J.; Pitman, E.B. Mechanism-based emulation of dynamic simulation models: Concept and application in hydrology. *Comput. Stat. Data Anal.* **2011**, *55*, 1638–1655. [CrossRef]

144. Cappugi, L.; Castorrini, A.; Bonfiglioli, A.; Minisci, E.; Campobasso, M.S. Machine learning-enabled prediction of wind turbine energy yield losses due to general blade leading edge erosion. *Energy Convers. Manag.* **2021**, *245*, 114567. [CrossRef]

145. Campobasso, M.S.; Castorrini, A.; Cappugi, L.; Bonfiglioli, A. Experimentally validated three-dimensional computational aerodynamics of wind turbine blade sections featuring leading edge erosion cavities. *Wind Energy* **2022**, *25*, 168–189. [CrossRef]

146. Nikuradse, J. *Laws of Flow in Rough Pipes*; Technical Memorandum NASA TM 1292; Lewis Research Center: Washington, DC, USA, 1950. Available online: https://digital.library.unt.edu/ark:/67531/metadc63009/m2/1/high_res_d/19930093938.pdf (accessed on 20 October 2024).

147. Kadivar, M.; Tormey, D.; McGranaghan, G. A review on turbulent flow over rough surfaces: Fundamentals and theories. *Int. J. Thermofluids* **2021**, *10*, 100077. [CrossRef]

148. Castorrini, A.; Ortolani, A.; Campobasso, M.S. Assessing the progression of wind turbine energy yield losses due to blade erosion by resolving damage geometries from lab tests and field observations. *Renew. Energy* **2023**, *218*, 119256. [CrossRef]

149. Castorrini, A.; Ortolani, A.; Minisci, E.; Campobasso, M. Opensource machine learning metamodels for assessing blade performance impairment due to general leading edge degradation. *J. Phys. Conf. Ser.* **2024**, *2767*, 052055. [CrossRef]

150. Barthelmie, R.J.; Doubrawa, P.; Wang, H.; Giroux, G.; Pryor, S.C. Effects of an escarpment on flow parameters of relevance to wind turbines. *Wind Energy* **2016**, *19*, 2271–2286. [CrossRef]

151. Latiffianti, E.; Ding, Y.; Sheng, S.; Williams, L.; Morshedizadeh, M.; Rodgers, M. Analysis of leading edge protection application on wind turbine performance through energy and power decomposition approaches. *Wind Energy* **2022**, *25*, 1203–1221. [CrossRef]

152. Technical University of Denmark. Preventing MIcroplastics Pollution in SEa Water from Offshore Wind (PREMISE) Project. Available online: https://premise.dtu.dk/ (accessed on 1 October 2024).

153. Thacker, B.H.; Doebling, S.W.; Hemez, F.M.; Anderson, M.C.; Pepin, J.E.; Rodriguez, E.A. *Concepts of Model Verification and Validation*; Report # LA-14167-MS: California; Los Alamos National Laboratory: Los Alamos, NM, USA, 2004; p. 41.